Cold Reactive Collisions between Neutral Molecules and Trapped Ions

Lorenzo S. Petralia

Wolfson College

University of Oxford

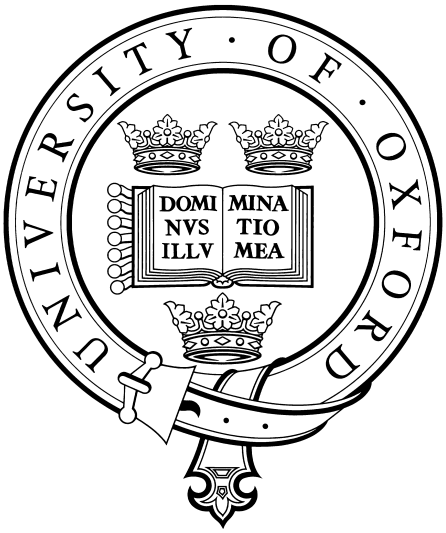

A thesis submitted for the degree of

Doctor of Philosophy

Trinity Term 2018

Cold Reactive Collisions between Neutral Molecules and Trapped Ions

Lorenzo S. Petralia, Wolfson College

A thesis submitted in partial fulfilment of the requirements
for the degree of Doctor of Philosophy of the University of Oxford

Trinity Term, 2018

Abstract

This thesis describes the development and demonstration of techniques for the study of ion-neutral reactive collisions at low temperatures conducted using two unique experimental apparatuses comprising radio-frequency Paul traps. One apparatus combines a Stark decelerator with a Paul trap; the other apparatus features a buffer gas cell interfaced with a Paul trap through an electrostatic quadrupole guide.

A novel ion trap time-of-flight mass spectrometer has been introduced and characterised. This apparatus is designed to detect the ion products of reactive collisions at low temperatures (< 10 K). This detection approach affords excellent detection efficiency and is broadly applicable to all ion-molecule reactions that one could study within a linear Paul ion trap. A proof-of-principle reaction between xenon ions and neutral ammonia isotopologues is examined to test the performance of the new detection set-up.

With the goal of achieving full control over the reaction parameters, the amount of alignment retained by rotationally and translationally cold ammonia molecules exiting the electrostatic guide has been examined using $(2 + 1)$ REMPI detection of the molecules with varying linear polarisation. Simulations suggests how modifications to the current setup will enable full orientation of the cooled molecules reaching the detection region to be achieved.

Experiments on cold charge exchange reactions between sympathetically-cooled Xe^+ and room temperature ammonia (NH_3 and ND_3) have been conducted within laser-cooled Ca^+ Coulomb crystals in a linear Paul ion trap. There is ongoing work to ascertain any difference in reactivity between NH_3 and ND_3 as the neutral reactant species. Preliminary data are discussed at a qualitative level, with the prospect of observing any isotope effect in this charge transfer process. Charge exchange reaction experiments using cold state-selected ammonia are discussed with the goal of establishing reaction rate constants at different collision energies.

Acknowledgements

I would like to start by thanking my supervisor Dr. Brianna Heazlewood, though I cannot possibly find the words (not even in my native language) to express my immense gratitude and esteem for her. You are an amazing role model! I am very grateful to my supervisor Prof. Tim Softley for his wise advice and guidance through my D. Phil. project, for sharing his invaluable expertise and for always encouraging me to look at the bigger picture. Thank you also for getting me on board in the first place and for believing in me during the various challenges and setbacks.

I would like to thank the people I have worked with on a daily basis in the old laboratory: Katharina Meyer (thank you for sharing the challenges of a great experiment), Dr. Edward Steer, Dr. Chris Rennick (thanks for the help in the lab), Dr. Mike Kohlhoff (cheers for the coffee break chats), Dr. Atreju Tauschinsky, Dr. Katrin Dulitz (who inspired and encouraged me), and Fred Cascarini. And many thanks to the new laboratory comrades: Andriana Tsikritea (thank you for the great lab collaboration), Dr. Michal Hejduk (thanks for the wacky jokes), Dr. Neville Coughlan, and Jake Elworthy. Many thanks to Dr. Tertia Softley and Prof. Tim Softley for reinforcing the group spirit by hosting various delicious dinners/BBQs. Special thanks to Jutta Toscano, with whom I shared numerous challenges, pleasant events (at Merton College) and hard times, like the whole saga of the relocation of the laboratory.

I want to acknowledge the incredible amount of skilled and hard work done by Paul Mitchell and Martin Lyne in facilitating the lab move. Also, thanks to the Electronics and Mechanical workshops for the excellent assistance provided during these years. Many thanks to Prof. Stuart Mackenzie and Prof. Grant Ritchie for their helpful support and advice. I am grateful for funding and support I received from COMIQ (Marie Curie Initial Training Network scheme). Particular thanks to Prof. Franco Gianturco for his supervision and kindness during my secondment in Innsbruck. Moreover, thanks to the professors and scientists that have guided me through my academic path, in particular Prof. Sergio di Matteo for his great academic advice and trust.

A great thanks to my friends, especially Joelle, Jutta, Ferd, Alisandro, Giuli, Luca, Derek, Mattia, Paige, Panino, Leonardo, Daniele e Riccardo.

I now want to thank (a whole lot!) my fiancée Maria for always bringing joy and colour to my life. Thank you for the fantastic trips, hikes, adventures and most importantly for being the best partner one can dream of. Finally, a wholehearted thank to my ever-encouraging father and mother. As I always say, I would have not gone this far if it wasn't for your huge love and precious guidance! TuttiTutti sempre!

Parts of chapter 4 of this thesis have been published in this article:

"Ejection of Coulomb Crystals from a Linear Paul Ion Trap for Ion-Molecule Reaction Studies", K. A. Meyer, L. L. Pollum, L. S. Petralia, A. Tauschinsky, C. J. Rennick, T. P. Softley, and B. R. Heazlewood, Journal of Physical Chemistry A, **119**, 12449, 2015.
https://doi.org/10.1021/acs.jpca.5b07919

Chapter 5 is based on the work that has been published in this paper:

"Measurement of the orientation of buffer-gas-cooled, electrostatically-guided ammonia molecules", E. W. Steer, L. S. Petralia, C. M. Western, B. R. Heazlewood, and T. P. Softley, Journal of Molecular Spectroscopy, **332**, 94, 2017.
https://doi.org/10.1016/j.jms.2016.11.003

I wish to acknowledge the referees of these papers for the valuable feedback and fruitful discussions.

Lorenzo Salvatore Petralia
Wolfson College, Oxford
October 2018

Contents

Abstract i

Acknowledgements ii

1 Introduction **1**

1.1 Overview of the field 1

1.2 Techniques for producing cold species 3

1.2.1 Direct techniques 4

1.2.2 Indirect techniques 13

1.3 Techniques for producing cold ions 15

1.4 Applications of cold species and related fields 19

1.5 Low temperature chemistry 20

2 Generating a target of cold ions **25**

2.1 The ion trap 25

2.1.1 The linear Paul trap 26

2.2 Ion trapping and Coulomb crystals 32

2.2.1 Laser cooling 32

2.2.2 Coulomb crystals 34

2.2.3 Sympathetic cooling and multicomponent crystals 37

2.2.4 Main aspects of Coulomb crystals 38

2.3 Experimental configurations of the ion traps 43

2.3.1 The Stark decelerator experiment ion trap 43
2.3.2 The Stark guide experiment ion trap 45

3 Sources of cold molecules 51
3.1 Controlling polar molecules via the Stark effect 51
3.2 The Stark decelerator experiment 53
3.2.1 Decelerator features 53
3.2.2 Operating mode 57
3.2.3 Performance details 59
3.3 The Stark guide experiment 60
3.3.1 Buffer gas cell 61
3.3.2 Electrostatic quadrupole guide 64
3.3.3 Performance details 66
3.4 Summary 68

4 Damped cosine trap detection method 71
4.1 Techniques for Coulomb crystal detection 71
4.2 Damped cosine trap ejection setup 74
4.2.1 Experimental DCT TOF traces 76
4.3 Ejection and detection simulations 80
4.3.1 Detection limitations 81
4.3.2 Consideration of mass resolving power 83
4.4 Summary 85

5 Controlling the orientation of the guided cold molecular beam 89
5.1 Orientation of molecules 89
5.1.1 Orientation of ammonia molecules 91
5.2 Experimental methods 92

5.2.1 Resonant Enhanced Multiphoton ionisation 93
5.2.2 Probing alignment with polarised REMPI 94
5.3 Simulations 98
5.3.1 Simulating the REMPI spectra 98
5.3.2 Simulated trajectories 100
5.4 Results and discussion 103
5.4.1 Maintaining the orientation 105

6 Charge exchange of cold Xe^+ with ammonia neutrals 109
6.1 The reaction of xenon ions with ammonia 110
6.1.1 Choice of the system 110
6.1.2 Observations with NH_3 and ND_3 112
6.2 Experimental methodology 113
6.3 Analysis 116
6.3.1 Evaluating the reaction rate coefficient 116
6.3.2 LIF imaging analysis 117
6.4 Outlook 123

7 Conclusions 127

A LIF image manipulation code 130
A.1 Tutorial 131
A.2 The `enhance-LIF.py` script 132

References 148

Chapter 1

Introduction

1.1 Overview of the field

Achieving full control over the various experimental reaction parameters constitutes a prevailing goal in the study of reaction dynamics. Moreover, accurate quantitative detection methods are fundamental premises to investigate the kinetics and dynamics of chemical reactions. Hence, the development of a toolbox for manipulating and monitoring reactive processes is of crucial importance for unravelling how chemical reactions happen in different temperature regimes.

A common framework for describing a reaction process is the assumption of an underlying potential energy surface featuring a thermal activation barrier that separates the reaction coordinate into reactants and products. A reaction is deemed to have taken place when the colliding reaction partners possess sufficient kinetic energy to exceed the activation barrier E_a. In such cases, the bimolecular reaction rate constant can be approximated using the Arrhenius equation [1]:

$$k_2 = A\ e^{-\frac{E_a}{RT}} \tag{1.1}$$

where A is the Arrhenius scaling factor (depending on the reaction) and R is the molecular gas constant. From the Arrhenius equation, one can infer that the lower the temperature the more negligible the rate of reaction becomes. There are, however, types of reactions that proceed at a fast pace even at low temperatures – typically due to the lack of an activation barrier along the reaction coordinates. These types of reactions are normally called "barrierless"; numerous radical-radical, radical-neutral, and ion-neutral reactions and some processes involving excited Rydberg states belong to this category [2]. For instance, the majority of the atmospheric reactions of trace species involve open-shell radicals, and these reactions can proceed with rapid rates at low temperatures and low number densities due to the absence of an activation barrier (or the presence of a very small barrier).

More generally, it is expected that barrierless reactions dominate the chemistry of naturally occurring cold spaces, such as the mesosphere and the interstellar medium (ISM). The ISM involves areas of space where temperatures are typically on the order of $10-30$ K (depending on the density of the molecular clouds), and can drop as low as 2.7 K, corresponding to the energy contribution of the cosmic radio-wave background (CRB). Interestingly, temperatures lower than the CRB (≈ 1 K) have been detected from the central region of the Boomerang Nebula. This is due to the combination of two mechanisms: the absorption of CRB photons by CO molecules and the adiabatic expansion of the nebula [3].

It is impractical to perform accurate *in situ* experimental observations of the reactivity in this environment, aside from taking spectroscopic measurements. However, the ability to mimic cold conditions in a laboratory environment allows to fully elucidate the reaction mechanisms of important chemical processes in naturally occurring cold gas-phase environments.

Another key aspect of low temperature chemistry research is that it enables one to uncover the details of the underlying potential energy surfaces (PESs), revealing

features normally hidden by thermal averaging at higher temperatures. The ability to experimentally examine reactions at low temperatures (where fewer states are populated) and in a controlled manner, allows one to establish the contribution each state (or a handful of a few states) makes to the reaction rate.

Over the past ∼50 years, the development of methodologies for producing and taming cold (neutral or ionic) atoms and molecules has paved the way for experimentally exploring the largely untrodden field of cold chemistry. The initial reason to cool down particles (atoms) — in the sense of reducing their kinetic energy — was to obtain more precise spectroscopic measurements: decreasing the particles' random motion meant a decrease in Doppler broadening of the spectral line-widths. Subsequently, a wide variety of research areas have benefited from cooling techniques, such as atomic-molecular-optical (AMO) physics, (ultra)cold chemistry, theoretical condensed matter and the field of quantum information/computing (see section 1.4). The following section will discuss the main experimental techniques that are employed to cool down neutral and ionic species.

1.2 Techniques for producing cold species

In this section, various techniques for producing cold controlled (atomic or molecular) neutrals and ions are introduced. This is not meant to be an exhaustive review of all of the available methods in this research field, but rather seeks to frame the research work described later in this thesis. There is no globally applicable method to cool the translational and internal energies of molecules down to the cold ($\lesssim$ 1 K) or ultracold ($\lesssim$ 1 mK [4]) regime. There are, in fact, a variety of methods to choose from – depending on the system of interest and the desired temperature and experimental conditions. Each technique has different advantages, disadvantages and limitations. Despite the large variety of techniques, the common underlying challenge is to achieve

high sample densities and to expand the range of cold species that can be formed, thus broadening the number of systems that can be studied at low temperatures. In the literature it is common to categorise cooling techniques into two distinct branches: direct and indirect methods. With direct techniques, the particles themselves are cooled to low temperatures; indirect techniques see cold species produced *in situ* from pre-existing cold atoms.

1.2.1 Direct techniques

Supersonic expansion

Supersonic expansion has been the traditional way to obtain cold molecular beams. In this technique, gas-phase species of interest are seeded in a carrier gas and subsequently expanded from a high pressure ($\sim$ a few bar) container into a vacuum chamber via a small orifice with a diameter $d_s \gg \lambda_{\text{free}}$ (where λ_{free} is the mean free-path of the admitted sample). The centre of the resulting free jet expansion is then filtered using a skimmer. This method yields a high density beam ($\sim 10^{13}$ cm^{-3}) with high translational velocity (but highly unidirectional) with a low translational velocity spread and low internal energies (corresponding to internal temperatures of $\sim$1 K).

There have been improvements for addressing the main limitation of the supersonic expansion technique, *i.e.* the elevated translational velocity of the beam (in the laboratory frame). Specifically, Gupta and Herschbach introduced a rotating mechanism (see figure 1.1 (a)) to counter the high velocity of the supersonic beam in the laboratory frame [5]. This mechanical slowing approach relies on a very simple operating principle, is quite versatile, and has achieved forward velocities of less than 70 m s^{-1} (corresponding to translational temperatures $\lesssim$ 10 K) for beams of O_2 [5, 6]. However, due to the substantial centrifugal forces experienced by the nozzle, it is not possible to operate the valve in pulsed mode and consequently it produces a continuous rotating

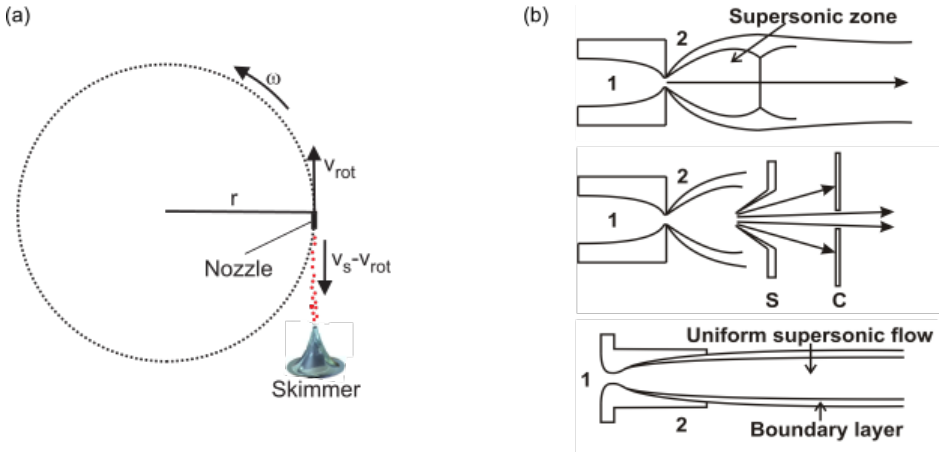

Figure 1.1: (a) Schematic representation of the principle of mechanical cooling obtained via a rotating nozzle setup. Panel (b) illustrates three types of supersonic expansion valve assemblies. The main distinction between the first two is that in the central setup a skimmer is in place. The lower scheme depicts the characteristic convergent-divergent shape of the Laval nozzle, which allows the gas to expand adiabatically. Figures adapted from [7, 8].

spray of gas, yielding high background pressure ($\gtrsim 10^{-4}$ mbar). Moreover, it results in a low-intensity beam with a broad velocity distribution, thus limiting its applicability.

The design of the valve employed in a supersonic expansion process influences the properties of the resulting beam. Instead of adopting a standard orifice (which yields only a limited usable portion of the flow), a "de Laval" valve with convergent-divergent shape (see figure 1.1 (b)) was designed for yielding an adiabatic expansion of the gas to achieve a collimated and uniform flow. The resulting *Cinétique de Réaction en Ecoulement Supersonique Uniforme*[1] (or CRESU) technique was developed by Rowe in the 1980s and provided a high-density molecular beam with a well-defined temperature [9]. The CRESU approach has proved to be highly versatile, with both ion-neutral reactions and radical-radical reactions successfully studied [10]. The CRESU method can be used either alone (starting reactions within the supersonic flow via laser light),

[1]Reaction kinetics in a uniform supersonic flow.

in a crossed beam configuration or in combination with a merged pulsed beam (see subsection 1.2.1). By using a liquid nitrogen-cooled de Laval nozzle for the expansion, temperatures down to 13 K have been achieved [11]. The main limitation of the CRESU technique is that it can be successfully employed only for sufficiently fast reactions, given the limited number of collisions that can occur along the length of the reaction chamber. Additionally, CRESU experiments require a very high flow of gas which entails the need for large vacuum pumping systems and high running costs (especially when investigating deuterated species).

Deceleration

Slowing of a molecular beam can be performed by employing tailored schemes of external (electrical, optical or magnetic) fields to effectively remove kinetic energy from the system. Control of the switching pattern of the applied external field allows one to govern the final velocity of the sample and hence to tune the final kinetic energy available for a reactive collision.

In a Stark decelerator — originally devised and implemented by Bethlem *et al.* [12] — packets of dipolar molecules from a supersonic expansion travel through a series of electrodes whereby rapidly switching electric fields serve to decelerate the molecules via conversion of kinetic energy into Stark potential energy (see section 3.1). This method is now adopted in various laboratories and it has been used to successfully decelerate a wide range of neutral polar molecules (such as CO, NH_3, ND_3, and SO_2), radicals (such as OH [13] and NO [14]) and even small organic molecules like formaldehyde and benzonitrile [15]. The principle of Stark deceleration and the design of the setup employed in Oxford are discussed in detail in chapter 3.

It is worth noting that atoms and molecules in Rydberg states represent ideal candidates for Stark deceleration due to the characteristic highly polarisble electron distributions and large dipole moments. For instance, successful deceleration of hy-

drogen atoms in $n \approx 30$ can be performed with only two deceleration stages [16]. Consequently, Rydberg-Stark deceleration has been implemented on a chip and successfully employed for H($n = 23-70$) [17]; however, due to the restriction of extremely short lifetimes ($\sim \mu s$), the technique is limited to hydrogenic species.

Building on the success of the Stark deceleration, the magnetic counterpart — *i.e.* involving the switching of magnetic fields and employing the Zeeman effect — was realised by Vanhaecke *et al.* [18] (and almost simultaneously by Narevicius *et al.* [19]), thus expanding the scope of neutral species that could be decelerated. Typically, in a Zeeman decelerator, a series of coils (or electromagnets) is operated in a pulsed sequence protocol to produce a moving Zeeman potential energy hill for paramagnetic species travelling through the decelerator, thus removing the kinetic energy of the sample. The technique has been used to slow down hydrogen and deuterium atoms [18], metastable neon and nitrogen atoms [19, 20], methyl radicals and molecular oxygen [21, 22]. However, the large number of deceleration stages required for slowing down paramagnetic molecules effectively restricts this technique to low-mass species. The diagram in figure 1.2 shows the outline of the Oxford Zeeman decelerator setup; recent studies in the Oxford group have demonstrated pulsed current schemes optimised with the aid of evolutionary algorithms to enhance the density of decelerated particles and the amount of deceleration achievable [23].

Another deceleration method uses intense optical fields to manoeuvre molecules. In order to perform optical deceleration, two high power pulsed and counter-propagating laser beams interfere to create an optical lattice as depicted in figure 1.3. Then, the laser frequency is tuned so that the optical potential minima (*i.e.*, lattice sites) travel at the same velocity as the molecule of interest; reducing the velocity of the lattice, decelerates the molecular beam. Thus far, I_2 and C_6H_6 have been cooled down to $T = 1$ K via optical deceleration [25].

While Stark and Zeeman deceleration are limited to polar molecules and paramag-

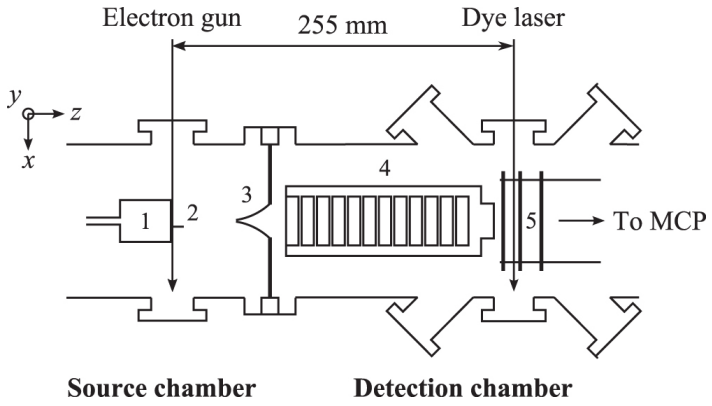

Figure 1.2: 2D CAD drawing of the Oxford Zeeman decelerator. The image clearly shows the position of the main elements: pulsed valve (1), capillary tube (2), skimmer (3), Zeeman decelerator coils (4), and time-of-flight mass spectrometry setup (5). Figure adapted from [24]

netic species (respectively), optical deceleration can be performed on a wider range of neutral species. Nevertheless, it too presents some drawbacks. Firstly, it requires very intense laser pulses – with the associated risk of inducing multiphoton ionisation or molecular photodissociation offering additional technical challenges [26]. Secondly, it requires a large initial volume of molecules, since only a small portion of the molecular beam is able to be effectively captured by the lattice and thus decelerated.

Velocity selection

A bent guide with confining electric or magnetic fields can be used to filter and transmit only the fraction of an effusive beam that is travelling below a certain threshold velocity (depending on the curvature of the bend, the intensity of the applied field and the properties of the target species). The Maxwell-Boltzmann distribution characterises the velocity spread of a thermal gas at a given temperature. Even at room temperatures, there will be a finite portion of the beam featuring low translational velocities. In the case of electrostatic velocity selection, high voltages are continuously applied to a curved path of electrodes (nomally in a quadrupolar or hexapolar con-

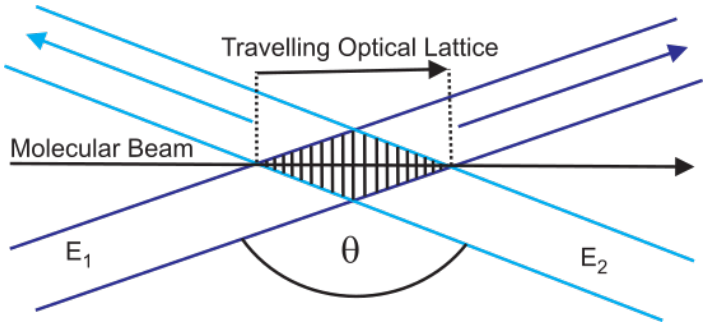

Figure 1.3: The diagram illustrates the technique of optical deceleration. Two high power pulsed laser beams generate the optical fields E_1 and E_2. The fields nearly counterpropagate (small separation angle θ) and their interference yields a travelling optical lattice. The molecules can be trapped in the optical lattice sites and the velocity of this lattice can be tuned by adjusting the laser frequencies, thus achieving deceleration of the incoming molecular beam. Figure adapted from [7].

figuration) to generate large static electric fields to confine polar molecules from an effusive beam and guide only the lowest translational energy portion of the molecules along the curved path; molecules travelling above a certain threshold velocity will be lost from the guide at the curved section (as the forces of the confining fields will be insufficient to overcome the magnitude of the forward velocity vector).

As such, electrostatic guiding does not actively decrease the kinetic energy of the molecules — it instead provides a colder sample by filtering out the more energetic part of the initial molecular beam. Electrostatic velocity selection was firstly demonstrated in Rempe's group [27], for an effusive beam of dipolar molecules, employing a high-voltage quadrupole guide (± 5 kV) with a 90° bend. The technique is applicable to a wide range of polar species that exhibit a reasonable Stark potential energy shift (such as CH_3F [28], ND_3 [27] and isotopologues of water [29]) and it typically yields translational velocities corresponding to temperatures of approximately 10 Kelvin.

The electrostatic velocity selector has been successfully combined with a cryogenic effusive source to yield a continuous beam of molecules with low internal energies and higher number density [30]. Electrostatic selection has been employed in one of the

experiments performed for this thesis work, and will thus be discussed in more detail in section 3.3.

Recently, the electrostatic guide approach has been further developed to create a rotating spiral-shaped device to actively slow down molecules [31]. In this rotating frame, polar molecules are guided towards the centre of the rotation, whilst climbing a centrifugal potential hill and losing kinetic energy (which is converted to centrifugal potential energy).

A method analogous to electrostatic velocity selection, entails the use of magnetic fields to confine and filter paramagnetic species. Various groups have devised different designs for a magnetic guide [32, 33, 34, 35]. In our group, J. Toscano *et al.* [36] have developed a magnetic guide featuring a controllable "zig-zag" geometry rather than a curved path. In this magnetic guide setup, the fields are produced via Halbach arrays comprising 12 NdFeB permanent magnets in a hexapole configuration. The guiding Halbach arrays are mounted on actuator arms (for fine adjustment of the position and angle of the magnets) to manipulate the passage of radicals with the target properties up and down around two skimmer blades, which serve to block all other undesirable components of the beam.

Cryogenic methods

As previously mentioned, an electrostatic quadrupole guide velocity selector was combined with a cryogenic effusive source to achieve low rotational energy distributions in the final guided beam [30]. Specifically, this pre-cooling of the beam is achieved through collisional cooling with a buffer gas at cryogenic temperatures. Buffer gas cooling represents probably the most versatile technique to reduce the internal and translational energy of atomic and molecular species via inelastic and elastic collisions (respectively) with a buffer gas (typically He or Ne). This technique has also been combined directly with ion traps to internally cool trapped ions [37]. For example, the

internal and translational degrees of freedom of ions held in a 22-pole trap at $T = 10$ K were cooled via collision with a He buffer gas. The details of buffer gas cooling and the buffer gas cell utilised in our group are described in section 3.3.

A well-established cryogenic cooling technique adopted in the field of high-resolution spectroscopy involves the use of helium nanodroplets [38]. With this method, droplets (small assemblies of thousands of atoms) of ultracold helium atoms act as cooling pockets, containing the molecular species of interest. He nanodroplets are formed through supersonic expansion of a low temperature ($5 - 25$ K) and high pressure ($5 - 45$ bar) source of helium. The resulting nanodroplets exhibit temperatures of $\sim 10^2$ mK via evaporation and are sent into a vapour cell to incorporate target species that are cooled via thermalisation within the droplets. It is a great tool for examining the spectroscopy of highly reactive, transient species such as radicals [39]. The technique has also been used for investigating some cold reactions within the droplets, although this approach is currently limited to the formation of heteronuclear alkali dimers such as NaK [40].

Laser cooling and trapping methods

Independently discovered by Hänsch and Schawlow for free particles and by Wineland and Dehmelt for trapped particles in the mid 70's [41], laser cooling was a groundbreaking technique that has shaped the field of ultracold atomic and molecular physics in the decades since it was first introduced. By tuning the laser light to be just below a selected resonant frequency, the photon-particle collisions (during absorption or emission events) can be repeated over time ($\sim 10^6$ cooling cycles) to exert a net momentum transfer and remove kinetic energy from the particle (see subsection 2.2.1 for more details). The method can cool species down to ~ 10 μK (photon recoil limit) and can, in principle, be applied to any (neutral or charged) atom or molecule. However, to be efficient, laser cooling requires the existence of a favourable 2-level system so that the absorption/emission events can be repeated numerous times without

species getting "shelved" in other energy levels. Using additional lasers, it is possible to re-pump the shelved population back to the main cooling transition, and thus to effectively close the laser cooling cycle. Given the complexity of the energy levels of most molecules (specifically, the large numbers of ro-vibrational states) this method — albeit generally applicable in theory — is experimentally limited to a small selection of species [42]. Laser cooling is commonly adopted for ensembles of alkali metals or alkaline earth metal ions, for which the currently available continuous-wave lasers allow for an efficient closed cooling cycle.

Laser-cooled atomic species are typically confined using a trap — optical [43], or magneto-optical (MOT) [44] — thereby reaching temperatures of $\sim$ 10 μK. Once trapped, a further cooling protocol (evaporative cooling) can be applied [44]. With evaporative cooling, the trapping field is ramped down in amplitude and, consequently, the more energetic atoms of the ensemble can escape the shallower trap depth. The process can be repeated (allowing the ensemble to rethermalise between each ramp-down event) to reach temperatures $\sim$ 100 nK below T_{BEC}, thus obtaining a Bose-Einstein condensate (BEC) or a degenerate Fermi gas sample (^{37}Rb was the first species for which a BEC was demonstrated [45]).

Crossed and merged beam methods

The approach of crossing molecular beams was briefly mentioned when discussing the supersonic expansion technique (see 1.2.1). The methodology of beam crossing enables one to investigate chemical reactions between reactants originating from two independent sources. It can also be used as a means of cooling. For instance, in kinematic cooling, a beam of molecules is cooled via collision with a crossed-beam of noble gas atoms; by accurately choosing the initial scattering conditions (namely, the colliding partner mass and velocity), a subset of the sample of the molecule of interest can undergo (near) vector cancellation, thereby leaving these molecules (almost) stationary

in the laboratory frame [46]. Cold (sub-Kelvin) NO and ND_3 have been obtained via inelastic collisions in this way, with Ar [46] and Ne [47] collision partners (respectively). A sample of ∼100 mK krypton was produced via elastic Kr-Kr collisions [48].

By designing molecular beamlines crossing at a grazing angle, it is possible to obtain favourable experimental conditions – such as extremely low collision energies between the colliding partners in the frame of the centre of mass of the collision (even though the kinetic energies of the colliding species may be individually high in the laboratory frame) [49]. In the limit of this approach, two beams can actually be merged. In the merged beam approach, two individual beams are formed (typically via supersonic expansion methods) and are combined at a crossing angle of 0° through the use of electrostatic or magnetic benders. Partial wave resonances in bimolecular gas-phase reactions have been observed in merged beams of O_2 + H_2 owing to the low collision energies and enhanced sensitivity offered by this method [50]. Narevicius and coworkers have successfully examined the Penning ionisation of a beam of Ar or H_2 by merging it with a beam of metastable He guided via a magnetic quadrupole [51]. Moreover, a magnetic guide and an electrostatic guide have been combined in Osterwalder's laboratory, leading to merged beam collision energies as low as $\sim 10\ \mu$eV [33]. Merged beams allow one to effectively examine certain types of cold neutral-neutral (and also metastable-neutral) reactions, however it is challenging to apply the technique to the study of ion-neutral reactions since the ions would react (exchange charge) with the background before reaching the target colliding partners.

1.2.2 Indirect techniques

"Photostop" is an indirect cooling technique based on the principle of momentum cancellation, as discussed in the direct kinematic cooling method above. Photostop involves the near-threshold photo-dissociation of a molecule using a specific wavelength,

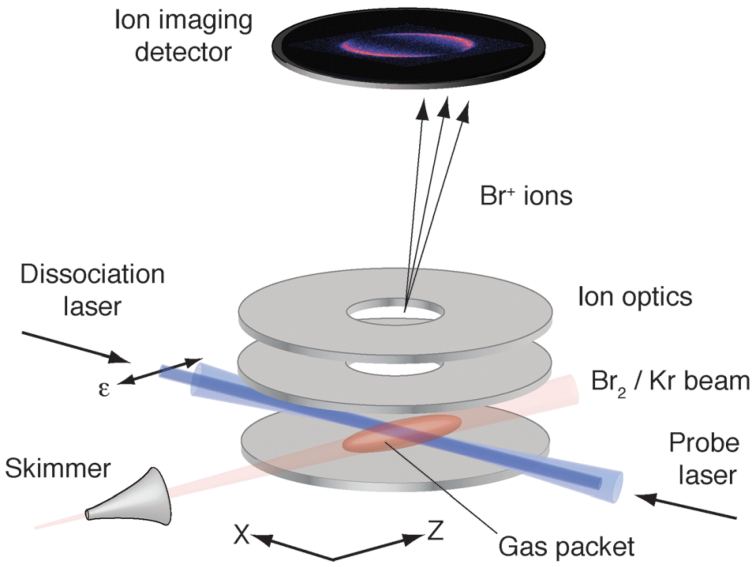

Figure 1.4: Pictorial view of the Oxford photostop experiment [53] - Reproduced by permission of the PCCP Owner Societies.
https://pubs.rsc.org/en/content/articlelanding/2011/CP/c0cp02472d#!divAbstract

polarisation and laser direction, so that one photo-fragment is produced retaining the whole available kinetic energy, thus leaving the other fragment with zero velocity in the laboratory frame [52, 53], 1.4. The molecular precursor is seeded in a noble gas and admitted into a high vacuum chamber through a supersonic expansion. Here, the molecules are illuminated by a laser beam tuned to a certain dissociative molecular transition, thus causing fragmentation. The laser beam and the initial velocity of the molecular beam can be tuned so that, for a subset of photo-fragments of interest, the final velocity in the laboratory frame is lower than the initial beam velocity (or zero), thereby obtaining a decelerated (or stationary) ensemble of fragments. The drawback of this technique is that one can only address and slow down a small fraction of the molecular beam. As such, the process is typically performed inside a magnetic trap to accumulate density over sequential laser pulses. It is currently the only method available to produce cold halogen atoms.

As mentioned earlier, the technique of laser cooling, rapidly revolutionised the field of cold and ultracold chemistry. Once laser-cooled, two ultracold atoms can undergo photo-association to form an ultracold diatomic molecule [54]. Specifically, after colliding and absorbing the correct wavelength of laser light, the atoms can be bound together forming a translationally ultracold highly vibronically excited dimer: $\mathrm{A}+\mathrm{B}+\gamma_{PA}=(\mathrm{AB})^{*}$, where γ_{PA} is a photon with the necessary frequency to induce a transition in the bound system (possessing kinetic energy greater than the AB ground state dissociation energy).

An analogous associative method, called magneto-association, features the formation of ultracold diatomic molecules *in situ* from ultracold atoms via a precisely tuned external magnetic field. Specifically, a magnetic field is used to tune the colliding species into resonance[2] with a bound state on an excited potential energy curve. The adiabatic crossing between the two potential energy surfaces (PESs) leads to the formation of an ultracold molecule. As in the photo-association process, the subsequently formed dimer is in a highly excited ($v \gtrsim 20$) vibrational state. For this reason, these associative techniques are often paired with a second method (like the stimulated Raman adiabatic passage or STIRAP technique [55]) so that the dimers are internally cooled to the ground rovibronic state. It should be noted that the application of photo- and magneto-association is limited to a small number of diatomic molecules with favourable resonances, mainly alkali metals (either homonuclear or heteronuclear diatomic molecules).

1.3 Techniques for producing cold ions

Laser cooling is a ubiquitous technique used throughout the AMO and (ultra)cold chemistry communities, and is frequently employed alongside ion trapping methods

[2] A Feschbach resonance occurs when a two-atom system A-B in a non-bound state features the same potential energy as that of the related (excited) bound state $(\mathrm{AB})^{*}$.

for the cooling and confining of ions.

There are various options for trapping ionic species. Paul traps are the most common choice when it comes to combining ion trapping with laser cooling due to the convenient laser access. Linear Paul traps consist of four segmented rods arranged as a quadrupole; a combination of radio-frequency (RF) and static (DC) voltages are applied to the electrodes to achieve confinement of the ions at the centre of the trap (see chapter 2).

A remarkable advantage of performing laser cooling on ions rather than neutrals is that, in ensembles of trapped ions, all of the motional degrees of freedom are coupled via the continuous elastic collisions mediated by the Coulomb force. Therefore, laser cooling can be effectively performed with lasers along just one direction (rather than the six directions required in a MOT), although augmenting the process with additional cooling lasers in opposing directions allows one to reach lower temperatures more efficiently.

As a consequence of this Coulomb-mediated coupling, other ionic species that are not laser-cooled can also be trapped and cooled down via elastic collisions with the laser-cooled ions. This versatile cooling mechanism for ions, named sympathetic cooling, greatly expands the scope of ionic species that can be studied at low temperatures and is described further in subsection 2.2.3.

Whilst Paul traps conventionally operate with cosine-wave trapping fields, several groups — including our own research group — have made the use of square-wave RF trapping fields [56]. In the Oxford (so-called) digital ion trap, pulsed voltages are applied to the trap quadrupole rods to provide radial confinement; this has significant advantages in terms of ion trap mass spectrometry detection efficiency, as discussed in detail in section 4.2. The Drewsen group has pioneered a cryogenic version of a linear Paul trap [57], which can operate at temperatures as low as 4 K owing to a complex system of encapsulated heat shields (see figure 1.5).

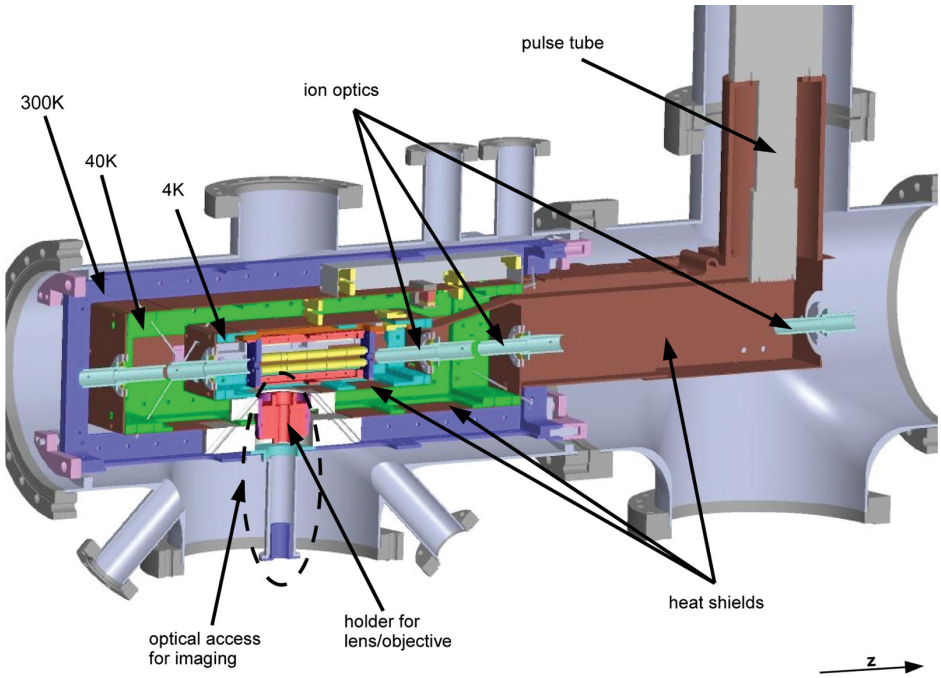

Figure 1.5: CAD drawing of the cryogenic linear Paul trap recently built by Drewsen and coworkers. This linear Paul trap can be operated down to a temperature of ≈ 4 K. Figure reproduced from [57], with the permission of AIP Publishing.
https://doi.org/10.1063/1.4742770

Advances in circuit miniaturization technology have also led to the realisation of a Paul trap on a chip [58], and recent work by Willitsch and coworkers has demonstrated sympathetic cooling on a surface-electrode trap [59]. RF traps have also been successfully combined with magneto-optical traps, generating hybrid traps, to investigate cold ion-ultracold atom reactions [60].

In the realm of RF traps, multipole ion traps (like the 22-pole trap devised by Gerlich [37]) are widely used for the study of spectroscopy and dynamics of cold ions, as they offer the advantage of steeper potentials and larger field-free trapping volumes, albeit at the expense of optical and mechanical access [61]. Spectroscopy and thermometry measurements of cold negative ions have been conducted by Wester and collaborators utilising a cryogenic 22-pole trap combined with time of flight mass spectrometry [62, 63].

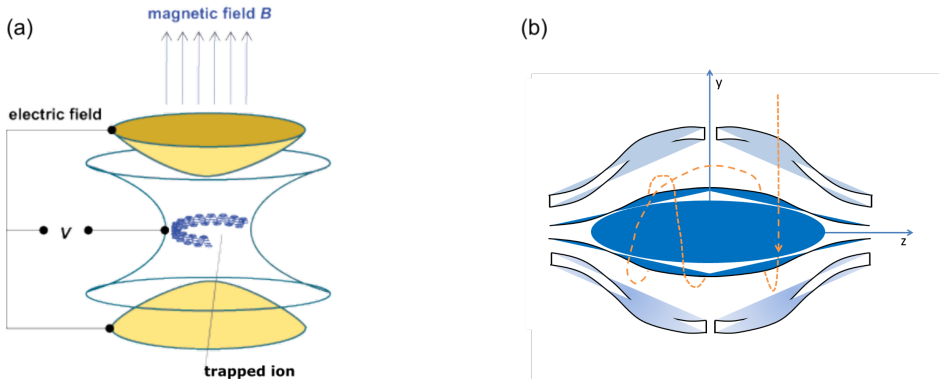

Figure 1.6: Pictorial view of typical ion trajectories in a Penning ion trap (a) and in an Orbitrap (b).

There are types of ion trap that do not make use of time-varying electromagnetic fields, including Penning traps and Orbitraps. In a Penning trap, confinement is achieved via static electric and magnetic fields. Specifically, three hyperboloidal electrodes (two endcaps and one ring electrode) provide axial confinement (see figure 1.6 (a)). The additional presence of a magnetic field (typically a few Tesla in magnitude) oriented along the ring electrode axis yields the three-dimensional trapping fields [64]. Orbitraps — arising from the further development of the older Kingdon trap [65] — comprise axially symmetric electrodes (the inner one featuring a spindle shape and two bell-shaped outer electrodes) around which ions with a specific mass-to-charge ratio are kept in rotation and oscillate across the axis, affected by an additional axial electrostatic confinement (see figure 1.6 (b)). The Orbitrap has been developed as a versatile tool for the high-resolution mass spectrometry of proteins [66].

It is important to note that, due to the lack of RF-induced micromotion (see section 2.1), Penning traps and Orbitraps offer the advantage of lower heating rates compared to RF traps. However, as a consequence of the applied field, ions orbit around the trap axis and consequently stable confinement on a extended volume is not achievable. Additionally, in collisional experiments, the orbiting of the ions would result in high collision energies. Moreover, Orbitraps present issues with laser access

and long trapping times.

1.4 Applications of cold species and related fields

As a result of the relatively recent development of a broad range of cooling techniques, it has increasingly become possible to probe the untrodden field of (ultra)cold chemistry. Techniques are refined and combined to expand the range of chemical processes that can be examined at low temperatures. It becomes possible to access the details of exotic phenomena (*e.g.* quantum tunnelling and reflection [67], and multiple scattering resonances [32]) that occur during reactive collisions in the ultracold regime. Moreover, the ability to study chemical reactions at cold and ultracold temperatures offers a way to verify low temperature reaction theories that were formulated decades ago and are yet to be fully tested [68, 69, 70, 71].

A variety of other scientific communities have benefited from the advancement of cooling techniques. Improvements in laser cooling and trapping have seen the development of highly accurate applications, such as atomic clocks [72]. The tremendous impact of atomic clocks, from redefining the second to everyday life applications (communication, satellites, GPS, power-grid synchronization to name a few) has led research groups to hunt for increasingly accurate ultracold atomic clock systems [73]. In this regard, Hudson and collaborators are conducting research on a promising "nuclear" clock based on a high-Q transition in the ^{229}Th nucleus [74]. This system was chosen for the convenient lowest nuclear transition energy (compared with any known nuclear excitation) and the advantageous low background interference (nuclear energy levels are relatively insensitive to their environment) which offer the chance to be implemented in a solid state environment, such as a crystal doped with ^{229}Th.

Traps are employed as a preparatory step for performing further cooling, or as a means of storing previously cooled particles. The enhanced life time and perturbation-

free environment experienced by trapped ultracold ions make ion traps the ideal candidates for quantum computing units (nodes) to securely store and coherently change the quantum state of the (qubit) system [75, 76]. In this regard, the research conducted by Lucas and collaborators on the adoption of ultracold ($\approx 1.2\ \mu$K) $^{43}Ca^{+}$ ions as qubits, and the use of small magnetic fields (≈ 10 mT) and near-field microwaves to coherently change the state of the qubits, is highly promising [77]. Significant progress has also been made by the Hensinger group on the implementation of microfabricated ion traps on 2D silicon dioxide substrates as highly scalable platforms for the manipulation and storage of Yb^{+} qubits [78]. The realisation of quantum computing is expected to facilitate the calculations of problems that would take the fastest conventional supercomputer clusters million of years.

Initially proposed by Feynman [79], another potential application of ultracold systems is the implementation of quantum mechanics simulators for studying complex many-body systems, particularly as applies to solid state physics [80, 81]. For instance, ultracold dipolar samples could be applied as a modelling platform for emulating complex condensed matter systems [82]. Specifically, dipolar quantum gases on an optical lattice can be manipulated with external fields to explore novel ferroelectricity or exotic magnetic phase transitions [83]. Of prominent interest is also the discovery of exotic physics such as investigation of the time-invariance violation of fundamental constants via high-precision spectroscopic tests [84].

1.5 Low temperature chemistry

The concept of barrierless reactions, *i.e.* a set of reactions that occur at an appreciable rate even at low temperatures, was introduced earlier in this chapter. The Arrhenius equation cannot be adopted to model these low temperature processes , as they feature no activation barrier and frequently exhibit an inverse relationship with temper-

ature. The Langevin model can be generally used to predict reaction rate constants for barrierless processes [85, 86]. According to this theoretical framework, ion-neutral molecule reaction rate constants can be calculated simply through the knowledge of the ion charge q, the polarisability of the neutral molecule α, and the reduced mass of the reactants μ:

$$k = 2\pi\sqrt{\frac{q^2\alpha}{\mu}} \tag{1.2}$$

It is evident that, according to the Langevin equation 1.2, the rate constant for a barrierless reactions is expected to be quantum state independent, and (most importantly, for this work) temperature independent. Thereafter, various modifications to this model (e.g. the inclusion of state-dependent terms) have been implemented in the so-called post-Langevin theories, or capture theories [87, 7].

It must be noted that, despite the absence of an activation barrier, there can still be a centrifugal barrier term to take into account the orbital angular momentum of the reactants. This is central to the capture theory approach to barrierless reactions and is encoded in the impact parameter b appearing in the formula of the effective ion-molecule intermolecular potential modelling the dynamics of ion-molecule reactions along a single reaction coordinate:

$$V_{\text{eff}} = \frac{b^2 E_{\text{coll}}}{r^2} \; - \; \frac{C_s}{r^s} \tag{1.3}$$

where E_{coll} is the collisional energy and r is the distance separating the reactants. The subscript s denotes the type of interaction (*e.g.*, $s = 4$ for ion-dipole interaction or $s = 6$ in case of van der Waals's forces); C_s represents an orientation parameter. The aforementioned impact parameter b is linked to the orbital angular momentum, the reduced mass of the system and the relative velocity of the reactant through the equation: $b = L/(\mu\ v_{\text{rel}})$. The impact parameter indicates the closest approach

available for the colliding reactants in the case of no chemical barrier.

A common characteristic among capture theories is the assumption that, if the collision parameters allow the centrifugal barrier to be surmounted, then the reaction will occur with 100% probability [87, 7, 88]. At lower temperatures, where the relative velocity (and the angular momentum) can assume smaller values, there will be a weaker centrifugal barrier contribution to the intermolecular potential V_{eff} and subsequently a higher probability of a reactive collision event. Moreover, at low internal temperatures, only the lowest rotational quantum states will be populated, which could lead to an increase of the reaction rate constant given the enhanced ability of the reactants to "clasp" each other in a more favourable orientation [87]. More advanced post-Langevin theories have indeed introduced quantum-state dependent terms in the reaction rate constant calculations. For instance, the rotationally-adiabatic quantum capture theory developed by Clary implements a temperature and quantum-state dependence for k and predicts an increase in reactivity at temperatures lower than 20 K, given the enhanced polarisability of the rotational wavefunctions of the lowest rotational quantum states [89]. Fully quantum capture theories extend these arguments by considering the propagation of the wave describing the collision partners over the potential energy landscape that includes the centrifugal barrier [70].

In section 1.4 it has been pointed out that the capture theories are yet to be fully tested given the experimental challenges associated with studying systems at low temperatures. Unless the reaction of interest can be initiated with laser light within a cold molecular source, it is typically necessary to combine two low temperature sources to investigate reactive collisions. Specifically, this thesis is concerned with the study of reactive collisions between ions and neutral molecules in the cold regime. In order to examine cold ($\lesssim$ 30 K) ion-molecule reactive collisions, a source of cold neutral molecules and a localised target of cold ions have been employed (see chapter 2 and 3).

In the past, experiments examining low temperature ion-molecule reactions involved the use of selective ion flow tubes (SIFT) and the CRESU technique [90, 91]. SIFT has proved to be a versatile and effective technique and a huge number of ion-neutral molecule reactions have been analysed with this method [92, 93]. Adopting cryogenically cooled SIFT apparatus has enabled reactions to be examined at temperatures down to 77 K [94].

The ability to produce cold particles (atoms, molecules and ions) has a vital role in the investigation of reactions occurring in very low temperature environments. It is expected that the majority of interstellar molecules are formed via reactions between positive ions and atomic or molecular neutral species [10, 95]. To facilitate the simulation of molecular synthesis in the interstellar clouds, databases of rate constants have been compiled over several decades [96, 97]. It is widely acknowledged that the majority of the reaction rate constants included in these databases – and incorporated into models of atmospheric and interstellar chemistry – have been recorded under room-temperature conditions. Precise studies are required, at temperatures comparable to the ambient conditions of the gas phase environments of interest, in order for these models to be accurate and effective predictive tools [98, 99]. There is an evident need for extensive and accurate studies of ion-neutral reactions at low temperatures.

The overarching goals in the body of research taking place in the area of cold chemistry are to achieve full state selectivity for any given reaction and to develop detection tools to investigate state-to-state reaction dynamics. We aim to study collisions of ions with neutral molecules at low temperatures, measuring reaction rates with control of the quantum states (including the M quantum states that affect the orientation) and collision energies of the reacting species, and identification of the products and branching ratios between multiple product channels. We are also interested in studying isotope effects, especially with H/D substitution as these are likely to be highly sensitive to the quantum nature of the reaction dynamics at low tempera-

tures. Specifically, the work described in this thesis is concerned with the combination of trapped ions with sources of cold polar molecules to investigate low-temperature chemistry. The first chapter of this thesis (this chapter) has provided an overview on this field of research and the various techniques available to produce and examine cold neutrals and ions. The second chapter introduces the theory behind ion trapping, laser cooling, and Coulomb crystals, and describes the details of the adopted ion traps. In the third chapter, the two sources of cold molecules used throughout the D. Phil project are described in detail. The fourth chapter presents the novel time-of-flight mass spectrometry setup characterised and employed for studying ion-molecule reactions in the cold regime. Herein, alternative methods are firstly discussed and compared with the one developed as part of this thesis work. A study on the orientation effects on cold electrostatically-guided polar molecules is then reported in the fifth chapter. In chapter 6 a charge exchange reaction between xenon ions and ammonia neutrals in a calcium Coulomb crystal framework is examined in a preliminary study in different temperature regimes (effusive and guided beams). The final chapter provides the conclusions for the thesis and outlines the possible directions for future work.

Chapter 2

Generating a target of cold ions

This chapter outlines the experimental devices employed for the production of Coulomb crystals, the target of cold ions for the study of ion-molecule reactive collisions. The theory of ion trapping and laser cooling will be briefly discussed, in addition to the ways in which the ions can be manipulated.

2.1 The ion trap

Given the high localisation of trapped, laser-cooled ions and the high sensitivity offered by Coulomb crystal detection methods (see chapter 4), ion traps provide an ideal environment for the study of ion-molecule reactive collisions at low temperatures. Ion traps were first developed in the 1950s and are devices that allow one to spatially confine the motion of charged particles by means of electric and magnetic fields. These trapped particles tend to accumulate at the centre of the trap in order to minimise their energies. However, the Coulombic repulsion between like-charged ions prevents them from getting too close to each other and, as result, an inter-ionic equilibrium distance is reached. Consequently there is a maximum density of particles that can be accommodated in an ion trap.

An electromagnetic potential well is required to trap ions. Due to the mathematical constraints of the Laplace equation in charge-free space (see equation 2.1), no potential minimum can exist in three-dimensions with static electric fields. The only permitted stationary points are saddle points; in a radio-frequency (RF) trap, RF voltages are applied which yield a rotating saddle point [100]. RF traps are also called Paul traps as they were first devised by Wolfgang Paul in Bonn (for this work he was awarded the Nobel prize Physics in 1989 [101]).

$$\Delta\phi = \frac{\partial^2\phi}{\partial x^2} + \frac{\partial^2\phi}{\partial y^2} + \frac{\partial^2\phi}{\partial z^2} = 0 \tag{2.1}$$

As mentioned in section 1.3, researchers operate with different ion trap designs according to their particular research goals. In addition to hyperbolic [100], linear cylindrical [102], and surface (chip) [103] geometries, Paul traps have also been designed using bladed [104], needle [105], or spherical [106] electrode configurations. Interestingly, a needle design has allowed Köhl and coworkers to build a trap coupled to an optical cavity (consisting of micro-machined fibre-couplers) with the intention of facilitating the study of ion-photon qubit information exchange [107].

The excellent optical access and the larger trapping volume (which translates into higher numbers of ionic reactants and product ions) offered by the cylindrical linear Paul trap makes it the ideal design for cold chemistry applications [108]. The experiments described in this thesis utilise a linear Paul trap, which will be described in the following subsection.

2.1.1 The linear Paul trap

The linear Paul trap consists of 4 stainless steel cylindrical electrodes in a quadrupole arrangement, in which each electrode is divided into three segments, with these components electrically isolated from each other via Macor insulators. The result is 12

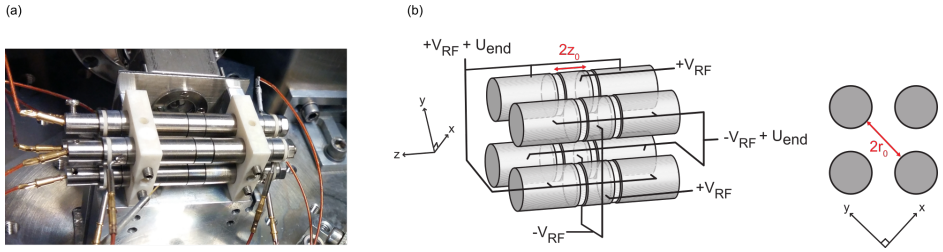

Figure 2.1: (a) Photograph depicting the linear Paul trap used in our laboratory in the experiment involving a Stark decelerator. (b) Schematic front and side views of the adopted ion trap illustrating the voltage configuration. In addition to V_{RF} and U_{end}, it is possible to independently vary DC bias voltages on the 12 electrodes to manoeuvre the trap centre (see subsection 2.2.4).

independently-variable electrodes (see figure 2.1). The four cylindrical rods have a radius of 4 mm and are mounted with two PEEK insulating brackets, diagonally separated by $2r_0 = 7$ mm; the length of the four central electrodes is $2z_0 = 5.5$ mm. This linear cylindrical design (inspired by the Paul trap developed at Aarhus University by Drewsen and coworkers [102]) affords excellent optical access and a relatively large stable trapping region (see stability diagrams later in this section).

A saddle point potential periodically switching with frequency $f_{RF} = \Omega_{RF}/2\pi$ in the $x - y$ (radial) plane (see figure 2.2) is yielded by RF voltages ($V_{RF}(t)$) applied to the trap electrodes in a quadrupolar configuration, *e.g.* diagonal rods are in phase and adjacent rods have inverse phase (see equation 2.2). The ions are therefore confined in the radial plane if this saddle point flips faster than their motion in that plane.

$$V_{RF}(t) = V_{RF} \cos(\Omega_{RF} t) \tag{2.2}$$

To achieve three-dimensional trapping, static voltages (U_{end}) are superimposed on the endcaps to yield the axial (z-axis) confinement. Specifically, the traps utilised in our laboratory are operated at $2V_{RF} \in [200, 350]$ V, $U_{end} \in [0.5, 4]$ V, $\Omega_{RF} \approx 2\pi \times 3.82$ MHz. The theory of trapping charged particles with oscillating electric fields has been meticulously studied in the past [100]; the following paragraphs will highlight

the salient points of the theory related to linear Paul traps.

The resulting trapping field corresponds to an approximately harmonic potential ϕ. In the case of hyperbolic trap electrodes, the potential would be perfectly harmonic; for linear cylindrical rods, a geometric factor κ must be taken into account and characterised by matching the numerical simulations of the ensemble of trapped ions with the experimental images [88]. The resulting near-harmonic potential can be modelled with the following analytical expressions:

$$\phi_{\mathrm{RF}}(x,y,t) = \mathrm{V_{RF}}\ \cos(\Omega_{\mathrm{RF}}t)\left(\frac{x^2-y^2}{r_0^2}\right) \tag{2.3}$$

$$\phi_{\mathrm{end}}(x,y,z) = \frac{\kappa\ \mathrm{U_{end}}}{z_0^2}\left(z^2-\frac{x^2+y^2}{2}\right) \tag{2.4}$$

$$\text{where}\quad \phi(x,y,z,t) = \phi_{\mathrm{end}}(x,y,z) + \phi_{\mathrm{RF}}(x,y,t) \tag{2.5}$$

From Newton's second equation of motion, the dynamics of an ion held in an RF trap will follow:

$$m\vec{a} = \vec{F} = -Q\vec{\nabla}\phi(x,y,z,t) \tag{2.6}$$

where m and Q are the mass and the charge of the ion (respectively), whereas $\vec{a}$ and $\vec{F}$ are the acceleration and force vectors experienced by the ion. Therefore, considering equation 2.5, one can derive the following set of equations for the Cartesian components of the ion acceleration vector:

$$\frac{d^2x}{dt^2} = -\left(\frac{-\kappa Q\mathrm{U_{End}}}{mz_0^2} + \frac{Q\mathrm{V_{RF}}}{mr_0^2}\cos\left(\Omega_{\mathrm{RF}}t\right)\right)x \tag{2.7}$$

$$\frac{d^2y}{dt^2} = -\left(\frac{-\kappa Q\mathrm{U_{End}}}{mz_0^2} - \frac{Q\mathrm{V_{RF}}}{mr_0^2}\cos\left(\Omega_{\mathrm{RF}}t\right)\right)y \tag{2.8}$$

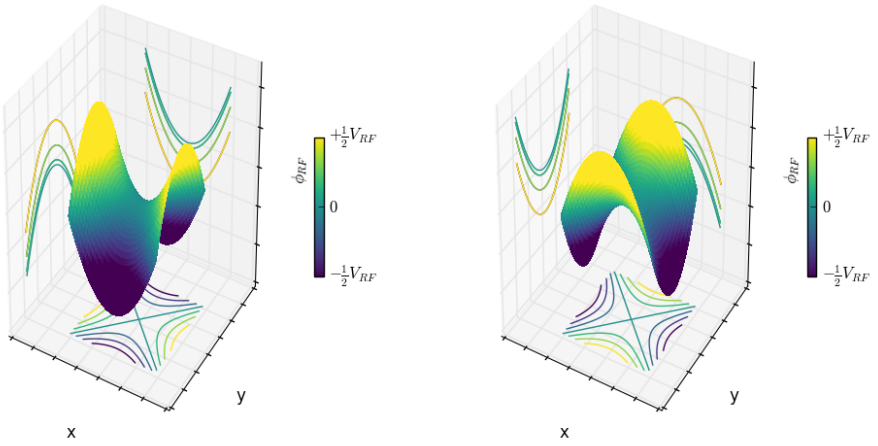

Figure 2.2: Graphs showing two instances of the saddle point potential periodically switching on the $x-y$ plane. In the left plot, the trapping well is oriented along the x-axis; whereas the plot on the right illustrates the opposite phase, with the confinement along the y-axis.

$$\frac{d^2z}{dt^2} = -\left(\frac{2\kappa Q \mathrm{U_{End}}}{mz_0^2}\right) z \tag{2.9}$$

By adopting the following substitutions

$$\tau = \frac{1}{2}\Omega_{\mathrm{RF}} t \tag{2.10}$$

$$a_x = a_y = -\frac{1}{2}a_z = -\frac{4\kappa Q \mathrm{U_{End}}}{mz_0^2\Omega_{\mathrm{RF}}^2} \tag{2.11}$$

$$q_x = -q_y = \frac{2Q\mathrm{V_{RF}}}{mr_0^2\Omega_{\mathrm{RF}}^2} \quad ; \quad q_z = 0 \tag{2.12}$$

it is evident that the one-dimensional differential equations of motion follow the paradigm of the well known Mathieu equation [109, 110]:

$$\frac{d^2u}{d\tau^2} + \left(a_u - 2q_u cos(2\tau)\right) u = 0 \tag{2.13}$$

It is convenient to describe the motion of the trapped ions in terms of the two dimensionless Mathieu parameters a and q (previously defined in equations 2.11 and 2.12), as the stability of an ion trajectory depends only on those two parameters and not on the ion initial conditions [110].

Under the adiabatic approximation [111, 112], the motion of a trapped ion can be split into two components: a low frequency *secular* motion and a higher frequency *micromotion* [113]. The secular motion refers to the thermal motion of the ion trapped in a time-averaged pseudopotential; this motion can be laser-cooled. The micromotion is induced by the dynamic switching of the RF potential; this oscillatory motion is proportional to the field strength. As such, it increases in amplitude with radial distance from the trap centre and vanishes along the trap axis (where the RF field is zero) [109]. In the case of hyperbolic Paul traps, there is only a single point of vanishing micromotion, so the linear cylindrical geometry offers a clear advantage (in addition to being easier to manufacture) for low temperature chemistry applications.

For unstable trajectories, micromotion exponentially increases with time and the ions are lost from the trap or collide into one of the electrodes. Stability diagrams can be generated in the $\{a, q\}$ parameter space, *i.e.* for certain values of $a_i,\ q_i$ with $i \in \{x, y, z\}$ there will be stable confined ion trajectories within the trap. Such stability maps can be obtained by analytically solving the Mathieu equations (or numerically via classical trajectory simulations of a discrete subset of $\{a, q\}$) (see figure 2.3).

The aforementioned pseudopotential treatment is an effective theoretical framework for modelling the ion motion and for establishing stability criteria. The pseudopotential consists of a time-indepenent effective potential V^* experienced by an ion in a stable trajectory, and it can be expressed as [112]:

$$V^*(\vec{R_0}) = \frac{Q^2\ \mathrm{V}_{\mathrm{RF}}^2}{4m{\Omega_{\mathrm{RF}}}^2} + q\Phi_{\mathrm{End}}\ , \tag{2.14}$$

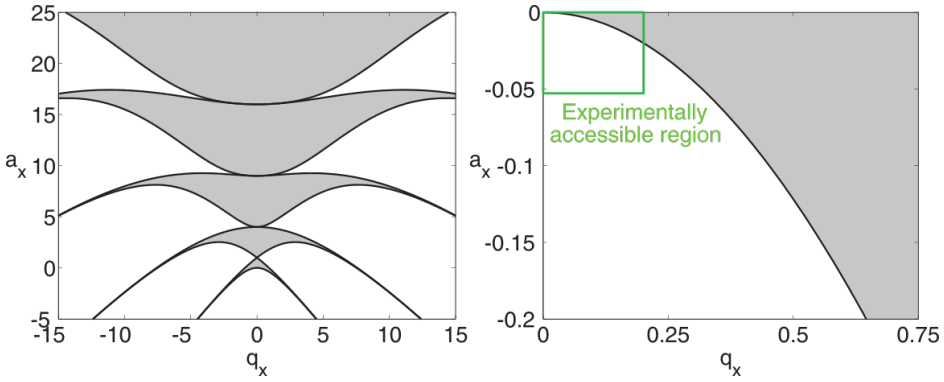

Figure 2.3: Typical one-dimensional (x-axis) stability diagram for an ion held in a Paul trap. Stable trapping is achieved by operating the trap so that the values of a and q fall within the grey areas enclosed by black lines. Figure reproduced from reference [88].

where $\vec{R_0}$ represents the coordinate for the "smooth"[1] stable trajectory, and the first term on the right-hand side represents the time-averaged contribution of the RF fields. As such, the secular stable trajectory $R_0(t)$ satisfies the following equation of motion:

$$m\frac{d^2}{dt^2}\vec{R_0} = -\vec{\nabla}V^*(\vec{R_0}) \tag{2.15}$$

From the pseudopotential equation 2.14, it can be seen that the effective radial confinement is stronger (steeper trapping walls) for lighter ions. This is a key point for understanding the spatial distribution of ions of different masses that are simultaneously trapped: lighter ions will appear in proximity to the trap centre, whereas co-trapped heavier species will be located farther away from the potential minimum (see multicomponent Coulomb crystals in subsection 2.2.3).

[1]Within the adiabatic approximation, the smooth secular motion is treated separately from the "wiggling" micromotion.

2.2 Ion trapping and Coulomb crystals

2.2.1 Laser cooling

Laser light can be used to slow down hot, confined atoms and ions (and, to a certain extent, molecules — albeit for a limited number of molecular species). The process, termed laser cooling, was formally proposed by Hänsch and Schawlow (for free particles) and independently by Wineland and Dehmelt (for trapped particles) [114, 115]; it was further developed (experimentally and theoretically) by Phillips [116], Chu [117], Cohen-Tannoudji and Dalibard [118].

The phenomenon relies on the wave-particle duality of photons, on the momentum change associated with the absorption of a photon and on the isotropy of the spontaneous re-emission of absorbed photons in free-space. Specifically, when a particle absorbs or emits a photon, the momentum of the particle changes according to the laws of conservation of momentum; the change of momentum at every scattering event is $\Delta\vec{p} = \hat{r}_\gamma \; h/\lambda$ which is equal in modulus to the momentum associated with a photon of frequency $\nu = c/\lambda$ propagating along $\hat{r}_\gamma$. The associated change in velocity at each event is given by the change in momentum divided by the mass of the particle: $\Delta v = h/(m\lambda)$.

Since the laser propagates along a fixed direction and there is no preferred re-emission direction, repeating the absorption-emission process over many cycles will provide a net effect which will increase or decrease the particle motion along the laser axis, depending on the relative movement of the particle and the photons that are absorbed/emitted. In order to increase the probability of deceleration, the laser wavelength is red-shifted from the wavelength resonant with the absorption transition, taking advantage of the Doppler effect. If the laser is detuned to a longer wavelength, the particles moving towards the laser beam have a higher chance of absorption, thus reducing the velocity of the particles counter propagating the laser beam path. The

method is commonly called Doppler laser cooling and was first demonstrated in 1978 using Mg^+ and Ba^+ [115].

To achieve low translational temperatures, it is optimal to have cooling lasers propagating along several orthogonal geometrical axes, in order to address directly all of the translational degrees of freedom. This is the base principle in optical molasses for cooling ensembles of neutral atoms in magneto-optical traps [119]. In this regard, laser cooling of ions has a clear advantage over neutral atoms: cooling is achievable simply with a laser propagating along a single direction (since the translational degrees of freedom of trapped ions are coupled by their Coulomb interactions); it is not a requirement that additional cooling lasers are employed, it simply makes the cooling process more efficient.

A strict requirement for performing Doppler cooling is the presence of a closed cycle, so that the absorption/re-emission process can be repeated quickly ($\sim 10^6$ cooling cycles are needed). For example, if after the addressed particle absorbs a photon and reaches an excited state $|2\rangle$, it subsequently decays to a (metastable) state different than the initial ground state $|1\rangle$, an additional laser will be required to re-pump the population back into the excited state $|2\rangle$ so that the "cooling" transition $|2\rangle \rightarrow |1\rangle$ takes place and the cycle is closed (with the re-emission of a photon $\gamma_{1,2}$).

Given the complexity of the energy diagrams for molecules, it is evident that finding a closed laser cooling cycle is not feasible for the vast majority of molecules. While there are various examples of molecular species that have been successfully Doppler cooled with relatively elaborate schemes [42, 120], sympathetic cooling (see subsection 2.2.3) remains the mechanism of choice for removing kinetic energy from co-trapped molecular ions.

As mentioned earlier in this section, the spontaneous emission of a photon is an isotropic process whereby the associated momentum change — $\Delta p = h/\lambda$ in a random direction $\hat{r}_\gamma$ — averages to zero when summed over the various cooling cycles. In

terms of momentum-space, this is equivalent to a random walk with step size h/λ (with the frequency given by the scattering rate) centred on the cooled particle's initial momentum (since $\langle \Delta p \rangle = 0$). However, this is not the case for the mean square displacement from this initial position, *i.e.* $\langle \Delta p^2 \rangle \neq 0$ and therefore the variance $\langle \Delta p^2 \rangle - (\langle \Delta p \rangle)^2 \neq 0$, corresponding to a non-zero speed term. This constitutes a limitation on the lowest translational temperature that can be achieved using only Doppler laser cooling [119]. This lower limit, termed the Doppler temperature limit, can be calculated from:

$$T_D = \frac{\hbar \Gamma}{2k_b} \,, \tag{2.16}$$

where Γ is the line-width of the transition (*i.e.*, the transition decay rate).

The experiments described in this thesis make use of low-translational temperature calcium ions that are trapped and laser-cooled. The adopted laser cooling scheme for $^{40}Ca^{+}$ was described by Ritter and coworkers [121] and is depicted in figure 2.4. A 397 nm diode laser excites the population of the calcium ions in their ground state, 4s $^2S_{1/2}$, to the 4p $^2P_{1/2}$ excited state, where the ion can either fluoresce back to the ground state (which represents the main cooling transition) or decay to the metastable 3d $^2D_{3/2}$ state, with a branching ratio of about 1:12 in favour of the ground state [88]. A laser operating at 866 nm is therefore needed to address the ions shelved in the metastable state 3d $^2D_{3/2}$, to re-pump the population back to the $^2P_{1/2}$ level and thus close the optical cycle.

2.2.2 Coulomb crystals

Trapped, laser-cooled ions undergo a phase transition to form a highly ordered structure referred to as a Coulomb crystal (or sometimes Wigner[2] crystal), when the po-

[2]Wigner proposed this structure for electrons back in the 1930s [64].

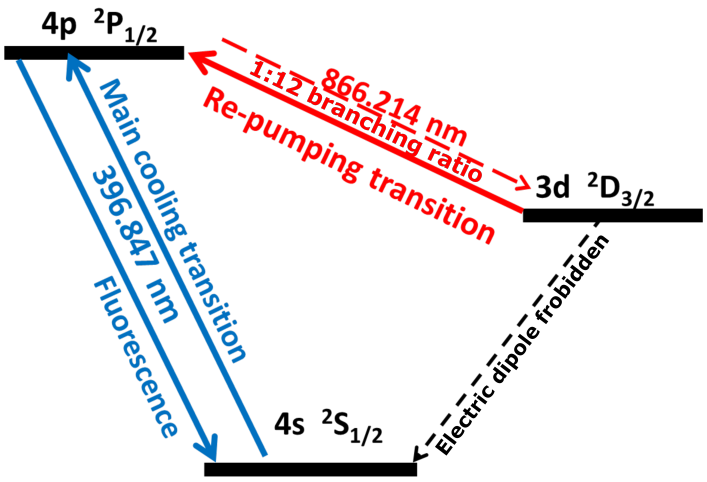

Figure 2.4: Diagram of the adopted $^{40}Ca^{+}$ laser cooling scheme showing the main cooling transition at 396.847 nm and the re-pumping transition from the 3d $^2D_{3/2}$ metastable state. The transition from 3d $^2D_{3/2}$ to the ground state 4s $^2S_{1/2}$ is electric dipole forbidden.

tential energy exceeds the kinetic energy of the ensemble. In the case of a linear Paul trap, the resulting Coulomb crystal structure is typically composed of concentric ellipsoidal shells (see figure 2.5). Interestingly, different crystal geometries and structures - ranging from single ions to 1D strings to 2D planes all the way up to 3D ellipsoids of several thousand ions - can be achieved by manipulating the trap parameters and by varying the number of ions trapped. Moreover, more exotic geometries, and "crystal" structures (e.g. fcc and bcc) have been numerically investigated by Drewsen and co-workers [122].

Notice that the term "crystal" seeks to acknowledge the lattice-like configuration, even though this structure has no true translational symmetry, is in the gas-phase, and can be more accurately described as a strongly-coupled non-neutral plasma [108]. The dimensionless coupling parameter Λ for such a one-component plasma derives from the ratio of the potential and kinetic energy of the ensemble (see equation 2.17); for values $\Lambda \geq 150$, a Coulomb crystal is formed.

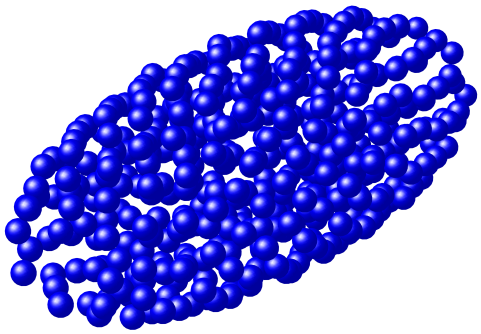

Figure 2.5: 3-dimensional rendering of a 400 ion Ca^+ Coulomb crystal, obtained via molecular dynamics simulations (see subsection2.2.4). Notice the typical ellipsoidal symmetry.

$$\Lambda = \frac{E_{\text{pot}}}{E_{\text{kin}}} = \frac{Q^2}{4\pi\epsilon_0 a_{WS} k_B T} \tag{2.17}$$

The Wigner-Seitz radius for such a localised structure is defined in equation 2.18 and is connected to the particle density n and therefore to the ion-ion distance.

$$a_{WS} = \left(\frac{3}{4\pi n}\right)^{\frac{1}{3}} \tag{2.18}$$

Considering the definition of the coupling parameter Λ and the condition $\Lambda \geq 150$, it can be derived that the inter-ionic distance in a Coulomb crystal is on the order of $\sim$10 – 20 μm [28]. It is worth noting that this value is about five orders of magnitude larger than the typical spacing observed in a solid state crystal. As such, Coulomb crystals exhibit an ion density of $< 10^9$ ions cm^{-3}.

2.2.3 Sympathetic cooling and multicomponent crystals

In addition to the directly Doppler-cooled ions, other ionic species (atomic or molecular) can be incorporated into Coulomb crystals. When other ions are co-trapped, they will interact (via the Coulomb force and the confining forces of the ion trap) with the laser-cooled ions comprising the Coulomb crystal. Kinetic energy of co-trapped ions can be removed via elastic collisions with laser-cooled ions, which essentially act as a heat sink. It is through this mechanism — called sympathetic cooling [123, 124] — that non-laser-cooled (atomic or molecular) ions can have their translational temperature reduced until they become incorporated into the cold lattice of ions that constitutes the Coulomb crystal [125, 126]. Sympathetic cooling is most effective for ions of a similar mass-to-charge ratio to the laser-cooled species; the optimal relative mass-to-charge ratios of the co-trapped species and the laser-cooled species is $\sim$0.4 $-$2.5 [108].

In contrast to these Coulomb interaction-mediated elastic collisions, inelastic collisions only become dominant at much shorter length scales than the ion-ion distances in the Coulomb crystals. As a result, the internal degrees of freedom of any sympathetically cooled molecular ions are not affected, and so their internal energy distributions remain in thermal equilibrium with the ambient black-body radiation (BBR), usually corresponding to room temperature $T_R \approx 300$ K [127, 108]. In experiments where the molecular reactants are prepared in a specific quantum state, the interaction of the BBR with the molecular ions can lead to the loss of population from a previously selected state. A broadly applicable (but technically challenging) approach to overcoming this problem is the adoption of a cryogenic ion trap whereby the presence of consecutive heat shields around the trap (kept at 4 K) prevents any room temperature BBR from scrambling the population of previously state-selected molecular ions. Moreover, the cryogenic trap can be operated with helium as a buffer gas to redis-

tribute the internal energy states so that only the lowest few states remain populated [57, 108].

It is worth noting that, owing to the sympathetic cooling, it is also possible to incorporate product ions generated from reactions occurring within the Coulomb crystal [126, 28]. This feature makes sympathetic cooling in linear Paul traps a versatile experimental protocol in the ion-neutral cold chemistry field.

2.2.4 Main aspects of Coulomb crystals

Shape and temperature

When discussing the $\sim q^2/m$ dependence of the pseudopotential, it was explained that lighter trapped species will experience a stronger confinement, whereas heavier ions experience a weaker trapping potential. As a result, when co-trapping species within a $^{40}Ca^+$ Coulomb crystal, ions with a mass-to-charge ratio $m/q > 40$ form ellipsoidal shells around the laser cooled ions. The Coulomb repulsion pushes the calcium ions so that their initially ellipsoidal configuration is distorted, thereby resulting in an elongated and flattened calcium ion framework (cf. panels (a) and (b) in figure 2.6). By contrast, species with a lower ratio (*i.e.* $m/q < 40$) form an ellipsoidal core inside the ensemble of calcium ions and push the heavier Ca^+ ions away from the trap axis (see figure 2.6 (d)).

By recalling that the micromotion is zero at the trap axis and increases with increasing radial distance from the axis, it is evident that there are different motional regimes across the various regions of a Coulomb crystal. Ions located along the trap central axis feature the lowest translational kinetic energy within the ensemble. As such, it is difficult to ascribe a single temperature to a Coulomb crystal, given the diverse range of properties for ions located at different positions. Moreover, Coulomb crystals are not a system at thermal equilibrium. It is, however, common in the

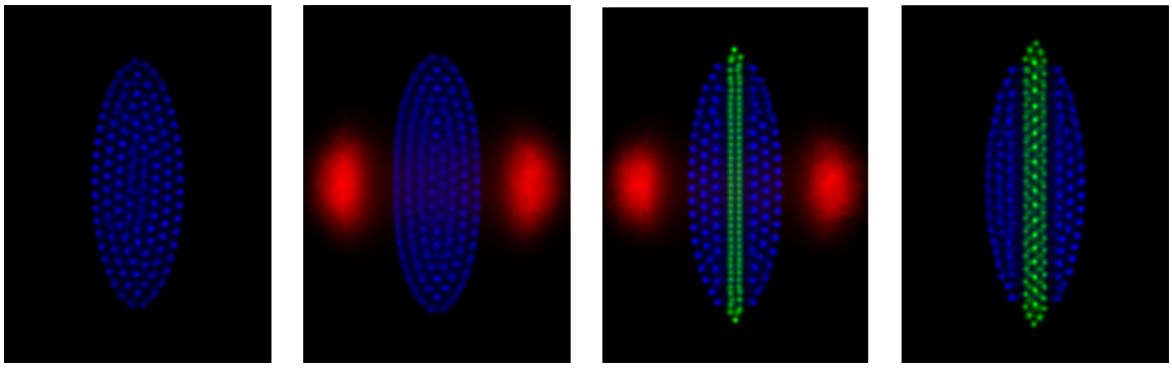

Figure 2.6: Simulated CCD camera false-colour images of multi-component Coulomb crystals (in the experimental images, only the LIF pattern (of Ca^+ ions) can be visualised). Panel (a) illustrates a Coulomb crystal formed by 600 Ca^+ ions. In panel (b) a bi-component crystal consisting of 600 Ca^+ (in blue) and 150 Xe^+ (in red) is shown. The image in Panel (c) corresponds to a multi-component crystal containing 600 Ca^+, 70 Xe^+, and 80 ND_3^+ (in green). Panel (d) depicts a bi-component crystal containing 600 Ca^+ and 150 ND_3^+.

literature to refer to the effective temperature of a Coulomb crystal as the average kinetic energy converted into Kelvin via $T = \langle E_{\text{kin}} \rangle / k_B$. The kinetic energy associated with the average micromotion for crystals of a few hundred ions is typically significantly higher than the secular motion, since only the secular motion can be laser cooled (see 2.1.1). For instance, adopting the definition of temperature set out above, a Coulomb crystal comprising $\approx$ 600 Ca^+ ions exhibits a temperature of $\sim$ 500 mK [7].

Imaging and manipulation

Laser-cooled ions will re-emit photons (and thus continuously fluoresce) during the laser cooling process. Consequently, one can exploit the laser-induced fluorescence (LIF) to monitor the lattice positions of individual laser-cooled ions in a Coulomb crystal by means of a charged couple device (CCD) camera and a magnifying objective lens[3].

Typically, the shallow depth of field of the camera-lens setup will allow one to bring

[3]In a Coulomb crystal, inter-ionic distances are on the order of $\sim$10$-$20 μm [28].

into focus only one transverse layer of the crystal, albeit with some blurring due to the contribution from adjacent layers. The camera focus can be adjusted to be at the central plane of the crystal, so that by considering the ellipsoidal symmetry one can reconstruct the entire ensemble. One can experimentally image the LIF pattern, but other non-fluorescing co-trapped species will not be visible on the CCD experimental images. However, the presence of "dark" ions can be often inferred from changes to the shape of the fluorescing framework.

Imaging Coulomb crystals is not only useful for carrying out data analysis (as explained later in this section), but also to optimise the numerous experimental parameters. The visual feedback is an invaluable resource to refine, for instance, the RF voltages, the static potentials and the cooling laser parameters, especially when utilising the apparatus after a long interval. If perfectly centred within the trap, the ensemble of laser-cooled ions will only radially expand or contract with respect to the trap axis (see figure 2.7 (I)) when decreasing or increasing V_{RF} (*i.e.*, the amplitude of the RF trapping potentials). Should the ensemble move in an asymmetric manner, DC bias voltages on the trap electrodes can be varied to manoeuvre the ions towards the real centre of the trap. Additionally, by either decreasing or increasing the axial trapping voltage U_{end}, the ensembles of ions will either axially elongate or compress, as shown in figure 2.7 (II). If this motion does not occur in a symmetric way, it is again an indication that the crystal is not perfectly centred in the trap. The ability to amend the trap electrodes' DC bias voltages allows one to centre the ensemble before starting an experiment. An exhaustive procedure for optimising the experimental parameters leading to the formation of Coulomb crystals can be found in the theses from previous group members [88, 7].

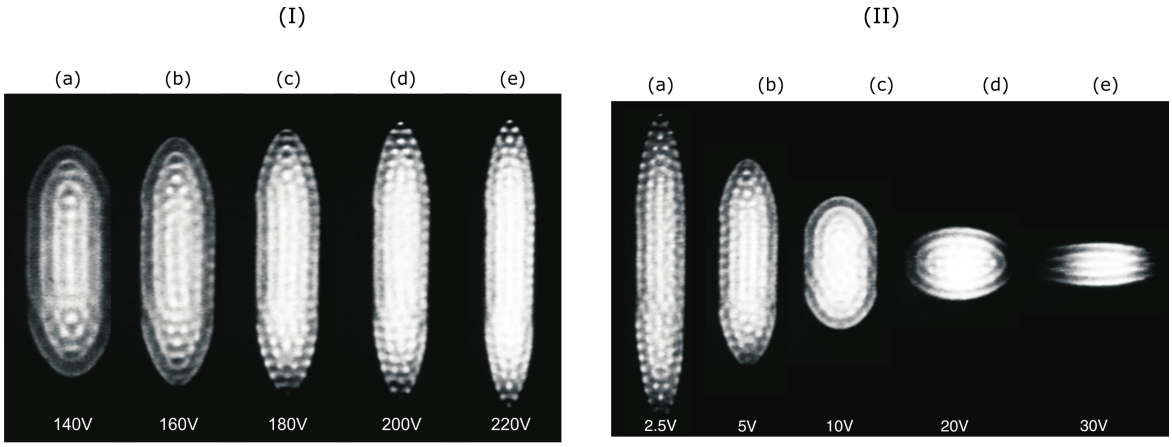

Figure 2.7: Experimental LIF images showing the manipulation of Coulomb crystals via the variation of the voltages applied to either the RF or to the endcaps. In panel (I) a sequence of CCD images of the LIF of Ca^+ Coulomb crystals recorded at increasing values of V_{RF}, whilst keeping U_{end} constant (at 4 V). The sequence in panel (II) shows the effect of varying U_{end} whilst keeping V_{RF} constant (at 180 V). Figures adapted from [88].

Molecular dynamics simulations

It is well established that molecular dynamics simulations of Coulomb crystals can facilitate the calculation of the rate coefficients [128]. Specifically, by emulating the dynamics of the ions within a Coulomb crystal one can obtain the lattice positions of the ions and thereby reproduce simulated images of the LIF framework of the crystal. One can then perform a comparative analysis between experimental LIF images and simulated images of LIF patterns in order to ascertain the Coulomb crystal volume and the number of ions [28].

A custom-made[4] molecular dynamics simulation software package (called "ccmd" for Coulomb crystal molecular dynamics) allows one to model Coulomb crystals in a linear Paul trap with parameters replicating the experimental conditions. Firstly, the code processes a formatted input[5] text file ("`trap.info`") to retrieve the experimen-

[4]Originally written in C++ programming language by M. Bell, the program has been later adjusted and improved by various members of the group and by the Oxford ARC facility.

[5]Typical input parameters can be found here: [129]

tal conditions of the experiment to be simulated. These parameters include the ion trap features (geometry, voltages, frequency), the information regarding the trapped species (masses, numbers and whether they are directly laser-cooled or sympathetically cooled), and the imaging characteristics (number of pixels, pixel-to-micron ratio, depth of focus, blurring).

In each simulation, the program generates an ion cloud whereby each ion is positioned randomly on a 3-dimensional grid within the trapping region. All ions are assigned a zero initial velocity. Subsequently, the code calculates the net force $\mathrm{F_{Total}}$ experienced by each of these ions:

$$\mathrm{F_{Total}} = \mathrm{F_{Trap}} + \mathrm{F_{Coulomb}} + \mathrm{F_{Cooling}} + \mathrm{F_{Heating}} \tag{2.19}$$

Hence, $\mathrm{F_{Total}}$ is computed by considering the following contributions: the trapping force $\mathrm{F_{Trap}}$ (which encodes the interaction of the ion with the Paul trap fields), the Coulomb force $\mathrm{F_{Coulomb}}$, a force term related to the cooling mechanism $\mathrm{F_{Cooling}}$, and a heating force term $\mathrm{F_{Heating}}$ modelling the heating due to photon-recoil or collisions with background gas in the trap.

Then, Newton's equations of motion are computed for each ion via a reversible reference system propagation algorithm (RESPA); the Verlet numerical integration method provides the ions velocities and positions at a each time-step [130]. The routine is repeated numerous times so that at each iteration, after updating the forces and accelerations, the ions are propagated over a small time-step. It should be noted that fast-changing forces (*e.g.* $\mathrm{F_{Trap}}$) are updated at each integration time-step, whereas slow-changing forces (*e.g.* $\mathrm{F_{Coulomb}}$) are re-evaluated every "`respastpes`" time-step (an optimal balance between accuracy and speed was found for `respastpes`=5). After a certain number ("`CoolPeriods`") of iterations, the code starts storing the data of the positions in order to build two 3-dimensional histograms. The algorithm continues

iterating for a "`histperiods`" number of time-steps before generating an image. It should be noted that, in order to mimic the shallow depth of field of the imaging setup, a Gaussian blur is applied prior to producing the simulated image.

The simulated images are sequentially compared with the experimental LIF images utilizing the software GIMP [131] and ImageJ [132]; details on the imaging analysis procedure can be found in the following theses written by previous group members: [133, 134, 129].

2.3 Experimental configurations of the ion traps

The work described in this thesis has involved the use of two ion traps, with both adopting the same aforementioned design in combination with two different sources of cold neutral polar molecules (see chapter 3). Both traps feature a trap depth $\sim$1.36 eV and are operated with trapping parameters in the range $2V_{RF} \in [200, 350]$ V, $U_{End} \in [0.5, 4]$ V, and $\Omega_{RF} \approx 2\pi \times 3.82$ MHz. The only differences arise from the specific configurations and geometries adopted for interfacing the ion traps with the two cold neutral molecule sources, described in the following subsections.

2.3.1 The Stark decelerator experiment ion trap

One linear Paul trap is combined with a Stark decelerator, and is located at the centre of a custom-built cylindrical (diameter $\approx$ 36.5 cm, height $\approx$ 26.5 cm) reaction chamber (see figure 2.10). The reaction chamber is operated at ultra-high vacuum (UHV) condition: a baseline pressure P $\approx 7 \times 10^{-10}$ mbar is achieved using a rotary pump-backed turbomolecular pump (Leybold Turbovac 361).

In order to reach the UHV regime, the chamber is baked at 180 °C for $5 - 10$ days. This baking step is essential when changing the reactant species to be studied (to neutralise the environment), or whenever the ion trap chamber is pumped down

following venting or chamber opening. This process removes contaminants, particularly water and nitrogen that can adsorb onto the metallic surfaces. To further reduce the probability of reactive collisions with background contaminant species, it is possible to operate a cold finger. Such a heat-exchange device, consists of a series of turns of copper tubing through which liquid-nitrogen-cooled N_2 gas is flowed to freeze out gaseous contaminants present in the chamber. Additionally, low-mass background impurities (primarily hydrogen) are reactively removed by means of a titanium sublimation pump, operated for 1 minute at nominal firing intervals of 8 hours. A residual gas analyser (RGA, Stanford Research Standard 100) allows for an accurate reading of the various contaminants present in the chamber and is also used to perform diagnostic leak tests.

An oven [6] is resistively heated to about 600 – 900 K through the application of a current of $\approx$ 8 A, yielding an effusive beam of atomic calcium. The Ca beam passes through a $\approx$1 mm slit to reduce the divergent portion of the beam; a mechanical shutter is utilised to prevent calcium deposition[7] on the trap when not loading. When the chamber pressure rises to $\approx 1 \times 10^{-9}$ mbar, the shutter is opened so that the calcium beam can reach the ion trap for loading. At the trap centre, Ca atoms are non-resonantly ionised with 355 nm photons from the frequency-tripled output of a pulsed Nd:YAG laser (featuring 5 ns pulses and 10 Hz repetition rate). When the beam alignment and power (approximately 5 mJ/pulse) is optimised, typically $\sim 5 - 20$ laser pulses are admitted to form enough ions for a standard-sized Coulomb crystal ($\sim 100 - 400$ ions).

All the laser beams enter the chamber through the same view-port, which is equipped with a Brewster window (see figure 2.9) and located approximately 30 cm from the trap centre. The laser beams then pass through an iris inside the chamber

[6] AlfaSource Calcium 225 mg, purtiy 99,8%, outer diameter 3 mm, length 98 mm, type F.

[7] The deposition of calcium on the trap electrodes can cause patch potentials that affect the nearly-harmonic characteristic of the trapping fields.

prior to reaching the trap; both the Brewster window and the irises before and after the trap serve to minimise any stray light reflections.

In order to laser cool the trapped $^{40}Ca^{+}$ ions, the outputs of the 397 nm and 866 nm continuous wave (CW) diode lasers[8] are sent through the trap axis by means of optical fibres and fibre-couplers (the fibre coupling serves to improve their beam profiles). After passing through the trap, an array of mirrors allows one to re-send the beams back thorough the trap, thus providing laser cooling in the opposite direction. A wavemeter interfaced to both diode lasers via an optical fibre switcher[9] enables one to effectively monitor the wavelengths of the lasers simultaneously. A `LabVIEW` [135] program controls the tuning and locking of the diodes to a specific wavelength.

A CCD camera and 10x microscope objective lens are mounted on an $x - y - z$ translation stage located on the top of the ion trap chamber to image the ion fluorescence through a quartz view port perpendicular to the trap axis (see figure 2.8). Finally, a flight tube and a micro-channel plate (MCP) detector are located perpendicular to the trap axis, diametrically opposed to the Stark decelerator side. The ion detection through time of flight mass spectrometry is detailed in chapter 4.

2.3.2 The Stark guide experiment ion trap

An almost identical Paul trap has been combined with a buffer gas cell and electrostatic guide source. It was designed and built mainly by L. Pollum, a former member of the Softley group [133], with the intention of combining it with the buffer gas cooled Stark guide [8]. There were nonetheless a few compatibility issues that arose during the combination phase, which were addressed by E. Steer and myself. As shown in figure 2.11, the trap is held at the centre of a significantly smaller cylindrical reaction chamber (measuring ≈15 cm in diameter and ≈14 cm in height) compared to the

[8]Respectively, a Toptica DL 100 Pro and a Toptica DL 100. Laser line widths are on the order of several MHz.

[9]Wavemeter model: High-Finesse WS-U. Optical fibre switcher model: Leoni M1x2 SI50/125.

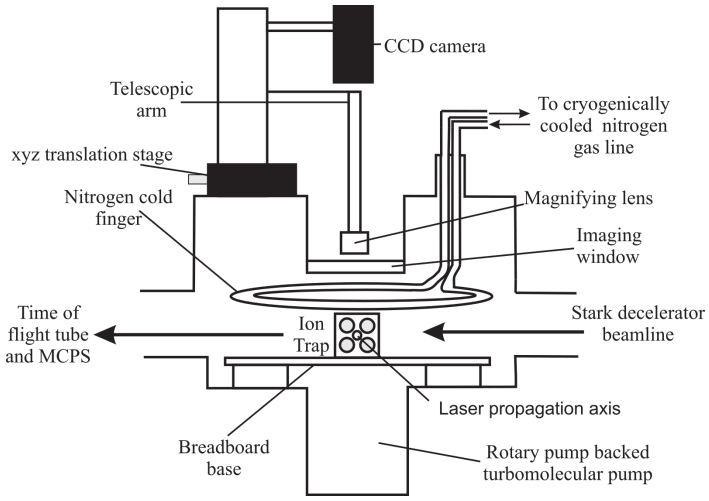

Figure 2.8: Schematic side view of the ion trap chamber adopted for the experiment involving a Stark decelerator. The laser propagation axis is orthogonal to the paper. Figure reproduced from reference [7].

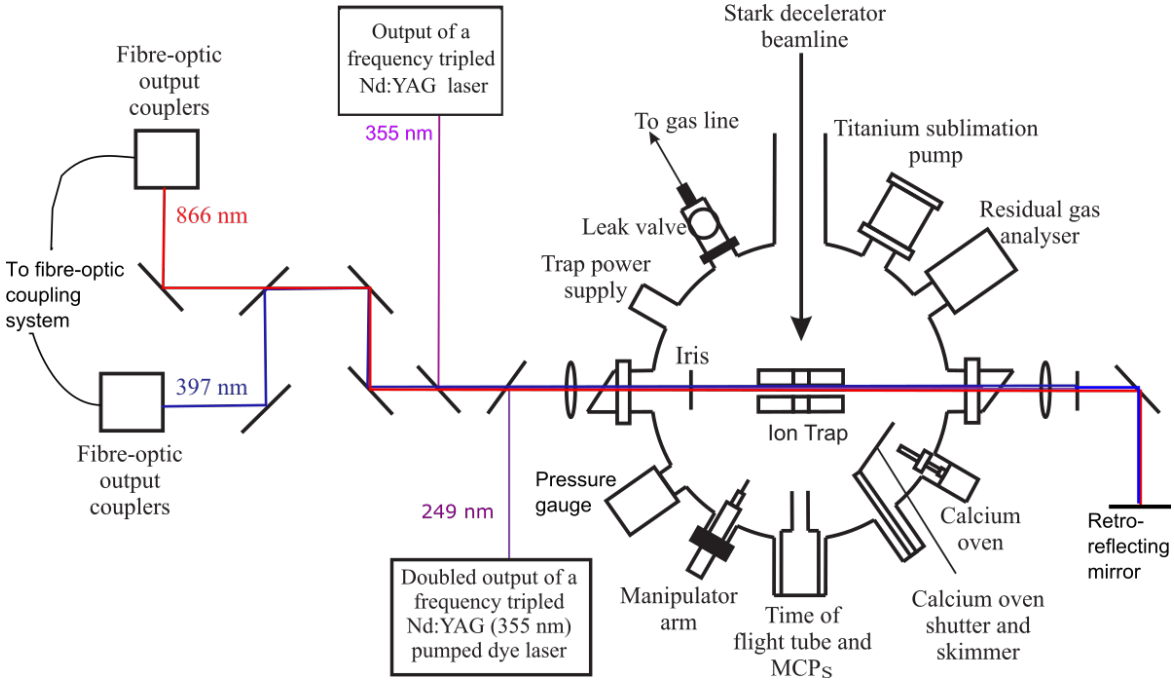

Figure 2.9: Schematic top view of the ion trap chamber adopted for the experiment involving a Stark decelerator. The CCD camera imaging plane is parallel to the paper. Figure reproduced from reference [136].

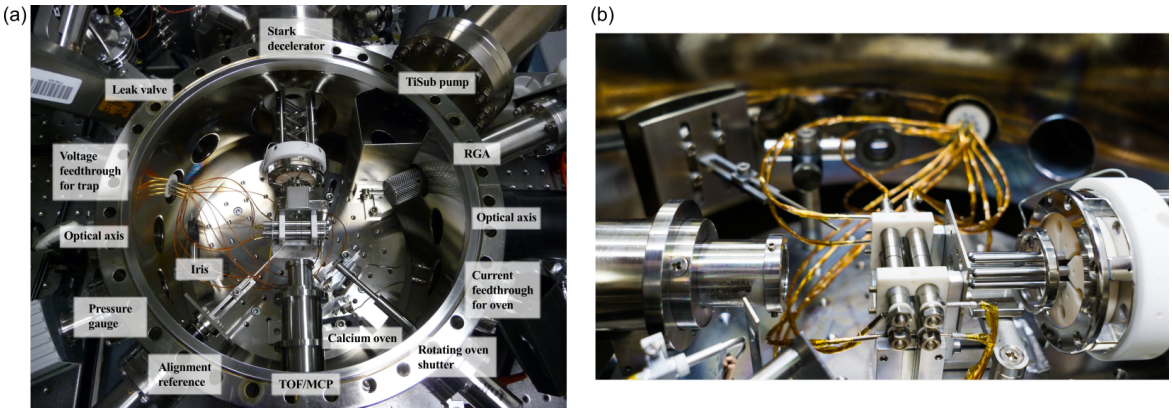

Figure 2.10: (a) Photograph of the top view of the ion trap showing the various components of the apparatus [133]. The picture in panel (b) shows the side view of the trap. The final hexapole of the Stark beamline and the time of flight tube of the detection setup are clearly visible on the right and left side of the trap (respectively).

Stark decelerator ion trap chamber; the ion trap is vertically separated from the end of the guide by a distance of 14.85 mm (see section 3.3.2 for more details). Whilst the reduced dimensions of the chamber allow for more efficient pumping and fewer surfaces on which contaminants can stick, it also translates into restricted access to the trap components, thus making the various maintenance operations more challenging.

Owing to a differential pumping stage (separating the reaction chamber from the rest of the Stark guide vacuum chamber) and the presence of two rotary pump-backed turbomolecular pumps, the nominal pressure in the trap chamber is $\sim 5 \times 10^{-10}$ mbar. The small trap chamber volume means that only a few days of baking are required to regain UHV conditions following a vacuum break (for diagnosis or replenishing the Ca oven). The production of the neutral calcium effusive beam for loading the trap is carried out via resistively heating a tantalum[10] wire wrapped around a ceramic sleeve surrounding a Ta tube containing grounded Ca powder (and aligned such that the tube opening is directed towards the trap centre). As a consequence of the favourable properties of Ta, flowing a small current $\lesssim 2$ A is sufficient to produce an effusive

[10]Tantalum was chosen by virtue of its high resistivity and thermal conductance but low thermal expansion [133].

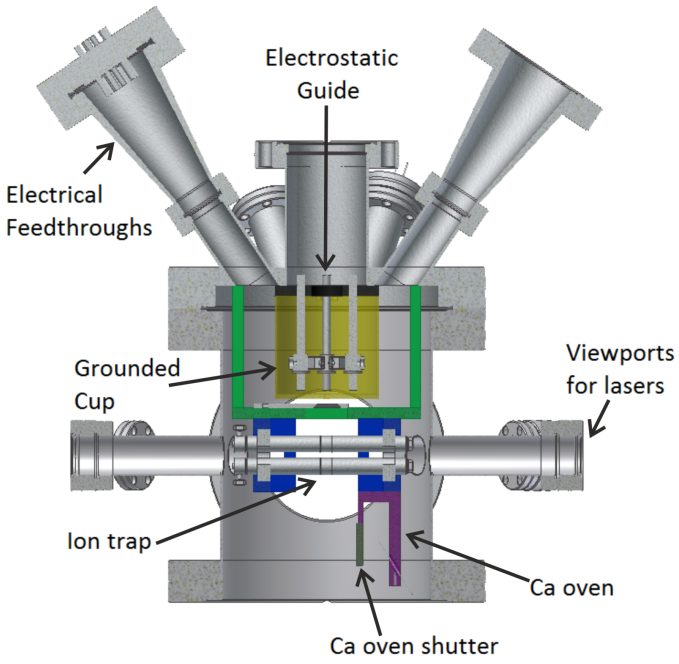

Figure 2.11: Schematic side view of the ion trap chamber adopted for the experiment with an electrostatic guide combined with a buffer gas cell. Figure reproduced from reference [137].

beam of Ca atoms. Between the trap and the oven tube there is a plate with a 1 mm diameter hole which serves to skim the effusive beam and prevent Ca deposition on the trap electrodes.

Due to the orientation of the end of the Stark guide (see section 3.3.2) — which guides the flow of polar molecules downwards and into the ion trap region — the top of the ion trap could not be used for imaging as in the other setup (the trap combined with a Stark decelerator). As a result, ion fluorescence is monitored from the side (in the laboratory frame) but still perpendicular to the trap axis.

The quartz side view port for imaging the fluorescence of the ions measures 25 mm in diameter. As in the other ion trap, ions are imaged through a 10x objective lens. A 3-axis translation stage supports a CCD camera[11] and a photomultiplier tube[12] (PMT)

[11]Model: Andor Luca DL-658M-TIL.
[12]Model: Hamamatsu H10721P-110.

which are mounted perpendicular to one another in order to share the same field of view through a beam splitter. The beam splitter sends the majority (24 : 1 ratio) of the light to the CCD camera. The reason is twofold: the PMT is more sensitive than the CCD but does not have imaging capabilities; the PMT is used only for initially searching for fluorescence, whereas it is the CCD that provides experimental data for the imaging analysis.

There are three additional vacuum chamber ports with a direct line of sight to the trap and one of these is used for ion detection. Another port is aligned with the trap axis and is employed for laser cooling (both the 397 nm and 866 nm light). The final port, located at 30° to the trap axis, is assigned to the ionisation beam (either 355 nm for ionising calcium or 325 nm for ammonia); this port is also used for introducing a radial laser cooling beam (in addition to the axial cooling beams) to improve the efficiency of the laser cooling process.

In this chapter, the properties and design of a laser cooled ion trap producing a source of cold ions have been discussed. The following chapter is concerned with the properties and design of two sources of cold neutral molecules, which when combined with the ion trap allow the study of cold ion-neutral reactions.

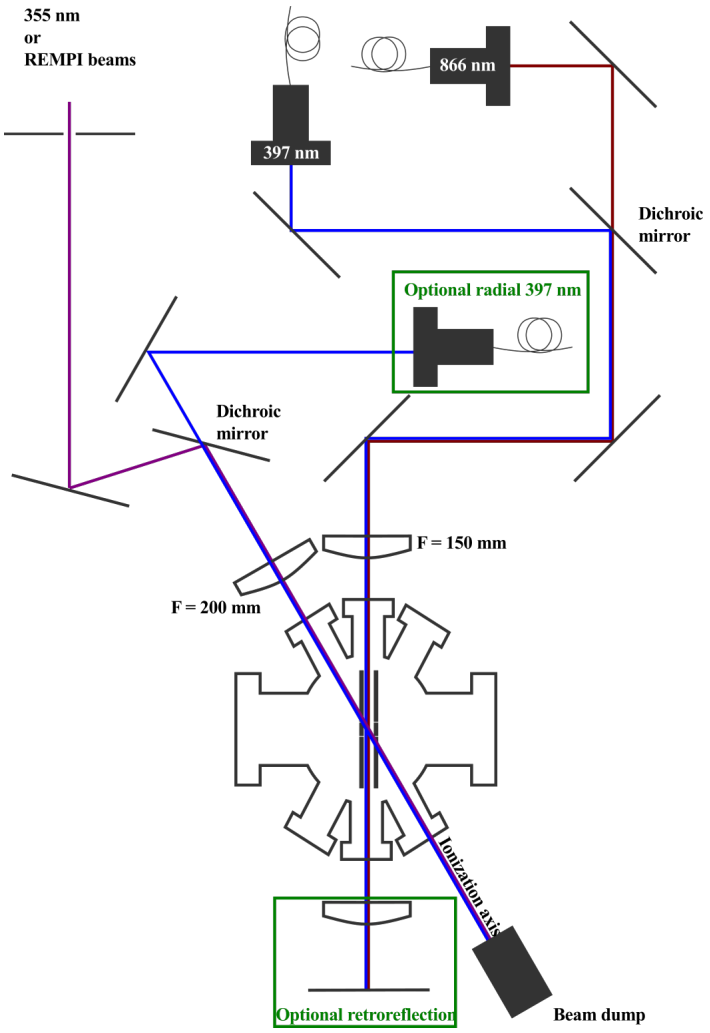

Figure 2.12: Schematic top view of the ion trap chamber adopted for the experiment with an electrostatic guide combined with a buffer gas cell. Figure reproduced from reference [133].

Chapter 3

Sources of cold molecules

3.1 Controlling polar molecules via the Stark effect

The work described in this thesis was carried out using two different experimental set-ups. This chapter provides details about these two complex apparatuses, each of which comprises an ion trap and a source of cold molecules to facilitate the study of ion–molecule reactive collisions. The ion traps of both experimental set-ups share the same design, as described in sub-section 2.1.1. Only minor differences are present (see section 2.3) and these are mainly due to the need for combining the traps with the different cold molecular sources.

Both molecular sources rely on the electrostatic Stark effect and therefore act on polar molecules. The Stark effect describes the shifting and splitting of the quantum energy levels in the presence of an external electric field; the Stark effect removes the m-degeneracy of the rotational energy levels of polar molecules. Figure 3.1 (a) shows the splitting of the M-level for $J = 1$ and for different values of K (where J is the total angular momentum, K represents the projection of J on the main molecular axis, and M is the projection of J along the external field axis).

The Stark effect arises from the interaction between the polar molecule dipole

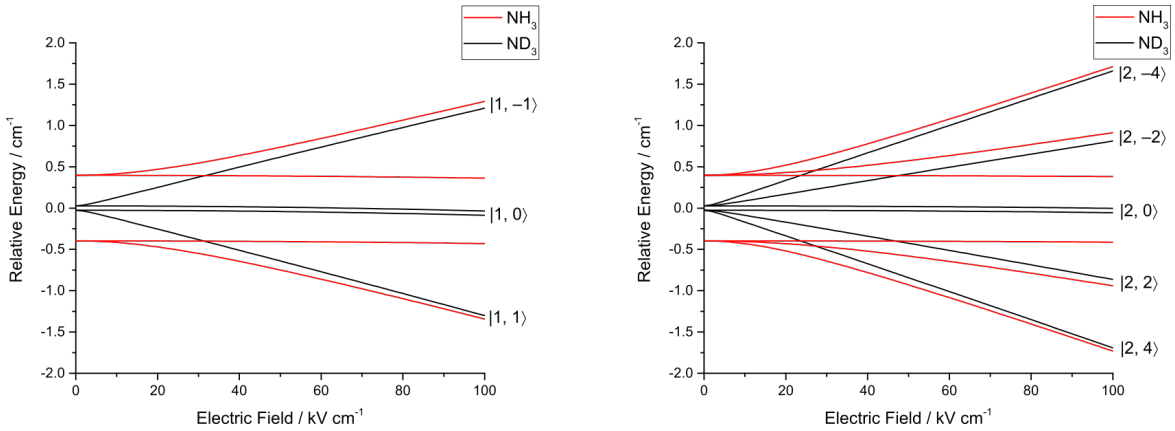

Figure 3.1: ND_3 and NH_3 energy level diagrams depicting the splitting of the M-degeneracy for different K-values for the J=1 state (panel (a)) and for the J=2 state (panel (b)) [137].

moment $\vec{\mu}$ and an applied electric field $\vec{E}_{\text{ext}}$, which in quantum mechanics is expressed as an additional term in the total energy operator $\tilde{H}_{\text{tot}}$:

$$\tilde{H}_{\text{Stark}} = -\vec{\mu} \cdot \vec{E}_{\text{ext}} \tag{3.1}$$

This extra interaction term can cause the energy of the polar molecule to either increase or decrease in the presence of an applied electric field. Those quantum states for which the Stark potential energy increases with increasing field strength are referred to as low-field-seeking (LFS) states; high-field-seekers (HFS) are those states whose energy decreases in increasing electric field strength.

It should be noted that M and K are not good quantum numbers individually when high electric fields are present. However, since the expectation value of the scalar product in equation 3.1 is proportional to $MK/(J(J+1))$, the product MK constitutes a suitable quantum number. For this reason, the various LFS states are normally labelled with the ket notation $|J, MK\rangle$.

Both the Stark decelerator and the Stark bent guide experiments operate by addressing polar molecules in LFS states. This is because species in LFS states seek to

minimise their Stark energy and so are repelled from regions of high electric fields. This allows one to control molecular trajectories with a force term acting upon polar molecules, derived from the Stark potential energy (see equation 3.1).

3.2 The Stark decelerator experiment

A Stark decelerator [138] is interfaced with a linear Paul trap to facilitate the study of tunable-collision-energy, quantum-state-selected ion-molecule reactions at low temperatures. In a Stark decelerator, the kinetic energy of polar molecules in LFS states is converted into Stark potential energy and subsequently removed from the system as the molecules enter regions of rapidly switching high voltages (see figure 3.2).The amount of kinetic energy removed from the beam is determined by the exact time sequence of the applied electric field pulses (see subsection 3.2.2).

3.2.1 Decelerator features

The Stark decelerator was developed by previous members of the group [139], and is based on the design introduced by G. Meijer [140]. Specifically, this decelerator is 715 mm in length and consists of a linear array of 132 pairs of parallel electro-polished stainless steel cylindrical electrode rods mounted on alumina supporting rods. These electrodes are 3 mm in diameter and feature a 2 mm gap between the rods of each pair. Adjacent pairs are perpendicular to each other and are separated by a distance of L =5.5 mm. High voltages of $\pm$10 kV are applied to every second pair of electrodes, whilst neighbouring pairs are grounded. These high voltages are then rapidly switched, yielding a time-dependent inhomogeneous electric field along the decelerator (see figure 3.2 (b)). The voltage switching sequence is timed so that, at each deceleration stage, polar molecules in LFS states experience an upward slope of the Stark potential energy.

Figure 3.3 shows the various sections of the cold molecular source; molecules are

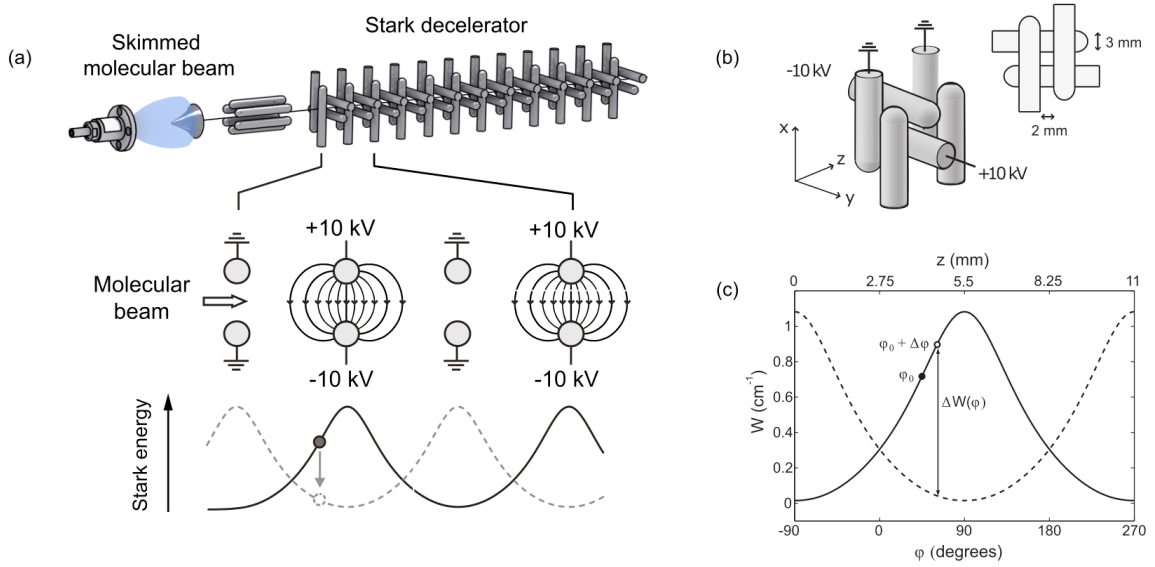

Figure 3.2: (a) Pictorial view of the Stark decelerator and its operating principle. Panel (b) depicts the detailed configuration of two adjacent pairs of electrodes. Panel (c) visually explains the phase angle parameter. Figures adapted from [139].

admitted into a source chamber via supersonic expansion through a pulsed valve. In the source chamber, held at a nominal pressure of approximately 2×10^{-7} mbar, a pulsed solenoid valve[1] is backed with 3 bar of carrier gas (xenon) and $\sim 5-10\%$ seeded gas (ammonia). This valve is operated at 10 Hz and with a pulse width of 160 μs. When running the experiments, the pressure in the source chamber increases up to $\sim 1 \times 10^{-5}$ mbar.

Following the supersonic expansion, the beam passes through a region of free flight (25 mm in length) and then accesses the decelerator chamber (nominal pressure $5-9 \times 10^{-9}$ mbar) through a 1 mm diameter skimmer. Once skimmed, the beam is focused into the Stark decelerator by a hexapole located 20 mm after the skimmer; this is the first of the three hexapoles present along the decelerator beamline. The first two hexapoles have a length of 60 mm, whereas the final hexapole is 10 mm longer. All

[1]General Valve 99 series.

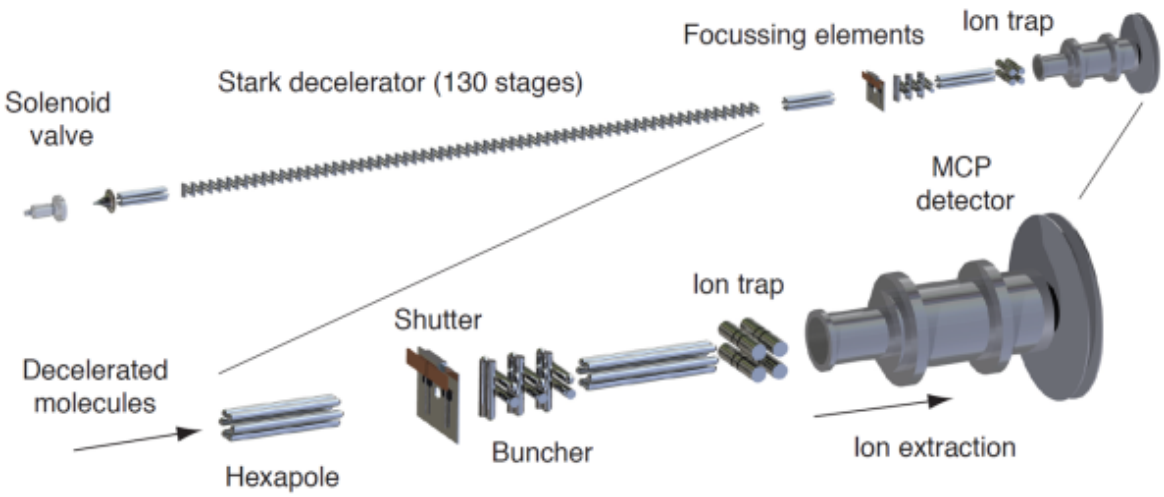

Figure 3.3: Schematic of the Stark decelerator apparatus and the other elements interfaced with it, including the Paul trap and the detection setup. Figure adapted from [7].

the hexapoles have a radius of 10 mm and adjacent hexapole rods have an applied voltage of typically ± 10 kV via pulses lasting 150 μs. The hexapole rods are made of electro-polished stainless steel, have a diameter of 4 mm and are mounted on MACOR insulators to suppress conduction between opposite phase poles. The second and third hexapoles reside after the 132 decelerator electrodes and just before the ion trap (their roles are discussed later in this section).

The 132 pairs of electrodes yield a total of 131 deceleration stages. Voltages (typically ranging from $\pm 5 - 10$ kV) are applied to a given pair of electrodes whilst the two adjacent electrode pairs are kept at $\simeq 0$ kV. It is important to note that there is a small DC bias voltage of ≈ 100 V constantly superimposed on the decelerator to prevent regions of zero field and thus to suppress non-adiabatic transitions between different MK states [141]. Four fast high voltage switches[2] serve to turn the electrodes on/off according to a sequence calculated via a `MATLAB` [142] code and sent to a DAC unit interfaced with the switches.

[2]Belke Electronic GmbH, HTS-150 PGSM

At a distance of 32 mm after passing through the 131 deceleration stages, the beam encounters a second hexapole that focuses the beam into a "buncher" stage (described in detail later in the paragraph) and through a fast opening shutter[3]. The shutter (opening time of 800 μs) serves to remove the undecelerated portion of the beam; without the shutter, the undecelerated particles would arrive before the decelerated particles of interest and would react with the trapped species in the reaction chamber. The buncher, located 42 mm after the shutter, serves the role of longitudinal phase space focusing [143]. It is 55 mm in length and features a design analogous to the decelerator, however it only consists of 6 pairs of electrodes (instead of 132) and these have twice the dimensions of the decelerator rods. After the buncher, the beam travels into the reaction chamber (nominal pressure 7×10^{-10} mbar, see section 2.3), passing through the third and final hexapole (that focuses the beam into the centre of the Paul trap (see figure 2.10 (b)). In order to electrically shield the ion trap from the high voltages emanating from the Stark decelerator beamline, a grounded mesh (supported by a stainless steel cubic element) is present between the final hexapole and the ion trap.

The inclusion of hexapole focusing elements in the beamline design is to address the transverse expansion of the beam — which would reduce its density — during regions of free flight outside the decelerator stages. Conversely, the buncher elements have the ability to reduce the axial expansion of the beam. As such, the buncher can increase the density of the beam packets at the centre of the ion trap. This spatial bunching is at the expense of a greater velocity spread. Alternatively, the buncher can be operated in a velocity-focussing mode to yield a narrower velocity distribution (at the expense of a greater spatial spread) to facilitate a finer control over the collision energy with the target of trapped ions [7].

[3]Uniblitz LS6TF-ECE

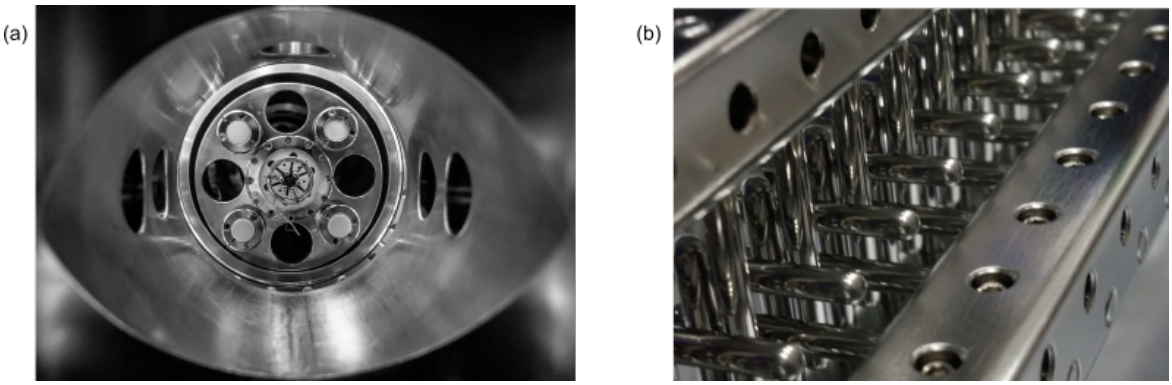

Figure 3.4: (a) Photograph of the Stark decelerator first hexapole. (b) Photo of the sequence of pairs of the Stark decelerator electrodes showing the orthogonal configuration in detail.

3.2.2 Operating mode

In order to establish a switching time sequence for the Stark decelerator, it is useful to consider the motion of a hypothetical molecule in a LFS state (often called synchronous particle) along the main axis of the decelerator (z-axis) starting from the centre of the first pair of grounded electrodes. The trajectory of the synchronous particle is selected so that it experiences constant kinetic energy loss at each deceleration stage.

For characterising the synchronous trajectories, it is common to use the phase angle parameter ϕ, which serves to indicate the axial position of the synchronous particle at which the voltages are switched (see figure 3.2 (c)). Given the periodicity of the assembly of pairs of electrodes, this angular parameter proves to be useful in establishing the amount of Stark potential energy gained at each stage. The phase angle is defined as:

$$\phi = \frac{z - L/2}{L}\pi \ , \tag{3.2}$$

where z is the axial coordinate starting in the middle of the grounded pair of electrodes located immediately behind the travelling synchronous particle and L is the distance between adjacent electrode pairs.

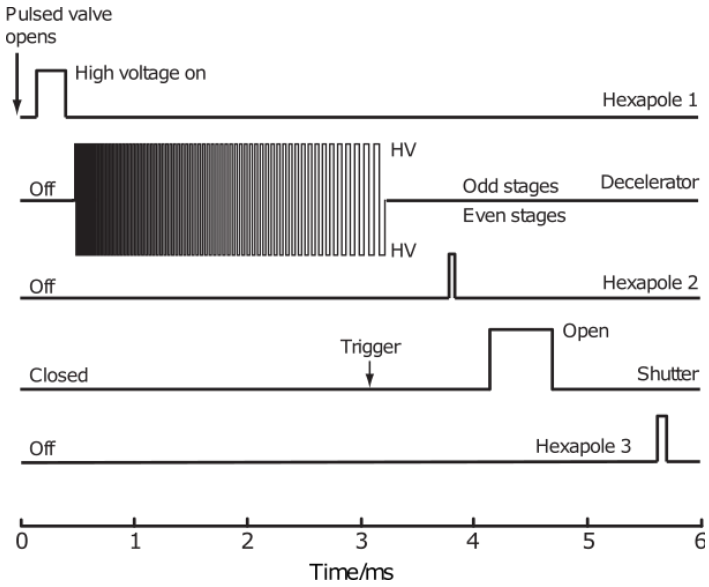

Figure 3.5: Typical switch time scheme for the Stark decelerator voltages sequence. Figure reproduced from reference [144].

In this framework, $\phi = 0°$ denotes a situation when the voltages are switched every time the synchronous particle is in the middle of two sets of electrodes pairs. Hence, the particle will experience the same amount of deceleration and acceleration over a switching cycle. For values of $\phi > 0°$, the particle will climb up a potential energy hill prior to switching, thus experiencing an average deceleration at each stage. A phase angle of 90° involves switching the fields such that the maximum amount of kinetic energy is removed at each stage. Figure 3.5 shows a characteristic switching sequence of voltages applied to the various components of the Stark decelerator beamline.

In order to avoid drawing high currents and damaging the apparatus, high voltage conditioning is conducted with extreme care following a routine derived during the characterisation of this setup. For details on the conditioning process please see reference [7].

It should be noted that the Stark decelerator beamline can also be operated using static voltages $\pm V_{\mathrm{DC}}$, with V_{DC} in the range $0 - 8$ kV. This protocol does not yield any overall deceleration but does focus and guide the beam into the ion trap. The

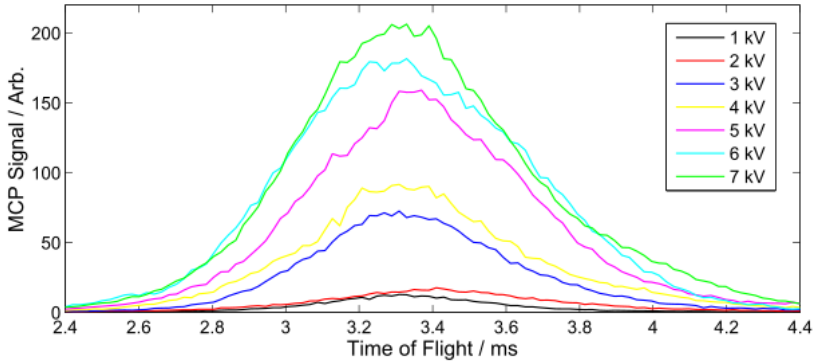

Figure 3.6: Time-of-flight signal of ND_3 guided to the ion trap centre, probed (via REMPI) at different guiding voltages in the range $\pm$ 1 – 7 kV. It is evident that the flux of guided ammonia molecules increases with increasing guiding voltages over this range. Figure reproduced from reference [7].

resulting beam is not translationally cold, but is still internally cold due to the initial supersonic expansion process. The static voltages yield a transversal confining Stark potential (see subsection 3.3.2), thereby electrostatically guiding all molecules in LFS states along the straight path of the beamline toward the ion trap. Since adjacent pairs of electrodes are orthogonal to each other, the transversal confining potential is present along both the x and y axes. This means that the loss of particles from the beam decreases with increasing V_{DC}. In figure 3.6, the intensity of the guided beam of ND_3 at the centre of the trap recorded via time-of-flight mass spectrometry is shown for different values of the guiding voltages [7].

3.2.3 Performance details

Time of flight measurements of ND_3 have been conducted by previous members of the group in order to characterise the performance of the Stark decelerator (at a phase angle $\phi_0 = 60°$) [139, 7]. A frequency-doubled pulsed dye laser[4] (317 nm in wavelength and $\approx$ 7 mJ/pulse in power) is focussed at the centre of the Paul trap. By means of

[4]DCM dye, pumped by a frequency-doubled Nd-YAG laser at 532 nm with a 5 ns pulse length and a repetition rate of 10 Hz.

(2+1)-REMPI[5] spectroscopy, accessing the $B(\nu = 5)$ intermediate electronic state, the 317 nm light selectively ionises ND_3 molecules at the trap centre. DC voltages of +300 V and +190 V are applied, respectively, to the front and rear vertical pairs of electrodes constituting the ion trap. In this way (see section 4.3), the electrodes accelerate the ions towards a free-flight tube before impinging on a MCP for detection.

Using this detection setup the deceleration of ND_3 has been monitored from an initial velocity of ~ 380 ms^{-1} to a final velocity of ≈ 130 ms^{-1} (thus removing ≈89% of the initial average kinetic energy) [7]. At this velocity, the resulting beam will have an average translational energy corresponding to a temperature of $T_{\mathrm{Trans}} \approx 20$ K. Characterisation of the beam via (2+1) REMPI spectra fitted with PGOPHER software[6] has indicated an internal beam temperature of $T_{\mathrm{Rot}} \approx 5$ K [144].

3.3 The Stark guide experiment

This experiment features a buffer gas cell interfaced with an electrostatic quadrupole guide, which is combined with an ion trap. Figure 3.7 (a) shows an overview of this unique experimental apparatus. The combined apparatus was built to investigate reactions between cold ions held in a Paul trap and translationally and internally cold neutral polar molecules coming from the electrostatic guide. As such, this apparatus constitutes the logical upgrade of a setup previously utilised in this research field [28], where no buffer gas cell was present, and therefore the molecular reactants were internally "warm".

The source of rotationally and translationally cold polar molecules was constructed and characterised by M. Bell and K. Twyman [139, 8], using a design inspired by the previous work of G. Rempe and co-workers [146, 147]. The source was characterised

[5]Resonance-enhanced multi-photon ionisation (REMPI) spectroscopy is discussed in detail in section 5.2.

[6]The PGOPHER spectral fitting and simulation software package has been developed by Western and is described in reference [145].

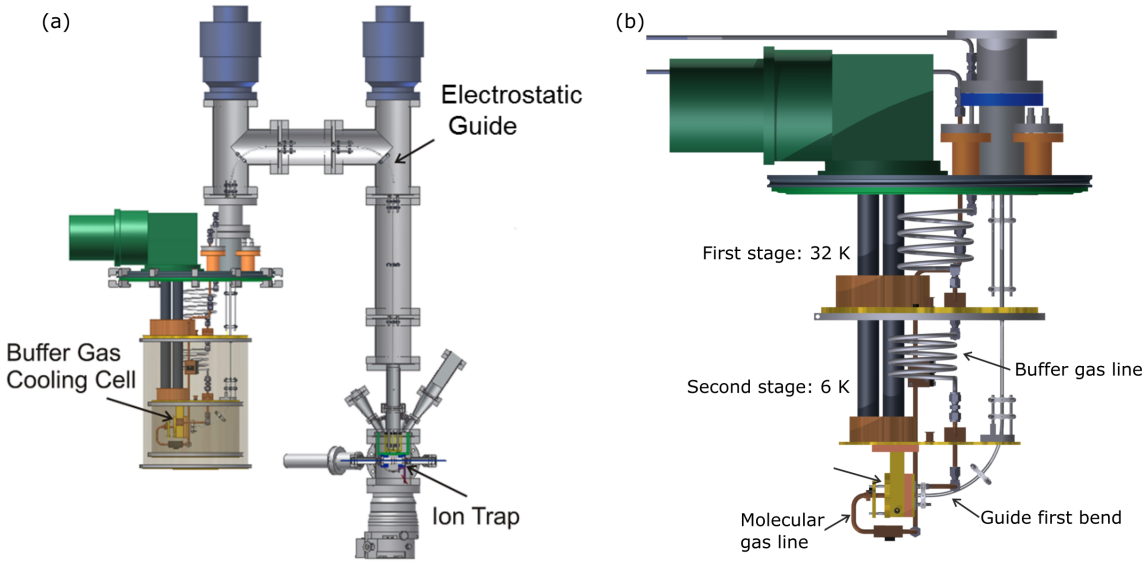

Figure 3.7: (a) Schematic diagram of the Stark guide experiment. Molecules enter the buffer gas cell (located in a 6 K cryostat) and thermalise with the buffer gas via elastic and inelastic collisions. Molecules then travel through a 2.1 m long three-bend electrostatic quadrupole guide which filters only the slowest portion of the molecular beam. As a result, only translationally and rotationally cold polar molecules reach the Paul ion trap, where reactions are examined. (b) CAD detail of the interior of the cryostat revealing the cryocooler stages, the buffer gas line and the molecular gas line connections to the buffer gas cell. The initial section of the guide with the first bend is also visible.

and optimised by previous group members [8, 137], with the molecular beam flux optimised to yield densities sufficient for performing ion-molecule reactions [8]. The following sections will describe the various components of this source of neutral polar molecules. The ion trap component of this set-up has been discussed in the previous chapter (see subsection 2.3.2) and was integrated with the cold molecular source at a later stage by Steer and myself [137].

3.3.1 Buffer gas cell

Within the buffer gas cell, molecules of interest undergo collisions with a buffer gas (typically helium) in a cryogenic environment. The internal state populations of the

molecules of interest thermalise through collisions with the buffer gas, reaching a new thermodynamic equilibrium with low rotational and translational temperature distributions (see figure 3.8 (b)).

The buffer gas cell is located at the second stage of a 2-stage low vibration cryostat[7]. The first stage reaches 32 K, with then an inner heat shield separating it from the internal second stage that is held at 6 K (see figure 3.7). The two heat shields are made out of copper, externally gold-plated (to prevent oxidation) and internally covered in activated charcoal (this carbon coating acts as a helium trap at low temperatures, thus keeping the pressure low in the high vacuum regions of the cryostat). The smaller shield encloses the cell and the second stage of the cryostat; the outer shield surrounds the entire cryocooler in the main cryostat chamber.

The buffer gas cell is a cuboid measuring 40 mm × 40 mm × 20 mm (height, length and depth) and is made of oxygen-free copper, which ensures excellent thermal conductivity and uniform temperature environment (minimal chances of temperature gradients); one of the faces of the cell is actually made of Kapton[8] film. The cell features three ports respectively for buffer gas filling, molecular gas loading and for effusion towards the electrostatic guide.

Buffer gas is admitted through a 6.3 mm diameter orifice in the cell wall after travelling into the cryostat region through a copper gas line. The line is mounted to the two stages of the cryostat via copper fitting blocks to ensure efficient thermalisation with the cryogenic environment before the gas reaches the cell. The line features two coiled sections made of stainless steel; both the material and the longer path were chosen to reduce the conduction of heat from the main cryostat chamber to the second stage of the cryocooler [8].

The flow of buffer gas is controlled by a thermo-mechanical leak valve in combina-

[7] A two-stage pulse-tube cryocooler from Sumitomo Cryogenics (RP-082B) with a water-cooled 50 Hz compressor unit (F70 HV).

[8] Poly-oxydiphenylene-pyromellitimide (Kapton) features low thermal conductivity.

tion with a pressure gauge. For achieving efficient cooling of the admitted molecules, it is imperative to obtain an optimal flow rate of buffer gas. In particular, if the buffer gas flow is too low, sufficient collisional cooling will not occur; if the flow is too high, the buffer gas may impede the passage of the molecules of interest effusing through the cell exit orifice.

Molecules of interest are admitted into the buffer gas cell via a gas line which is thermally disconnected from the the cryogenic cell to prevent heating of the cell or freezing (and consequently, obstruction) of the flow in the gas-line. Despite this elaborate design of the gas line, it is still possible for gas in the molecular line to freeze, thus leading to blockage of the flow. To address this, two heaters have been placed along the molecular line.

The molecular flow for loading the cell is governed by a commercial mass flow controlling device[9] which operates in the flow range between 0.1 – 5.0 cm^3 min^{-1} (otherwise referred to as sccm: standard cubic centimetre per minute). As discussed for the buffer gas flow, it is necessary to find an efficient operating regime that balances the need for a high flux, and efficient collisional cooling. When characterising the setup with a quadrupole mass spectrometer [8], it was found that the optimal operating conditions for the experiments were 1 sccm ND_3 with 0.6 mbar of He in the buffer gas cell kept at 6 K and with guiding of voltages of $\pm$ 5 kV.

The continuous effusive beam of cold molecules that exits the buffer gas cell subsequently enters the first portion of the electrostatic quadrupole guide (see section 3.3.2). A rotary pump-backed turbomolecular pump and the aforementioned activated charcoal coating ensure the pressure in the cryostat is $\approx 10^{-6}$ mbar to afford a negligible collision rate between the guided particles and the background gas in the first guide section passing through the cryostat chamber.

[9]Bronkhorst F-200CV-002-AAD-22-E.

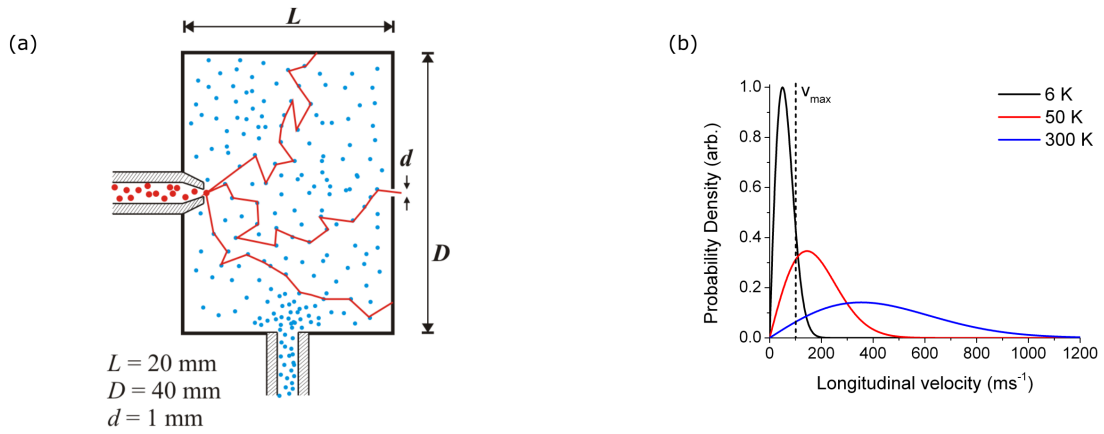

Figure 3.8: (a) Pictorial view depicting the buffer gas cell operating principle. Hot ($150 - 300$ K) molecules (in red) enter the gas cell and reach a thermal equilibrium with the buffer gas (blue) by means of collisional cooling. These molecules then exit the setup through a small aperture leading to the electrostatic guide entrance. (b) Plot of the Maxwell-Boltzmann velocity distributions for an effusive beam of ND_3 at three different temperatures (6 K, 50 K, 300 K). It is evident that if the samples undergoes buffer gas cooling, there will be more "slow" molecules that will make it through the velocity filter constituted by the electrostatic guide. Figures reproduced from [8].

3.3.2 Electrostatic quadrupole guide

The Stark guide consists of four hand-polished stainless steel rods, 2 mm in diameter and arranged as a quadrupole (with 1 mm separation between adjacent electrodes). Straight sections are combined with three 90° bent sections where the actual velocity filtering happens. The overall length of the guide is 2148 mm and the gaps present for joining straight and bent sections are less than 1 mm. Every 16 cm along the length of the guide, there are ceramic (Macor) insulators that hold the rods together and prevent rods of opposite polarity from arcing (see figure 3.9 (b)).

The guide passes through three differentially pumped regions, starting at a higher pressure ($\leq 10^{-6}$ mbar) in the cryostat and reaching the ultra high vacuum regime ($\leq 1 \times 10^{-9}$ mbar) in the trap chamber where the guide terminates after a final straight section of 69.3 cm. The centre of the ion trap is located at a distance of 14.85 mm from the end of the guide. A grounded stainless steel cup with a small opening covered

by Ni mesh (88% transmittance) encases the portion of the guide that extends into the ion trap chamber. This shields the trapping region from the high electric fields emanating from the guide.

Voltages of up to ± 5 kV are applied to the guide, yielding electric fields reaching 100 kV/cm near the surface of the guide rods (see figure 3.9 (a)). When applying high voltages to the electrodes, a cautious conditioning process must be performed reaching voltages up to ± 6 kV to ensure that the guide reliably holds the chosen high DC voltages without arcing or electrical breakdown [137].

The quadrupolar arrangement of the guide rods yields a low field region in the centre of the guide when high voltages are applied to the rods. Consequently, polar molecules in LFS states seek to remain in the centre of the guide in order to minimise their potential energy (see figure 3.10). In the region of a bent section of the guide, the (radial) trapping potential is steadily distorted and the potential minimum is gradually rotated by 90° in the lab frame. Only polar molecules in LFS states with a centrifugal force that is less than the centripetal force (arising from the Stark effect), will be guided around the bend. Specifically, the following guiding condition holds:

$$F_{\mathrm{Centr}} < \nabla W_{\mathrm{Stark}} \approx W_{\mathrm{Stark}}/r \quad , \tag{3.3}$$

where W_{Stark} is the Stark energy (i.e.,$-\vec{\mu}\cdot\vec{E}_{\mathrm{ext}}$), and $r = 1.12$ mm is the inner radius of the quadrupole. The approximation $\nabla W_{\mathrm{Stark}} \approx W_{\mathrm{StarK}}/r$ holds for molecules featuring a linear Stark shift, as in such cases $W_{\mathrm{Stark}} = -\mu_{\mathrm{eff}}|\vec{E}_{\mathrm{ext}}|$ [148]. From the equation of rotating bodies, the centrifugal force can be calculated as $F_{\mathrm{Centr}} = mv^2/R_{\mathrm{bend}}$, where $R_{\mathrm{bend}} = 100$ mm is the radius of curvature of the guide bent section. Combining these equations leads to the value of the maximum velocity that can be guided:

$$v_{max} = \sqrt{\frac{W_{Stark}\ R_{bend}}{m\ r}} \tag{3.4}$$

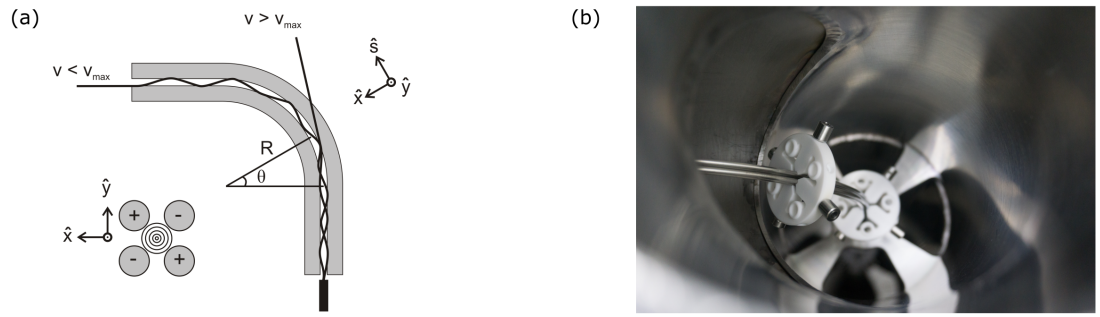

Figure 3.9: (a) Schematic view of one of the bent section of the guide. Only molecules in LFS states with a velocity under a certain threshold will make it around the bend. (b) Photograph of a bent section of the electrostatic guide.

When operating the guide at ±5 kV, for the lowest lying LFS state $|J, MK\rangle = |1, -1\rangle$ of ND_3, this threshold velocity is 240 m/s. Operating the guide at a lower voltage decreases the maximum velocity threshold, although it will also decrease the confinement and thereby the beam intensity at the end of the guide.

While the guide has three bends in total, characterisation experiments and simulations found that it is the first bent section that provides the entire velocity selection [8]. The second and third bends merely serve the role of directing the cold molecular beam into the ion trap chamber (see figure 3.7 (a)).

It is important to remember that the electrostatic guide does not perform any active cooling/deceleration of the sample; rather, it achieves a selection of the already present (post-buffer gas cell) translationally-cold molecules.

3.3.3 Performance details

In order to characterise the electrostatically guided buffer gas cooled beam, Twyman *et al.* established the rotational cooling effect provided by the buffer gas cell using REMPI spectroscopy (see section 5.2) and assessed the translational temperature via time of flight mass spectrometry [8, 149]. Characterisation of the beam via (2+1)

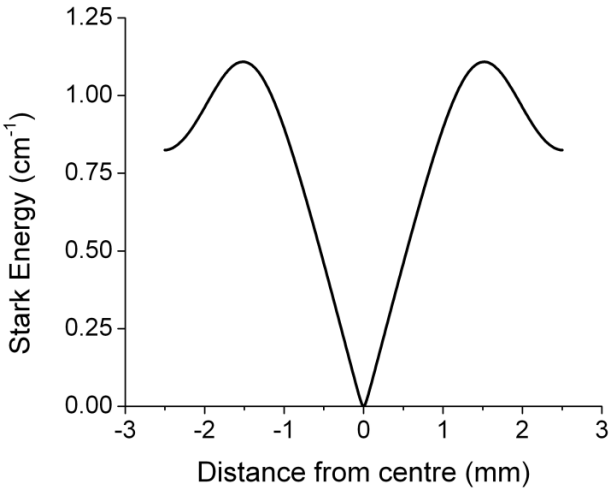

Figure 3.10: The graph shows the trapping potential energy experienced by a ND_3 molecule in the LFS state $|J, MK\rangle = |1, -1\rangle$ passing through the guide. Polar molecules in LFS states seek to remain in the centre of the guide rods in order to minimise their Stark potential energy. Figure reproduced from [8].

REMPI spectra fitted with PGOPHER was conducted for different buffer gas cell temperatures. Operating the setup without the outer heat shield (see subsection 3.3.1) allows one to conduct studies at higher temperatures. It was demonstrated that this apparatus can produce a beam of ND_3 molecules with rotational temperatures tunable in the range $9-18$ K and – crucially – at a near-constant translational temperature. As such, one can use the buffer gas cell and guide set-up to study the effect of rotational state distribution on the resulting ion-molecule reactions. [149]. Figure 3.11 shows experimental REMPI spectra and simulated PGOPHER spectra for a beam of ND_3 measured (under two sets of buffer gas cell conditions) at the end of the guide at the position of the ion trap. When the cell is operated at 6 K with helium, the ND_3 beam features a rotational state population corresponding to a temperature of 9 K; operating the cell with neon at 17 K yields a ND_3 beam with a rotational state population corresponding to a temperature of 15 K.

In order to measure the velocity of the beam, the setup was operated by pulsing

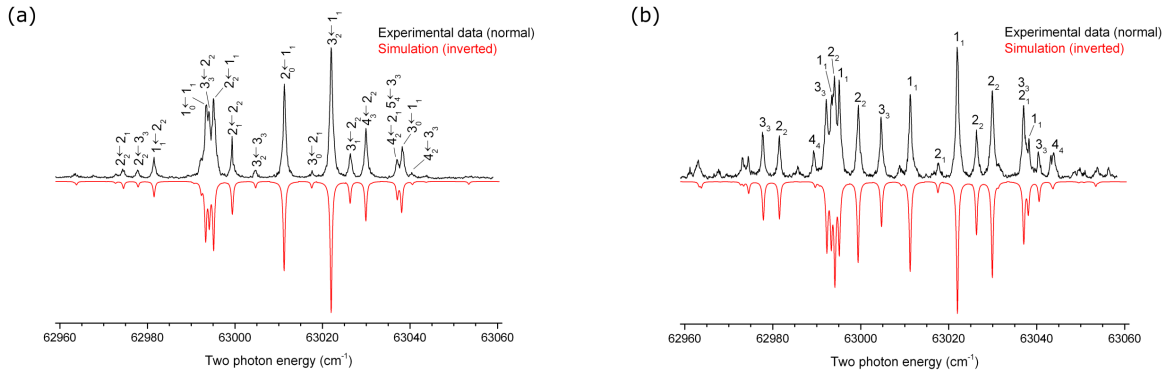

Figure 3.11: Experimental (above) and simulated (below) (2+1) REMPI spectra for the $\tilde{B}$ $(v = 5) \longleftarrow \tilde{X}$ $(v = 0)$ transition in ND_3. Panel (a) corresponds to the cell operated with helium at 6 K. The analysis provides a $T_{rot} \approx 9$ K. In panel (b) the cell is operated with neon at 17 K; analysis confirms a $T_{rot} \approx 15$ K. Figures reproduced from [8].

the electrostatic guide according to an asymmetric square wave signal (see figure 3.12 (a)). In this way the source is no longer continuous, thus allowing one to measure the velocity of the guided beam via time-of-flight mass spectrometry. The graph in figure 3.12 (b) shows the velocity distributions of the final beam of ND_3, obtained in three different regimes. When operating the cell with helium at 6 K, the ND_3 velocity distribution peak is at 75 ms^{-1}; when using neon at 17 K as the buffer gas, a comparable peak velocity of 70 ms^{-1} is achieved [149].

This constitutes an extremely useful feature for cold chemistry studies, as it allows one to probe just the effect of internal cooling by operating the experimental setup at different rotational temperatures whilst keeping constant the other experimental conditions (e.g., translational temperature of the molecular beam).

3.4 Summary

As described in this chapter, two sources of cold polar molecules have been combined with linear Paul traps to to provide the capability to examine reactive collisions at low

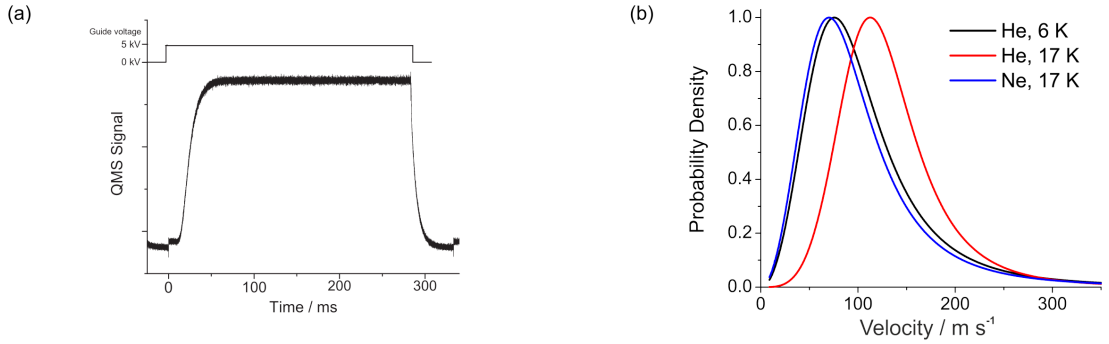

Figure 3.12: (a) Experimental mass spectrometry trace of the guided flow of molecules when pulsing the guide with a square wave. This procedure of pulsing the guide with a digital wave allows one to measure the velocity distribution to characterise the apparatus. Panel (b) shows the measured velocity distribution of guided ammonia previously cooled in a buffer gas cell operated at three different regimes. Notice the similarity of the measurements obtained using the cell with helium at 6 K and with neon at 17 K. Figures reproduced from [137].

temperatures. Both sources rely on the Stark effect, nonetheless they show remarkable complementarity. While the Stark decelerator is a pulsed, tunable energy source that allows state selectivity, it applies strict limitations in terms of the species that can be efficiently decelerated. However, this setup enables one to unravel the individual contribution of a selected quantum state on the reactive collisions in a Coulomb crystal for different collision energies.

Conversely, the Stark guide experiment is a continuous source of translationally and internally cold molecules. Given the high versatility of the buffer gas cooling and velocity selection, the Stark guide setup enables one to broaden the scope of low temperature reactions that can be investigated in the laboratory. For instance, the Stark guide apparatus could (in principle) be used to probe the reaction $NH_3^+ + ND_2H \rightarrow NH_4^+$ (NH_3D^+) + ND_2 (NDH) whilst varying the rotational temperature in the range 9 – 20 K. The branching ratio between the protonated and the deutereted product channel could be therefore examined at different temperatures to understand the mechanism of deuterium fractionation (of significant importance in astrochemistry

[150]).

In this chapter, the properties and design of two sources of cold polar molecules have been discussed. These cold molecule sources have been combined with Paul traps to facilitate the study of cold controlled ion-molecule reactive collisions. The following chapter is concerned with the characterisation of a recently developed detection method for quantitative investigation of ion-neutral reactions at low temperatures.

Chapter 4

Damped cosine trap detection method

This chapter is devoted to the characterisation of a novel detection method, which provides a quantitative analysis of the Coulomb crystal composition – details that are required for the calculation of reaction rate coefficients. The work presented here has been published as an article in Journal of Physical Chemistry A. [151]. My role in this project involved the collection of the experimental data with the damped cosine trap in conjunction with extensive simulations with the aim to characterise and test the performance of the new detection setup.

4.1 Techniques for Coulomb crystal detection

Reactions within a Coulomb crystal framework can be studied via imaging analysis by monitoring the laser-induced fluorescence (LIF) of the laser-cooled ions held in the trap. By comparing the experimental fluorescence pattern with images obtained from molecular dynamics simulations, it is possible to establish the number of reactant and product ions as a function of time [28, 152]. This approach is based on

the assumption that the crystal exhibits cylindrical symmetry about the trap axis, with uniform density throughout. The main limitation of comparing simulated images with experimental images is the inability to unambiguously identify the masses and abundances of the non-fluorescing ions ("dark" ions). Given the properties of multicomponent Coulomb crystals illustrated in chapter 2, reactions involving only two ionic species, one lighter than the laser-cooled ion and one heavier, can in principle be studied solely via LIF imaging analysis (*e.g.*, $OCS^+ + ND_3 \rightarrow OCS + ND_3^+$ or $Xe^+ + ND_3 \rightarrow Xe + ND_3^+$, within a Ca^+ Coulomb crystal) [7, 136]. In these cases it is possible to see the growth of an apparently hollow core (in the LIF pattern) as the reaction proceeds in the crystal and unambiguously ascribe the dark (non-fluorescing) region to specific product ions

For more complex reactions — for example, where there are multiple product pathways (and hence multiple product ions) — a quantitative detection method is essential. An accurate and quantitative method enables one to unambiguously ascertain the masses and abundances of all ions in the crystal at a given time. To this end, various quantitative detection techniques have been developed within this research field to complement imaging analysis.

For instance, resonant-excitation mass-spectrometry is a non-destructive detection method that relies on the different mass-related frequencies of secular motion of the trapped ions [153, 154]. In this technique, a weak axial RF field is added to the RF trapping field and varied while monitoring the emitted fluorescence to establish the motional frequency spectrum of the trapped species. Since ions absorb energy at certain frequencies according to their mass-to-charge ratio a visible decrease in fluorescence amplitude occurs when the additional RF field matches the secular motion frequencies. Drewsen *et al.* successfully applied this *in situ* MS technique to characterise the consecutive products of the photodissociation of a single $C_6H_5NH_2^+$ ion [155]. It must be noted, however, that large and multi-component Coulomb crystals typically

exhibit broad, poorly resolved motional spectra that are difficult to unambiguously analyse [156]; the sensitivity of this method is quite limited for large crystals. Hence this technique is suitable only for small crystals with few different ionic species.

Another technique for establishing the identities of the trapped ions is crystal weighing [157]. This method is also based on the measurement of the secular motion frequency of ions via resonant-excitation. The technique involves the use of short voltage pulses (applied to the trap electrodes) to excite the motion of trapped ions and the analysis of the autocorrelation of the LIF for scanning the motional frequency spectrum. The main drawback of crystal weighing is that it is limited to the investigation of small crystals for which the product masses are already known. Moreover, this method is challenging to employ for time-resolved studies (crucial for establishing reaction rates) since it relies on sequential frequency scans, thus lacking the ability to ascertain the identities of all ions present at a precise time.

Highly-sensitive detection of the mass components of Coulomb crystals can be achieved by adopting time-of-flight mass-spectrometry (TOF-MS), whereby the quantitative identification of the masses occurs via Wiley-McLaren TOF-MS [158].During the last decades, TOF-MS has proved to be an effective and versatile technique in chemical analysis. It was initially proposed by Stephens [159] and later improved by Wiley and McLaren [158]. TOF-MS allows one to determine the masses and abundances of ionic species in a given sample featuring initial low kinetic energies and narrow spatial distribution. It is based on the principle that the velocities of the ions — accelerated by a constant homogeneous electric field — are related to their mass-to-charge ratios. Since the kinetic energy of the ions is approximately the same and the length of the flight tube is fixed, it is possible to separate masses based on the different arrival times to the detector.

When implementing TOF-MS using a Paul trap setup, the RF trapping field is switched off and two different DC voltages are applied to the two vertical pairs of

rods, thus acting as a repeller-extractor pair, with ions radially ejected into a free-flight tube and ultimately hitting a detector.

TOF-MS detection constitutes a destructive method: at every ejection event to interrogate the crystal composition, the sample is lost. Hence, numerous repeats of crystal loading, reaction and ejection events are required to examine the reaction kinetics.

Hudson *et al.* introduced a complex Coulomb crystal ejection setup where the RF fields are switched off within one RF cycle and high DC voltages ($V_{repeller}$ =1.4 kV and $V_{extractor}$ =1.2 kV) are applied to eject the ions towards a channel electron multiplier after travelling through two einzel lenses and a TOF tube [160]. Our group has proposed a TOF-MS approach employing a digital ion trap (DIT), where the trapping fields are square-like wavefunctions rather than conventional cosine RF waves [56]. The use of a DIT enables one to cleanly apply ejection voltages with no residual noise driven by the decaying RF fields. However, due to the technical limitations of the electronic devices available in our lab, the experimentally available trapping fields yielded a shallower trap ($\approx$ 1.21 eV) than the one achieved with conventional cosine trapping waveforms ($\approx$ 1.36 eV). This issue constituted a major constraint in terms of the range of reactions that could be studied. It meant that the DIT could not be utilised to examine a larger number of exothermic reactions (owing to the shallower trap depth).

The following section describes a new TOF-MS detection method, the damped cosine trap (DCT) TOF-MS approach, which has been characterised and employed for studying cold ion-molecule reactions as part of the work for this thesis.

4.2 Damped cosine trap ejection setup

The DCT TOF-MS detection apparatus comprises an ion trap, previously described in section 2.1.1, a grounded flight tube, and a multichannel plate (MCP) detector (see

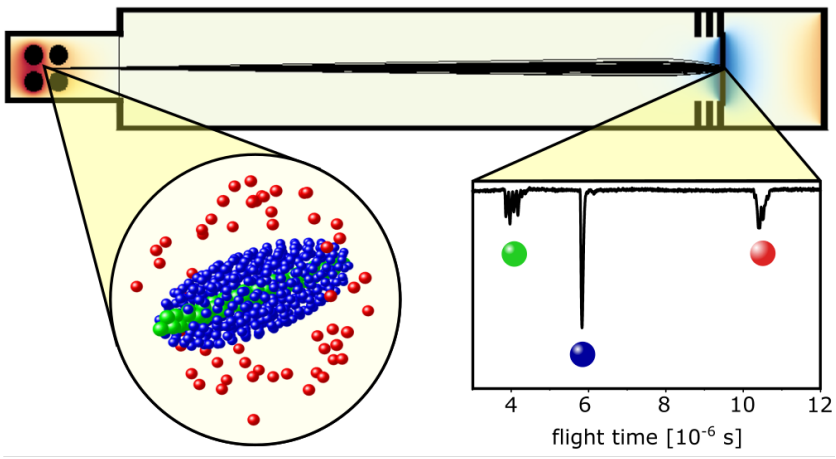

Figure 4.1: Pictorial view of the TOF-MS detection process. Coulomb crystals are formed within the ion trap and subsequently ejected through a field-free flight tube and onto MCP for detection. Different ionic species arrive at the detector at different times, depending on their mass-to-charge ratios, as indicated by the false-coloured spheres in the figure; the lightest green species are found in the centre of the Coulomb crystal and arrive at the detector first. Figure reproduced from [151].

figure 4.2). The ion trap sits 40.5 mm away from the flight tube entrance. Two ∼90% transparent grounded nickel meshes are located at the beginning and at the end of the TOF tube, to shield the free-flight region from electric fields propagating from the trap and the MCP.

The amplified MCP signal (collected from an anode held at +350 V) is proportional to the number of ions hitting the detector plate; for singly-charged ions, the integrated peaks within a TOF trace reflect the relative quantities of each mass channel present in a crystal prior to ejection.

When switching off the Paul trap RF fields, there is a residual RF voltage that remains superimposed on the ejection pulses; this is usually described as *ringing*. This has the negative effect of deflecting the ions away from the intended trajectory towards the detector thus negatively affecting the detection efficiency (see subsection 4.3.1).

The DCT TOF-MS relies on the damping of the trapping fields prior to the appli-

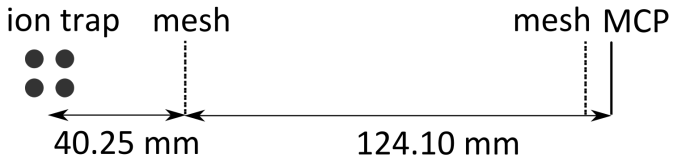

Figure 4.2: Schematic drawing of the side view of the adopted DCT detection apparatus composed of a linear Paul trap, a grounded flight tube and an MCP detector. The flight tube is grounded due to the presence of two nickel meshes held at 0 V. The mesh on the left acts as the third electrode for the second acceleration region of the Wiley-McLaren TOF-MS. Figure adapted from [151].

cation of the ejection pulse. Specifically, when the ejection button is fired to eject the ions from the trap and record a TOF trace, the driving electronics set off a circuit to actively quench the $\pm V_{RF}$ trapping RF waveforms. After a $\sim 1.26\ \mu s$ delay, to allow the residual RF fields to completely decay, the DC dipolar voltages ($V_{repeller}$ =305 V and $V_{extractor}$ =176 V) are applied to eject the ions from the trap, towards the MCP detector (electrified at -1.9 kV).

Figure 4.3 illustrates the recorded experimental waveforms of the two opposite phases (red and black) of trapping fields applied to the ion trap. At time $t = 0\ \mu$s, the RF fields are switched off and the damping circuit is activated. The RF waveforms are damped and decay during the delay time. When the ejection pulses are applied, four independent waveforms are applied to the four trap rods: "repeller(+)", "repeller(−)", "extractor(+)" and "extractor(−)". It is worth noticing that the delay time preceding the ejection pulse must be taken into account in order to correctly calibrate the experimental arrival times and match the time axis with the simulated TOF traces.

4.2.1 Experimental DCT TOF traces

The charge exchange process between Xe^+ and ND_3 (for which the calcium ions forming the initial Coulomb crystal act as a spectator and as a coolant for sympathetic cooling)

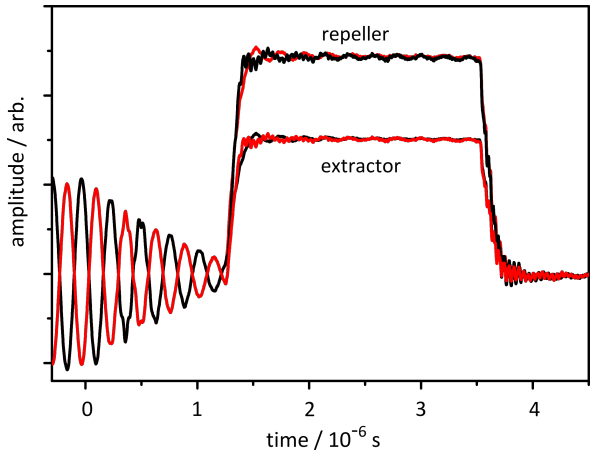

Figure 4.3: Plot of the experimental wavefunctions applied to the four ion trap electrodes. The cosine RF trapping fields are switched off at 0 μs; the damping lasts for $\sim$1.26 μs and then the ejection pulse starts. Figure reproduced from [151].

is chosen as a proof-of-concept reaction to test the performance of the DCT TOF-MS (chapter 6 discusses this charge exchange reaction system in more detail). Briefly, xenon ions are formed within the trap via (2+1) REMPI. Given their high mass, the Xe^+ ions experience a weak confinement and form an outer shell around the lighter Ca^+ ions. The Coulomb interaction between Xe^+ and the Ca^+ ions causes a flattening and elongation of the ellipsoidal shape of the Ca^+ lattice positions, and hence a change in the LIF pattern. This is clearly visible in figure 4.4 (b). After the formation of a stable Ca^+/Xe^+ bi-component Coulomb crystal, the charge exchange reaction is deemed to start when neutral ammonia molecules are admitted to the trap region. Specifically, in the preliminary measurements presented in this chapter, a mixture of ammonia isotopologues is introduced into the reaction chamber.

Each TOF trace is accompanied by a series of CCD camera experimental images of the LIF pattern recorded at various reaction times prior to ejection. One can eject a Ca^+/Xe^+ bi-component Coulomb crystal for TOF analysis before admitting ammonia, to ensure that the xenon ions are the only reactants and that the crystal contains no impurities. For instance, figure 4.5 shows an experimental TOF trace recorded for a

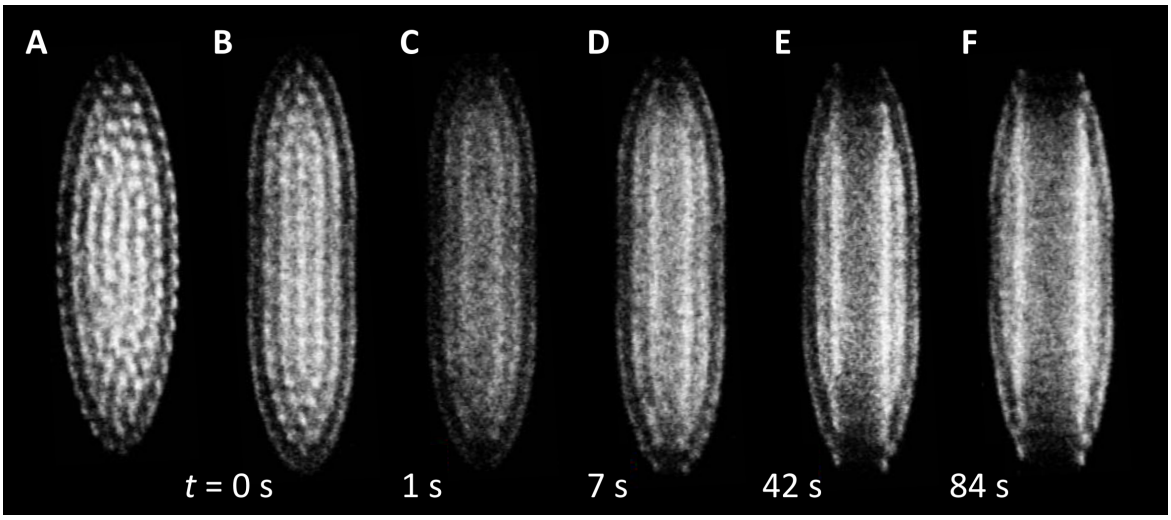

Figure 4.4: Series of images depicting the variation of the LIF profile during the charge exchange reaction between sympathetically cooled Xe^+ and ammonia. It is evident that a "dark" inner core of non-fluorescing ammonia ions grows as the charge exchange reaction progresses. Figure reproduced from [151].

Ca^+/Xe^+ crystal. The peak at 5.84 μs corresponds to the laser-cooled $^{40}Ca^+$ ions, whereas the xenon ions are represented by the broad peak centred at about 10.5 μs.

There are various factors contributing to the width of the Xe^+ peak in the TOF traces recorded. First, the xenon gas utilised in the experiment contains a mixture of isotopes with the natural isotopic abundance[1] and the REMPI laser light is insufficiently narrow in bandwidth to ionise only a specific isotope. As such, there are several mass channels that contribute to the broad Xe^+ peak. The xenon ions are also weakly confined to the trap axis and are not as effectively sympathetically cooled as co-trapped species with a mass-to-charge ratio closer to that of $^{40}Ca^+$, meaning that their kinetic energy is somewhat higher than that of $^{40}Ca^+$ ions (the effective temperature of the Xe^+ ions is approximately 10–20 K, which is 1-2 orders of magnitude higher than the effective temperature and kinetic energy of the Ca^+ ions). The repeller and extractor voltages adopted experimentally are also not optimised for such high

[1]The natural isotopic abundance of the xenon isotopes comprises ^{128}Xe (natural abundance of 1.92%), ^{129}Xe (26.44%), ^{130}Xe (4.08%), ^{131}Xe (21.18%), ^{132}Xe (26.89%), ^{134}Xe (10.44%) and ^{136}Xe (8.87%).

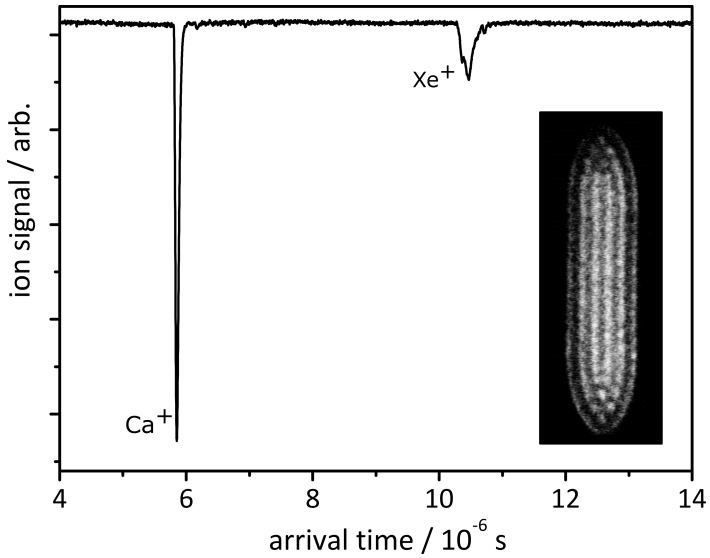

Figure 4.5: Ca^+/Xe^+ bi-component crystal TOF trace. The TOF mass spectrum shows that the Xe^+ reactant ions are cleanly incorporated into the crystal and no background impurities are present. Figure reproduced from [151].

masses. These factors contribute to the much broader Xe^+ TOF peak than is seen for the $^{40}Ca^+$ ions, hence the contributions of the various isotopes of Xe^+ are not resolved.

Conversely, the various ammonia ion isotopologues are fully resolved under the experimental conditions of the DCT TOF-MS, suggesting a mass resolution of $\lesssim 1$ u in the range of interest. Figure 4.6 shows the TOF trace recorded midway through the charge exchange reaction Xe^+ + ammonia. The four main peaks centred at around 4.1 μs indicate the presence of four isotopologues of the ammonia cation: NH_3^+, NH_2D^+, NHD_2^+, and ND_3^+. In addition to the $17-20$ u mass peaks, two side peaks can be seen at masses 21 and 22 u. Interestingly, these minor peaks reveal the presence of a few ammonium ions, formed by secondary reactions involving H- or D-addition from neutral ammonia molecules reacting with trapped ammonia ions (that have already been incorporated into the Coulomb crystal). For example $ND_3 + ND_3^+ \rightarrow ND_2 + ND_4^+$ gives rise to the mass 22 u peak. It must be stressed that the presence of ions at masses $17 - 22$ u could not be established from the crystal images alone, as all of

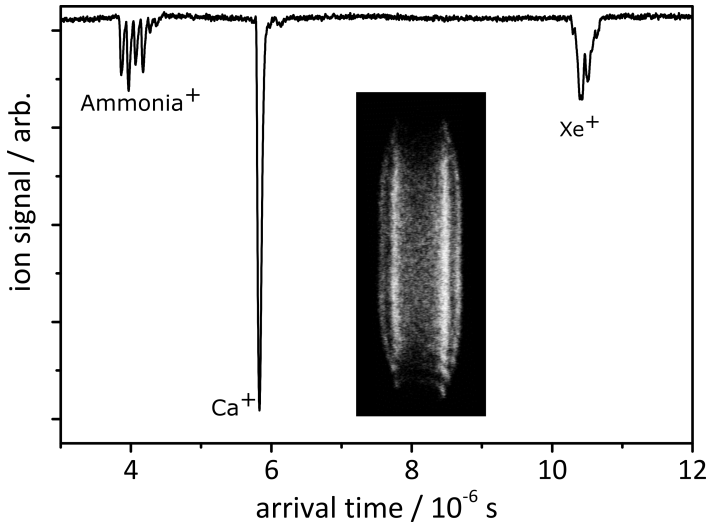

Figure 4.6: TOF trace recorded following the ejection of a multi-component crystal while the reaction between Xe^+ and ammonia is in progress. The peaks centred at ~4.1 μs indicate the presence of four isotopologues of ammonia: NH_3^+, NH_2D^+, NHD_2^+, and ND_3^+, with minor contributions from ammonium ions (NH_4^+, NH_3D^+, NH_2D^+, NHD_3^+, and ND_4^+) also evident. The $^{40}Ca^+$ peak is observed at 5.85 μs, with a shoulder peak at 6.17 μs corresponding to a small number of $^{44}Ca^+$ ions. The peak at 10.5 μs corresponds to the unreacted Xe^+ ions. The inset shows the LIF image of the crystal immediately prior to ejection. Figure reproduced from [151].

these ions are found in the dark inner core.

4.3 Ejection and detection simulations

In order to characterise the DCT TOF-MS setup, the trajectories of the ions ejected from the trap are simulated using a custom-made simulation program (called `fly.py`[2]). The code is written in Python programming language [161] and it employs the velocity Verlet algorithm to numerically integrate Newton's equations of motion [130, 162].

Prior to simulating the trajectories of the ions of a certain Coulomb crystal, the software package `SIMION` [163] is used to emulate the geometry and voltage configuration of the setup. This step allows one to numerically solve the Laplace equation and

[2]GitHub repository url: https://github.com/softleygroup/iflyer

thereby obtain the external fields that the ions experience throughout the ejection process. After importing the configuration files from `SIMION`, `fly.py` reads the positions and velocities of the ions within the Coulomb crystal from the output of `ccmd` (the Coulomb crystal molecular dynamics simulation code discussed in subsection 2.2.4). In order to accurately mimic the ejection process, the experimental waveforms (see figure 4.3) are imported and adopted into the simulation code. At each time step the algorithm calculates the forces (and thereby the acceleration) exerted on each ion, considering both the ion-field and ion-ion interactions. The ions velocities and positions are updated at each iteration of the velocity-Verlet algorithm, thus providing the trajectories of the ejected ions. When all the ions have hit either the detector or another surface of the setup, the algorithm stops and yields the information of when and where each ion landed.

4.3.1 Detection limitations

To scrutinise the effect of ejection from the ion trap without damping the resonant trapping fields prior to ejection, experimental waveforms recorded with the non-damped decaying RF superimposed on the extraction pulses have been imported into the simulation code. The ejection simulations demonstrate that ringing noise on the non-damped ejection pulses has a considerable impact on the trajectories of the ions, hindering the detection efficiency. Ions are deflected away when they experience an additional field component (arising from the ringing voltage) that is not parallel to the ejection axis. Additionally, the polarity and amplitude of any ringing noise depends on the phase of the RF at which the ions are ejected (see figure 4.7).

Consistently ejecting the ions at the same RF phase — for which there is maximum detection efficiency — might seem a viable solution to the problem. However, in addition to the technical difficulties arising from implementing a phase-synchronized

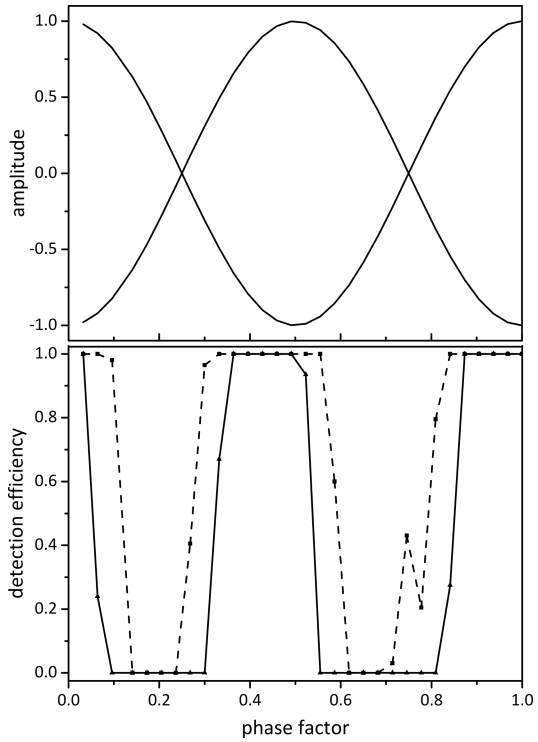

Figure 4.7: The number of ions successfully detected when using non-damped RF voltages prior to ejection is dependent on the phase of the RF when the ejection pulses are applied. The upper graph shows the amplitude of the RF voltages, where a phase factor of 1 is equal to 2π in radians. The lower graph shows the detection efficiency for a series of simulated 200-ion Ca^+ Coulomb crystals (with $\Omega_{\mathrm{rf}} = 2\pi \times 3.81$ MHz, $V_{\mathrm{rf}} =$ 147 V and $U_{\mathrm{dc}} = 2.7$ V) ejected at 30 different phases in the RF cycle. Simulations are conducted using different ejection voltages: 305 V and 176 V (dashed line), and 220 V and 97 V (solid line). It is evident that the number of ions reaching the detector is dependent on both the phase of the RF waveform upon ejection and the magnitude of the ejection voltages. Figure reproduced from [151].

ejection mechanism, it should be noted that the correlation between detection efficiency and RF phase also depends on the ionic species. When considering the ejection of multicomponent crystals, heavier masses will spend more time in the acceleration region; different ionic species will experience different phases of the decaying RF fields.

In contrast, simulations performed using the DCT waveforms demonstrated that more than 99% of the ejected ions successfully reach the detector plate. There is no dependence on the phase of the RF waveform prior to ejection. However, it must be

noted that there are a few experimental details not considered in the simulation that might reduce such near-unity efficiency. For instance, the two grounded meshes present in the detection setup (see figure 4.2) are simply modelled as grounded planes with 100% transparency in the simulations. As such, post-simulation detection efficiency corrections are performed adopting the optical transmission efficiency of $\approx 90\%$ for each mesh.

4.3.2 Consideration of mass resolving power

Simulations indicated that the DCT TOF-MS features a mass resolving power — defined as $m/\Delta m$ — of ≈ 100 for smaller (less than 100 ions) Coulomb crystals, decreasing down to $m/\Delta m \approx 70$ for larger crystals containing up to 200 ions [151]. The impact of the electrode geometry on the mass resolving power is scrutinised via comparing simulation results using conventional flat electrodes instead of the cylindrical rods constituting the linear Paul trap. Figure 4.8 illustrates how inhomogeneous the electric potential profiles generated by the DCT electrodes are in both the x- and y-coordinates (with the DCT trap axis oriented along the z-coordinate). This contributes to a spread in the kinetic energy imparted to ions of the same mass in the acceleration stages, thus affecting the mass resolving power of the DCT TOF-MS setup. Simulations indicated that by employing cylindrical electrodes one can achieve only $50 \pm 5\%$ of the mass resolving power obtained when simply substituting the rods with conventional planar electrodes as used in normal time-of-flight spectrometers (without ion trap). It is worth noting that a potential solution to this problem is the adoption of corrective or focusing elements. For instance, Bethlem and co-workers managed to compensate the non-planar electrode voltage profile distortions by including a series of planar electrodes featuring horizontal and vertical slits [164].

As pointed out in the previous section, the experimental ejection pulses feature

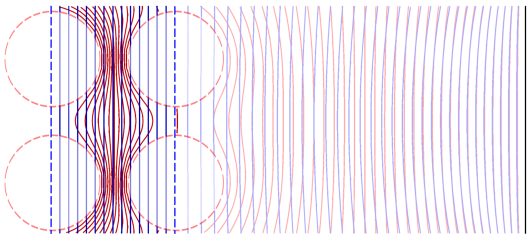

Figure 4.8: Schematic side view ($x - y$ plane) of the electric potential contour lines (drawn every 2.5 V) of the DCT TOF-MS acceleration stages (in red) compared with conventional planar electrode contour lines (in blue). The field inhomogeneity is more pronounced in the area near the cylindrical surfaces, especially in the first acceleration stage. These field distortions translate into a mass resolving power a factor of two lower than when adopting flat electrodes. Figure reproduced from [151] (Supporting Information document at DOI: 10.1021/acs.jpca.5b07919).

minimal residual ringing. By adopting fictitious experimental waveforms featuring no ringing noise, it is possible to simulate and quantify the effect of the residual ringing on the mass resolving power of the DCT. Simulations reveal that if there was no ringing noise superimposed on the ejection voltages, the mass resolving power could be enhanced by $20 \pm 2\%$. Technical improvements must be sought in order to cancel (or further minimise) the residual noise of the damped trapping waveforms at the time of ejection.

As noted above, there is a 1.26 μs delay between the turning off of the trapping waveforms and the application of the ejection pulses, to allow the RF fields to decay whilst being actively quenched. During this delay time, there is an expansion of the Coulomb crystal due to the increase of the ion-ion separations arising from the Coulomb repulsion. Simulations indicate that such delay yields a $6 \pm 3\%$ decrease in mass resolving power, a minor impact when compared to the ringing noise effect. Hence, the length of decay time between turning the trapping fields off and applying the ejection pulses could potentially be modified to maximise the detection efficiency, balancing the expansion of the crystal (when no confining forces are present) and the reduction in ringing noise (when there is more time for damping of the RF fields before

the ejection fields are applied).

Ejection simulations are also performed to examine the influence of the extraction voltages on the resolution of time of flight trace peaks in a certain mass region of interest. In a Wiley-McLaren mass spectrometer, repeller and extractor voltages are applied until all the species have exited the acceleration stages, so that ions arrive in the free-flight tube with approximately the same kinetic energy. There are, nonetheless, small variations in kinetic energy acquired by ions of the same mass due to the initial differences of the location of the ions. The spread in gained kinetic energy is further enhanced by the inhomogeneity of the ejection fields caused by the non-planar electrodes. The static extraction voltages can be optimised to compensate for the peak shape distortion due to the initial spatial differences of the ions. Simulations to improve peak separation and peak shape are conducted for tri-component crystals containing Ca^+ and sympathetically cooled $CaOH^+$ and $CaOD^+$ ions, exploring different extraction voltages whilst keeping the repeller voltage constant at 300 V. Figure 4.9 illustrates how the choice of $V_{extr} = 250$ V allows one to fully resolve the masses in the region of interest.

4.4 Summary

While the damped cosine trap ejection TOF-MS constitutes a destructive technique, it enables all species within the crystal to be quantitatively identified. It therefore affords a detailed investigation into complex reactions (such as $NH_3 + ND_3^+$ or the astro-chemically important $NH_3 + C_2H_2^+$) in a cold and controlled environment – studies that would not be possible with imaging detection methods alone. The high number- and time-sensitivity offered by this method and its broad applicability make it favourable over existing techniques such as resonant-excitation mass spectrometry and crystal weighing.

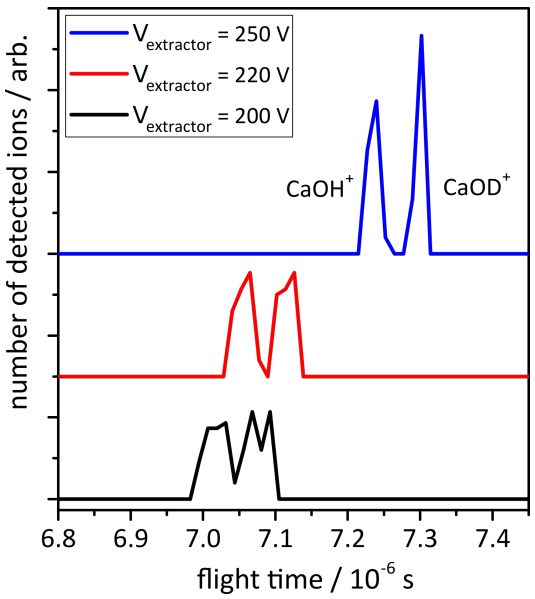

Figure 4.9: Simulated TOF spectra recorded for multi-component crystals containing 100 Ca^+, 50 $CaOH^+$ and 50 $CaOD^+$ ions. The data is obtained with the repeller voltage at 300 V; the extractor voltages range from $200 - 250$ V. The split in the $CaOD^+$ peak with repeller and extractor voltages of 300 V and 200 V (respectively), as seen in the lowest (black) trace, arises from the excess acceleration imparted to ions closer to the repeller. When choosing an extractor voltage of 250 V, it is possible to resolve the peaks corresponding two isotopologues (blue trace). Figure reproduced from [151].

Considering the deeper trap depth offered by the DCT (which facilitates the study of a broader range of exothermic reactions), the DCT TOF-MS constitutes a better alternative to the DIT TOF-MS setup [151]. Earlier in the chapter, it has been mentioned that the Hudson group adopted a Coulomb crystal detection method similar to the DCT TOF-MS [160]. Owing to complex electronic devices, their scheme utilises sinusoidal trapping voltages that are switched off within a fraction of an RF cycle prior to applying the ejection pulses. The used setup achieves isotopic mass resolution and a mass resolving power of ≈ 500. However, saturation of the ion detector — a channel electron multiplier (CEM) rather than MCPs — resulted in lower detection efficiency ($\approx 50\%$). The Willitsch group have also adopted a Paul trap TOF-MS approach [165]. However, in their device the ejection pulses are applied by extra separate repeller/extrator plates located very close to the Paul trap electrodes. While this configuration conveniently addresses the ringing issue, the presence of these extra electrodes (in proximity to the ion trap) creates detrimental stray fields. It is noted that recently Lewandowski and co-workers have adopted - and improved upon - our approach, achieving a mass resolving power ≥ 1100 over a wide mass range [166].

Further improvements to the DCT TOF-MS detection setup would involve more effective damping of the trapping waveforms, to reduce the minimal ringing noise and thus improve the mass resolving power, and the introduction of ion focusing elements to improve the detection efficiency. Moreover, it is noted that the adoption of the reflectron principle could enhance the mass resolution by several orders of magnitude [167]. With this approach, a reversing field is added after the free-flight region. As a result, ions with a greater kinetic energy can penetrate further into the reversing field, thereby taking longer to turn around. Consequently, all ions of a given mass can converge in time at the detector. Lastly, it is worth noting that the inclusion of corrective ion lenses, a phosphor screen and a CCD camera would allow one to visualise the spatial distribution of an ejected crystal, thus complementing the crystal

morphology analysis achievable via molecular dynamics simulations [151].

The DCT TOF-MS represents a powerful tool for the accurate detection of species in Coulomb crystals for studying cold reactions. As discussed in chapter 1, the development of effective quantitative detection methods for investigation of low temperature reactions is a prevailing goal of our research. The other key objective is the achievement of full control over all the reaction parameters. In this regard, the following chapter is devoted to describing the significant progress towards obtaining control of the orientation of cold polar molecule reactants coming from the buffer gas cell and electrostatic guide apparatus.

Chapter 5

Controlling the orientation of the guided cold molecular beam

This chapter is concerned with the analysis of the extent to which the spatial orientation of internally and translationally cold ammonia molecules can be controlled as they pass out of the quadrupole guide and through different electric field regions. The work presented in this chapter has been published as an article in the Journal of Molecular Spectroscopy [168]. My role in this project was principally in setting up and recording the measured REMPI spectra of the molecules exiting the guide for different laser polarisations. The theoretical simulations of the time-dependent evolution of the alignment were mainly carried out by E. Steer and the results of the simulations are included here for comparison with the experimental measurements and for completion.

5.1 Orientation of molecules

The ultimate objective in the field of reaction dynamics is the ability to develop a complete understanding of the reaction process. Throughout this thesis, it has been frequently mentioned how the investigation of chemical reactions under cold conditions

can afford control over the interaction energy and the quantum state population distributions of the reactants. At low temperatures, the long-range intermolecular forces experienced by slow-moving molecules can affect the orientation of the colliding partners as they approach. The orientation of the reactants can play a significant role in the properties of the resulting products [169, 170, 171, 172] . As such, gaining control over the spatial orientation of molecules is crucial in the study of reactive collisions.

In this regard, remarkable results were obtained in the 1970s by Brooks, who conducted beam scattering experiments using a hexapole and a static field to state-select and orient molecules. He demonstrated how the reaction rate coefficient for the $CH_3I + K \rightarrow KI + CH_3$ process was strongly influenced by the way the methyl group was oriented [173]. More recently, de Miranda *et al.* investigated orientation effects under ultracold conditions with KRb molecules held in an optical lattice trap. Their study showed how the rate coefficient for the $KRb + KRb \rightarrow K_2 + Rb_2$ reaction was significantly reduced (compared to the rate recorded with no orientation of the reactants) when the dipoles of the KRb molecules were aligned, such that only unfavourable "side-by-side" collisions could occur [174]. It is also worth noting that, when examining beams of $O(^3P_2)$, $Ne(^3P_2)$ and $He(^3S_1)$ emerging from a bent magnetic guide, Osterwalder and collaborators detected a substantial degree of orientation to the quantisation axis – in spite of the absence of additional uniform magnetic fields after the guide [175]. They have suggested that weak fringe fields emanating from the guide and stray magnetic fields could explain the results.

Electric (and magnetic) fields serve to shift and split the energy levels of polar (radical) molecules (see Stark and Zeeman effect in subsection 1.2.1), in addition to orienting the electric (magnetic) dipole moment of the species. The orientation of dipoles can be explained either in a classical or a quantum mechanical theoretical framework. From a classical mechanics perspective, molecules tend to assume the lowest energy configuration, which corresponds to the dipole moment being oriented

parallel to the applied electric field. This is the most stable configuration, although the amount of rotational kinetic energy may be enough to overcome the orientational potential. From a quantum mechanical point of view, the change in the rotational wave function induced by the field encodes the amount of orientation of the dipole [176].

5.1.1 Orientation of ammonia molecules

From the Stark Hamiltonian term (see equation 3.1), the interaction energy between any symmetric top molecule (*e.g.*, ND_3 or NH_3) and an external electric field E, can be calculated as $U_{\text{Stark}} = -\mu E \langle cos\theta \rangle$, where θ is the angle between the electric dipole $\vec{\mu}$ and the field axis. As previously mentioned in section 3.1, the expectation value of $cos\theta$ can be expressed in terms of the total angular momentum quantum number J and its projections K and M on the molecular principal axis and on the external field axis, respectively [177]:

$$\langle cos\theta \rangle = \frac{KM}{J(J+1)} \tag{5.1}$$

Therefore, the orientation effects are molecule and state dependent. Specifically, the electric field strength required to orient a molecule, in a given $|J, K, M\rangle$ state, to the external field axis can be expressed as [178]:

$$E_{JKM} = \frac{W_{\text{orient}}}{\mu} \frac{J(J+1)}{KM} \tag{5.2}$$

where W_{orient} is the minimum threshold energy required to rotate the molecule and depends upon the moment of inertia of a given molecule. For most small symmetric top molecules in low lying J states (typically $J < 7$), E_{JKM} is on the order of a few V cm^{-1}. Consequently, the magnitude of the electric field in the quadrupole guide — which near the axis varies linearly with distance from the axis and is approximately

independent of azimuthal angle — is more than sufficient to influence the orientation of ammonia molecules (except very close to the axis).

5.2 Experimental methods

The experiments described in this chapter have been conducted using the the buffer gas cell and quadrupole guide (described in section 3.3) before combining this cold molecule source with a linear Paul trap. Ammonia molecules, either NH_3 or ND_3, are internally and translationally cooled through collisions with He atoms (at a temperature of 6 K) in the buffer gas cell. Molecules in LFS states are then extracted via the electrostatic quadrupole guide operated at ± 5 kV. After exiting the guide, molecules (with a rotational temperature of ≈ 10 K) pass through a grounded nickel mesh (total area $\approx \pi \times 10^2$ mm^2) and then reach the detection region. The detection setup comprises a conventional (flat extraction electrodes) Wiley-McLaren TOF mass spectrometer, a free-flight tube and MCPs. The repeller and extractor plates have a 25 mm inner diameter and voltages of 300 V and 217 V are applied, respectively. The TOF tube (160 mm in length) is mounted to be aligned to the axis of the final section of the quadrupole guide (see figure 5.1).

When arriving at the region between the repeller and extractor plates, 14.85 mm beyond the guide exit, molecules are ionised and then accelerated towards the MCPs (held at -1.9 kV) for detection. Specifically, $(2 + 1)$ resonance-enhanced multi-photon ionisation (REMPI) spectroscopy (see subsection 5.2.1) has been employed with linearly polarised light in order to probe the alignment of cold ammonia molecules after they exit the quadrupole guide and enter a reaction chamber for detection.

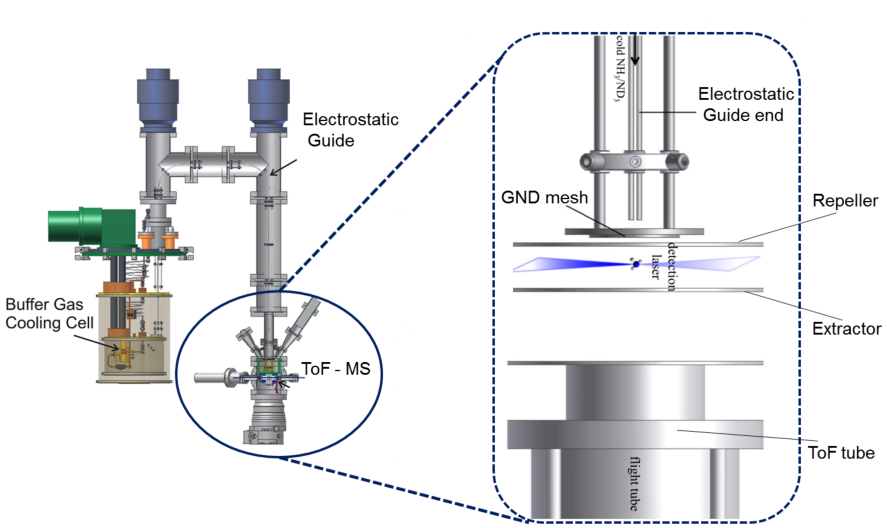

Figure 5.1: CAD drawing of the experimental apparatus used for investigating the alignment of buffer gas cooled and velocity selected ammonia molecules. The inset shows the main elements of the adopted Wiley-McLaren TOF mass spectrometer. Figure adapted from [137].

5.2.1 Resonant Enhanced Multiphoton ionisation

REMPI is a species- and quantum-state selective, highly sensitive spectroscopic technique. It relies on a multi-photon process that leads to the creation of an intermediate excited Rydberg state, which is subsequently excited to the ionisation continuum and detected. Specifically, in $(m + n)$ REMPI spectroscopy, m photons excite the molecule from an electronic ground state $|g\rangle$ to an intermediate excited electronic state $|e\rangle$; then, the absorption of n additional photons of the same energy ionises the molecule (see figure 5.2). A laser is typically scanned in wavelength in order to obtain different intermediate state resonances from different ground rotational states to the excited state. This process yields a REMPI spectrum, which provides information on the initial quantum state distribution of the probed molecules (via the spectral line intensities). As mentioned in chapter 3, REMPI spectra were recorded to ascertain the relative population of each rotational state when characterising the internal temperature of

the buffer-gas cooled and guided beam at the end of the guide.

Numerous spectroscopic studies have been conducted on NH_3 and ND_3. As a consequence, many spectroscopic constants and Rydberg states are well known, thus making these molecules ideal systems to probe for proof-of-concept studies. In the experiments described in this thesis, (2+1) REMPI spectra are then recorded by exciting the $\tilde{B}(v_2' = 5) \leftarrow \tilde{X}(v_2'' = 0)$ transition in ND_3 and NH_3. There are two reasons that led to the choice of this spectroscopic transition. First, the excited state $\tilde{B}$ has a lifetime of 0.25 ns (far longer than the 1 ps lifetime of the first excited state of ammonia) independent of the rotational state (for vibrational levels $v_2' \leq 6$), thus making this state ideal for extracting populations from rotationally-resolved REMPI studies. Secondly, the $\tilde{B}(v_2' = 5) \leftarrow \tilde{X}(v_2'' = 0)$ transition is proximate in energy to the peak output of the adopted laser system (*i.e.*, the frequency doubled output of a dye laser at ∼317 nm).

5.2.2 Probing alignment with polarised REMPI

By using a $\lambda/2$ plate and a polarising beam splitter, the polarisation of the REMPI laser can be controlled such that it is parallel or perpendicular to the TOF axis. Linearly polarised light facilitates the investigation of the M distribution and therefore the alignment of ammonia molecules at the point of detection. Linearly-polarised laser light allows different ΔM transitions to be probed independently: $\Delta M = 0, \pm 2$ transitions are excited by photons polarised perpendicular to the field (horizontal polarisation); only $\Delta M = 0$ transitions are excited by light polarised parallel to the field (vertical polarisation).

In figure 5.4 the recorded experimental polarised REMPI spectra are shown for ND_3 and NH_3 with the traces in black and red corresponding respectively to the parallel and perpendicular linearly polarised light cases. By comparing the recorded

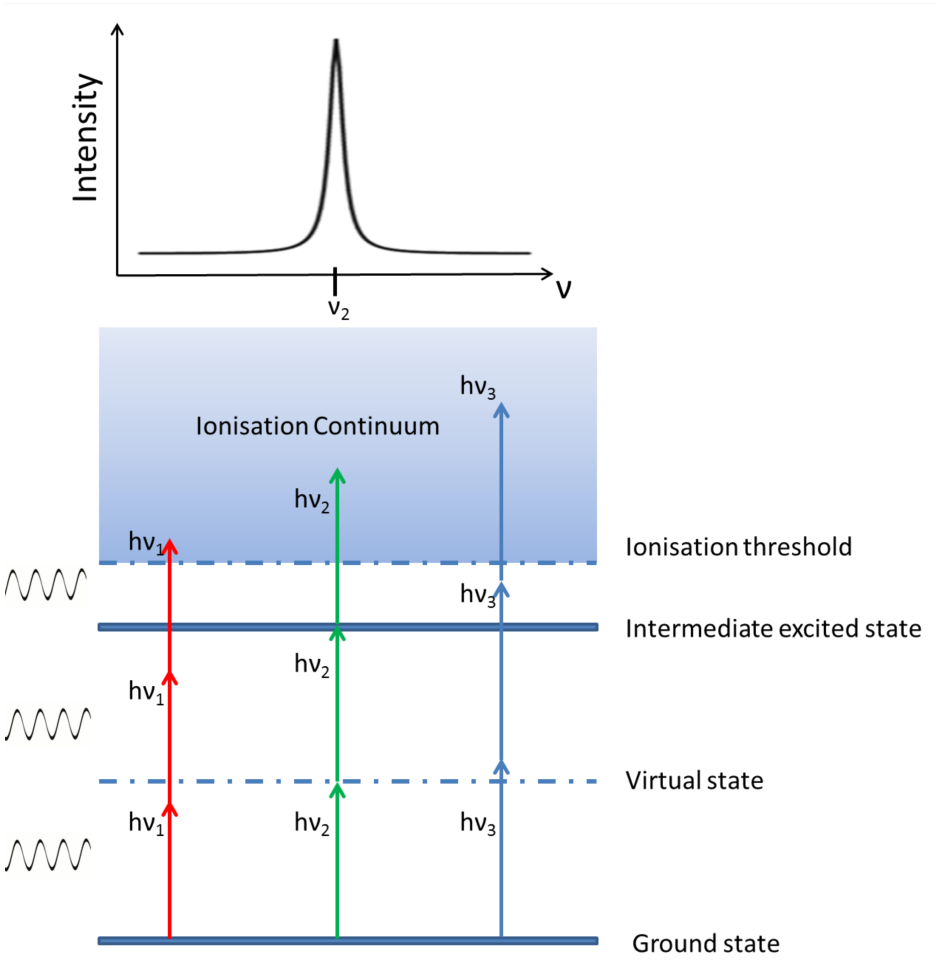

Figure 5.2: Pictorial view of the (2 + 1) REMPI process. When scanning the photon energy $h\nu$, enhancements in the ionisations signal are observed when the energy carried by the 2 photons is resonant with the transition to the intermediate excited electronic state $|e\rangle$.

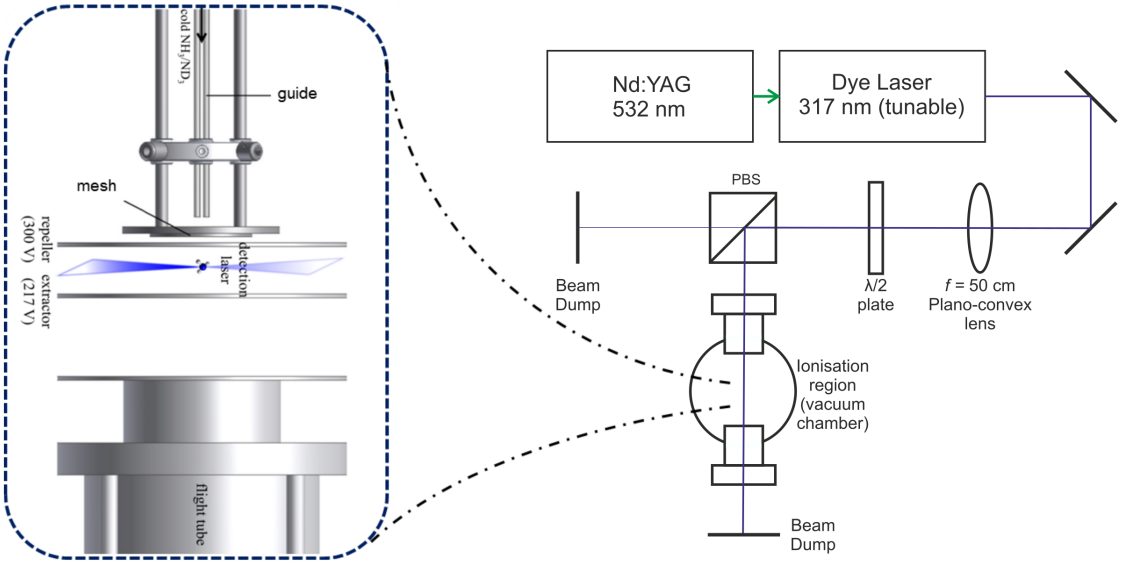

Figure 5.3: Optical setup for conducting polarisation-dependent REMPI measurements. A $\lambda/2$ plate and a polarising beam splitter are employed to change the polarisation of the REMPI laser. Figure adapted from [137].

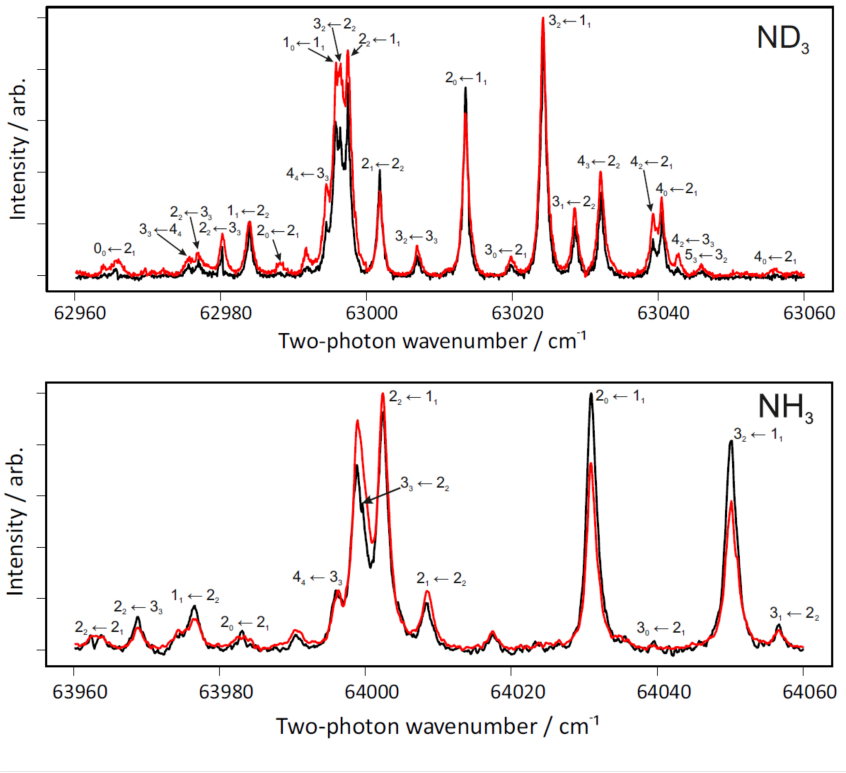

Figure 5.4: Experimental (2 + 1) REMPI spectra of both ND_3 and NH_3. The data in black is obtained via laser light linearly polarised parallel to the field axis, whereas the spectra in red are recorded using photons polarised orthogonally to the field. Figure reproduced from [168].

REMPI spectra obtained with the aforementioned light polarisations, differences in peak intensities are clearly visible. If there was no degree of spatial orientation of the molecules, no difference would be expected in the two REMPI spectra recorded with different laser polarisations. These significant differences in peak intensities are indeed due to the residual spatial orientation (relative to the local electric field axis) of the molecules at the point of spectroscopic probing.

For a more quantitative analysis, numerous repeat scans of the ND_3 REMPI spectrum were collected over the narrower spectral window $63008 - 63028$ cm^{-1} (two-photon energy), where clear peak intensity differences were observed (see figure 5.5). The preferential focus on examining ND_3 over NH_3 is due to the enhanced signal-to-

noise achievable resulting from the better transmission efficiency of ND_3 through the quadrupole guide (see [179]).

It should be noted that *orientation* and *alignment* have two clearly distinct meanings in spectroscopy. Essentially, if a molecule is aligned to a certain external electric (or magnetic) field axis, it means that its electric (or magnetic) dipole moment is positioned preferentially parallel or anti-parallel to that external axis with equal probability. If the orientation of the molecule is known, one can establish whether the molecule resides preferentially parallel or preferentially anti-parallel to the field direction. Effectively, in quantum mechanical terms, it means that in an aligned ensemble of molecules with angular momentum vectors $\vec{J}$, the values M of the projections of $\vec{J}$ on the reference axis can be either positive or negative. Specifically, states of a given magnitude $|M|$, have the same probability in the M-state distribution, irrespective of whether M is positive or negative. By contrast, if the sample is oriented to a certain axis, then there may be both positive and negative M components but these are of unequal probability.

By using REMPI with linearly polarised light, it is possible to probe the alignment of the molecules; the information about the orientation of the molecules can then be reconstructed via detailed simulations and fitting of the REMPI spectra. The protocol adopted for performing such simulations is explained in the following section.

5.3 Simulations

5.3.1 Simulating the REMPI spectra

Thanks to our collaborator Dr. Colin Western (University of Bristol), the `PGOPHER` spectral fitting and simulation software package has been improved and expanded (version 10) to produce simulated spectra under different polarisation configurations.

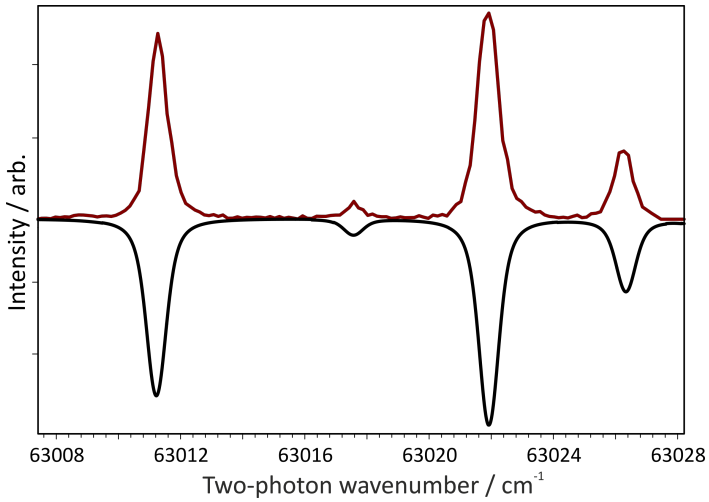

Figure 5.5: Comparison of the experimental (above) and (inverted) simulated (below) $(2+1)$ REMPI spectra of ND_3 recorded over the region $63008 - 63028$ cm^{-1} (two-photon energy) using laser light linearly polarised parallel to the local electric field. Figure reproduced from [168].

A detailed discussion of the theoretical premises adopted by Western can be found in reference [168].

The upgraded software enables one to determine the distribution over J, K and M. Specifically, a very small static electric field (1 V m^{-1}) — which has a negligible effect on its own on line positions or overall intensities — is assumed when performing the simulations so that the (otherwise degenerate) M component can be calculated separately. The population of each quantum level can be specified as a separate fitted parameter instead of using a default Boltzmann distribution.

A contour fit is performed for the spectra recorded over the narrower spectral window $63008 - 63028$ cm^{-1} (adopting the spectroscopic constants reported in [180, 181]), with the only fitting variables being the populations of states of given J, K and M. The fitting procedure returns robust populations, as illustrated by the excellent agreement between the experimental and simulated spectra in figure 5.5 (see 5.1 for the tabulated populations of the experimental spectra obtained via spectral fitting).

Table 5.1: Relative ND_3 rotational state populations established from `PGOPHER` fits to the experimental $(2 + 1)$ REMPI spectra recorded using linearly polarised light. Populations are normalised such that the population within each J_K state sums to 1. Statistical populations are provided for comparison. Table reproduced from [168].

$\|J, \|K\|, MK\rangle$	Perpendicular	Parallel	Statistical
$\|1, 1, -1\rangle$	0.22(15)	0.20(16)	0.33
$\|1, 1, 0\rangle$	0.38(8)	0.39(8)	0.33
$\|1, 1, 1\rangle$	0.40(13)	0.40(14)	0.33
$\|2, 1, -2\rangle$	0.28(11)	0.34(16)	0.20
$\|2, 1, -1\rangle$	0.21(8)	0.18(3)	0.20
$\|2, 1, 0\rangle$	0.12(11)	0.11(11)	0.20
$\|2, 1, 1\rangle$	0.13(10)	0.11(10)	0.20
$\|2, 1, 2\rangle$	0.26(8)	0.26(8)	0.20
$\|2, 2, -4\rangle$	0.26(3)	0.25(5)	0.20
$\|2, 2, -2\rangle$	0.21(8)	0.18(6)	0.20
$\|2, 2, 0\rangle$	0.17(8)	0.18(8)	0.20
$\|2, 2, 2\rangle$	0.14(7)	0.14(7)	0.20
$\|2, 2, 4\rangle$	0.22(4)	0.26(8)	0.20

5.3.2 Simulated trajectories

The reason why not all the internally and translationally cold ammonia molecules exhibit preferential orientation (to the field axis) at the point of spectroscopic probing is that, prior to reaching the detection region, the molecules travel through various electric field regions varying in both intensity and direction. For instance, in this apparatus, the quantisation axis is rapidly rotated from the inhomogeneous electric fields within the quadrupole to the homogeneous field — parallel to the TOF tube and the final section of the guide — present between the repeller and extractor plates.

Generally, polar molecules follow the field adiabatically and the eigenstates can be quantised with respect to the axis of the electric field. However, non-adiabatic transitions can occur, thereby leading to loss of orientation of the sample. One of the factors leading to non-adiabatic transitions is the rapid variation of the electric field direction so that molecules are not able to follow such field variation, thus losing their orientation to the field. Specifically, when the frequency at which an electric

field direction is rotated is comparable to or larger than the splitting between the neighbouring M states, non-adiabatic transitions can happen. In a quadrupole, the rate of rotation of the field is orders of magnitude slower than the minimum splitting between states, therefore there is no risk of such non-adiabatic transitions [182].

The other factor leading to non-adiabatic transitions is the presence of near-zero field regions. At zero field, the energy levels of a polar molecule are no longer split by the Stark effect. Therefore, when polar molecules travel through regions where the magnitude of the electric field is minimal, there is a near-degeneracy in states differing only in their orientation with respect to the electric field. As such, population in a certain oriented M state could transit into other nearly-degenerate states with the consequent loss of orientation. In the current setup, a critical region is around the entry to the grounded mesh, where the field rotates relatively rapidly whilst the magnitude of the field is also near-zero.

Monte Carlo trajectory simulations were carried out by E. Steer in order to investigate how the molecules maintain residual orientation (after exiting the guide and travelling through different electric field configurations and near-zero field regions), and to ascertain whether full orientation can be ultimately obtained through amendments to the current apparatus [137]. Specifically, the electric field framework experienced by the ammonia molecules as they pass through the electrostatic guide and into the ionisation region are modelled via the software package `SIMION` [163] (see figure 5.6). Voltages are applied to the quadrupole guide and the repeller and extractor plates throughout the simulations, in accordance with the experimental conditions. It should be emphasised that the nickel mesh (wire width 12.7 μm, pore area 0.042 mm^2, 88% transmittance) is modelled fully to account for any micro-focusing and fringe fields.

Within this emulated electric field framework, a script written in `MATLAB` [142] propagates ND_3 molecules with a pre-defined initial quantum state and velocity by solving and updating the time-dependent Schrödinger equation (TDSE). The adopted

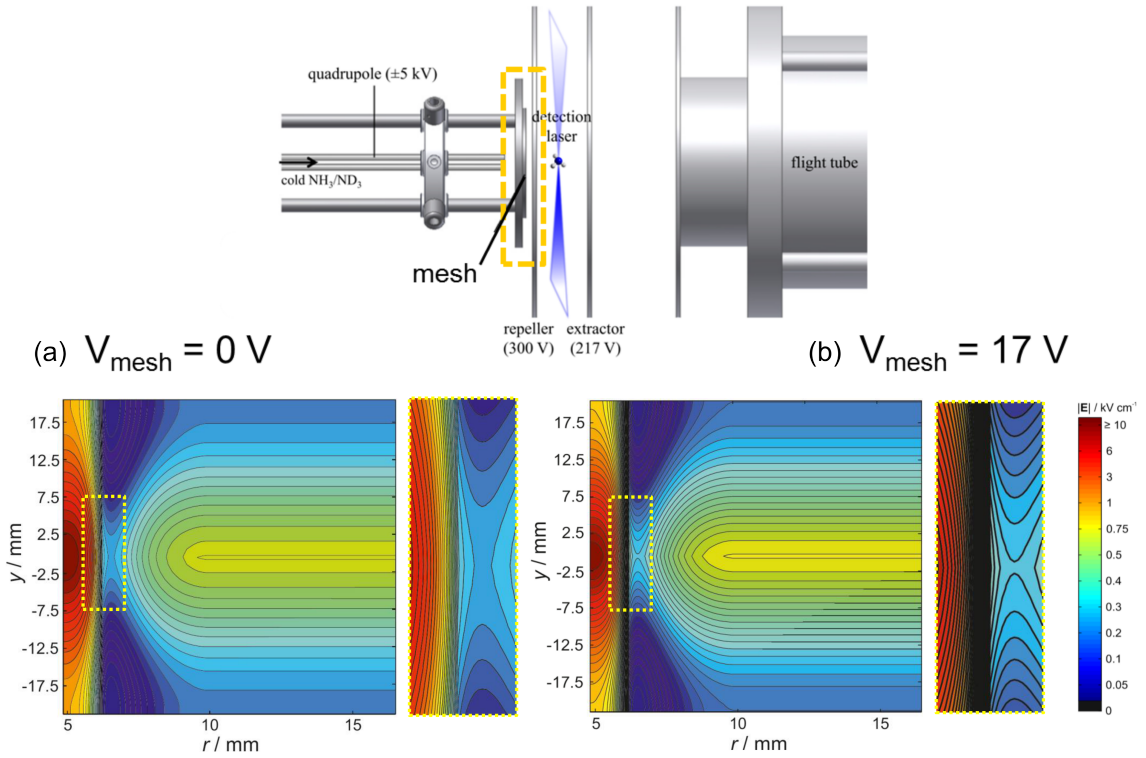

Figure 5.6: Comparative graph of a 2D slice of the simulated electric fields in the detection region after the guide in two cases, when the mesh is grounded (as in the current setup) and with a bias voltage of 17 V applied to it (corresponding to a field of 3 V/cm at the mesh). The quadrupole guide exit is at 0 mm, with the mesh located at 6.05 mm and the repeller plate at 8.00 mm. The regions enclosed within the dashed yellow lines are provided enlarged beside each plot, to better show the field framework differences. Figure reproduced from [168].

symmetric top basis set includes the inversion doubling and the hyperfine interactions. At 20 ns time steps, the evolution in time of the Stark Hamiltonian is calculated, thus allowing the M-state population (and thereby the orientation to the local field) evolution to be tracked. Notably, the TDSE is solved in a co-ordinate system that rotates following the direction of the field. This is a more efficient approach than considering performing calcualtions with a rotating field in a fixed frame of reference [182].

Figure 5.7 depicts the tracked orientation of a simulated 10^5 ensemble of ND_3 molecules in the $J_K = 1_1$, 2_1, and 2_2 states as a function of position (corresponding to different electric field regions). The top graph represents the $|J, MK\rangle$ populations in the local field frame, providing the orientation of molecules with respect to the local electric field. The bottom row illustrates the orientation of molecules with respect to a fixed laboratory axis, parallel to the final section of the guide and the TOF tube axis (namely, the z axis). As M is defined with respect to the local electric field, and not a space-fixed axis, the lower panel plots the M' distribution. (At distances beyond the repeller, $M' \equiv M$ as the electric field vector aligns with the z axis.)

5.4 Results and discussion

The aforementioned trajectory simulations confirmed that there is a rapid loss of polarisation as the internally and translationally cold ammonia molecules reach the detection region after exiting the guide. While the M-state distribution within the quadrupole guide is retained as molecules exit the guide, it is then almost entirely lost as molecules pass through the grounded mesh (located at 6.05 mm beyond the guide exit). The presence of some residual orientation after the mesh and at the point of spectroscopic probing (mainly for molecules in the $J_K = 2_2$ states, as shown in figure 5.7) confirms the clear differences consistently reproduced when comparing the various

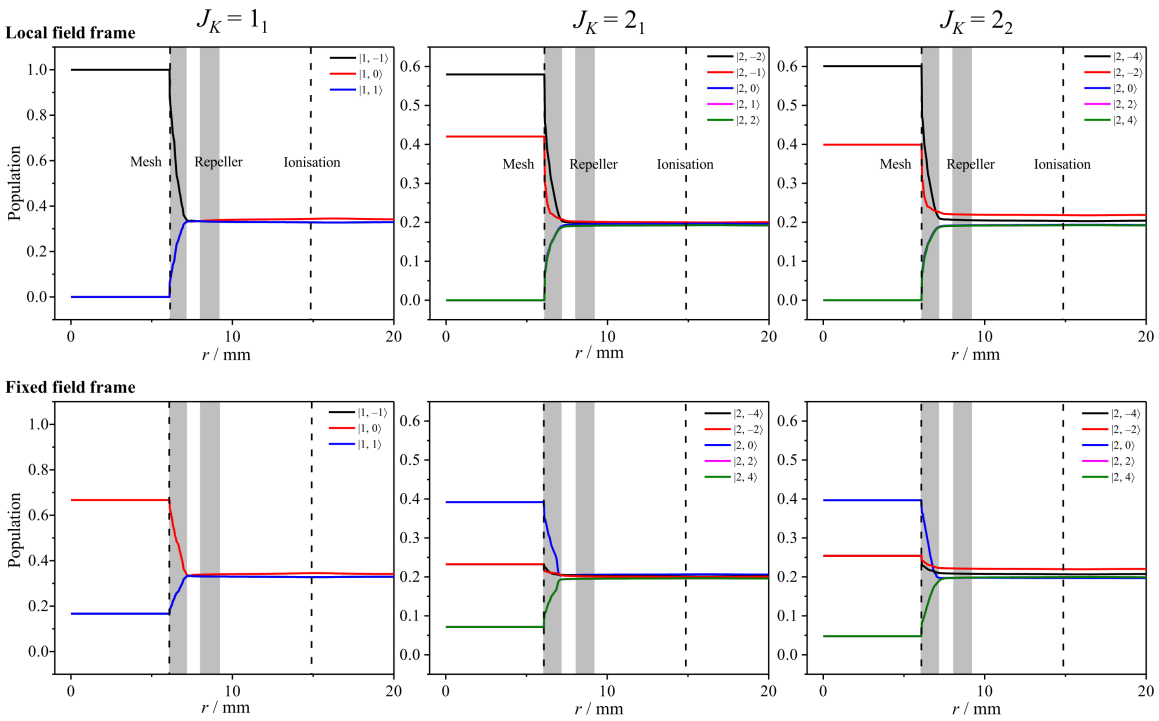

Figure 5.7: Change of orientation (MK-state notation) for ND_3 molecules in the $J_K = 1_1$, 2_1, and 2_2 states, plotted as a function of position and obtained from trajectory simulations. The top graph refers to the local field axis; the bottom graph refers to the fixed quantisation axis which corresponds to the axis of the final section of the electrostatic guide. The guide exit is located at 0 mm, the grounded mesh is positioned from 6.05 to 6.15 mm, with the mesh holder extending a further 1.0 mm. The repeller plate extends from 8.00 to 9.20 mm. ND_3 molecules are probed by the REMPI laser 14.85 mm beyond the guide exit. Figure reproduced from [168].

experimental REMPI spectra recorded with the two different configurations of linearly polarised light. As previously discussed, this loss of orientation is a consequence of the non-adiabatic transitions occurring due to the very rapid field rotation as the molecules enter the near-zero field region and subsequently due to the significant length (and time) over which molecules are held near-zero field.

Remarkable studies from Meijer and collaborators [141] showed that non-adiabatic transitions of polar molecules in an electrostatic trap can be suppressed when additional voltages are applied, such that the trap centre exhibits a non-zero field minimum. Moreover, previous studies on CH_3I have recorded orientation in molecules exiting a hexapole and entering a region of uniform electric field. Field intensities as low as 3 V cm^{-1} were sufficient to orient the examined molecules [177, 178]. Inspired by these findings, various simulated modified configurations of the current apparatus were explored with the view of suppressing the loss of orientation.

5.4.1 Maintaining the orientation

Adopting the same simulation protocol discussed in subsection 5.3.2, the effect of applying different voltages to the (previously grounded) mesh has been investigated to establish the minimum field needed to orient ammonia molecules at the point of spectroscopic probing. It is found that the application of a small voltage of 17 V (corresponding to a field of 3 V cm^{-1} at the mesh; see figure 5.6) allowed enhanced orientation of ND_3 to be preserved (see figure 5.8). With the application of a small voltage at the mesh (whilst replicating all the other experimentally applied voltages), the near-zero field region is removed. Therefore, the near-homogeneous fields beyond the mesh rotate the local field experienced by the molecules, from the inhomogeneous field in the quadrupole to the uniform direction of the field in the ionisation region. As such, molecules can follow the field adiabatically and retain their orientation as they

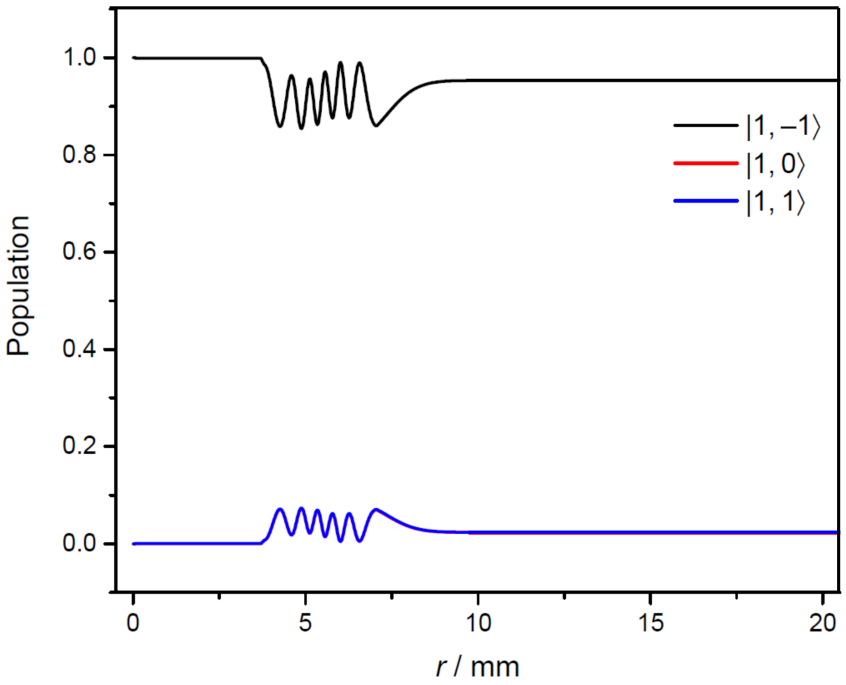

Figure 5.8: Simulated $|J, MK\rangle = |1, -1\rangle$ fraction of total population in $J_K = 1_1$ probed when a voltage of 17 V is applied at the mesh. The fraction of population is measured at different distances from the guide exit ($r = 0$ mm) as molecules travel through the different field regions of the apparatus. Figure reproduced from [168].

move through the different electric field regions until they reach the ionisation region.

From extensive trajectory simulations, it is ascertained that fields on the order of a few V cm^{-1} are sufficient to maintain more than 90% of population in the $|1, -1\rangle$ state. The simulations suggest that over 95% of population will be retained in the $|1, -1\rangle$ state when a 17 V bias voltage is applied to the mesh (see figure 5.9).

It is important to notice that, in the current experimental apparatus with the grounded mesh, molecules experience the problematic regions of near-zero electric field for a z-axis distance of up to 1.1 mm (see 5.6). This is due to the fact that, even though the mesh itself is very thin, with the Ni wire only 0.1 mm thick, the mesh holder has a width of 1.0 mm. Both the mesh and the mesh holder are held at ground during the experiments. As such, an alternative approach to reduce loss of orientation of molecules reaching the detection region is to reduce the length of this near-zero field

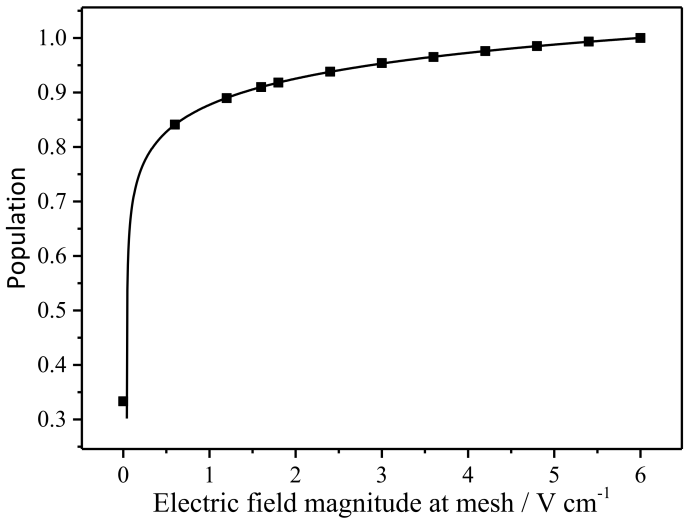

Figure 5.9: Simulated $|J, MK\rangle = |1, -1\rangle$ fraction of total population in $J_K = 1_1$ probed for different electric field strength values at the mesh. Figure reproduced from [168].

region. Essentially, replacing the mesh holder — currently made of stainless steel — with an insulating material would significantly reduce the near-zero field region along the z axis (from 1.1 mm down to 0.1 mm). Hence, molecules would experience a near-zero field for less time, thereby decreasing the likelihood of non-adiabatic transitions occurring. Trajectory simulations indicated that 70% of ammonia molecules would retain the orientation at the detection region if the mesh holder was made of an insulating material (see figure 5.10).

Since an ion trap has been installed in place of the detection region, a consideration has to be made with regard to the effect of the trapping fields on the oriented internally and translationally cold polar molecules reaching the target of cold ions. In order to preserve the orientation of molecules as they reach a prepared Coulomb crystal target (for the study of orientation-dependent cold reactive collisions), it is crucial to prevent the Paul trap RF fields from inducing non-adiabatic transitions.

Employing digital trapping fields (as in the DIT setup previously developed in the group [56]) rather than conventional cosine RF waves could provide a solution to

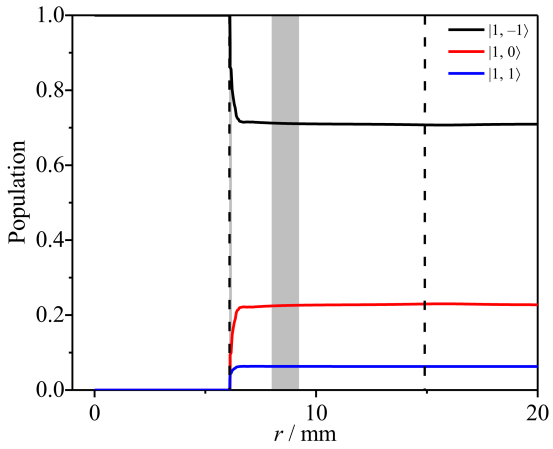

Figure 5.10: Simulated $|J, MK\rangle = |1, -1\rangle$ fraction of total population in $J_K = 1_1$ probed when the current stainless steel mesh holder is replaced with an insulating material so that only the narrow region of the mesh (0.1 mm thick) is held at zero voltage. The fraction of population is measured at different distances from the guide exit ($r = 0$ mm) as molecules travel through the different field regions of the apparatus. Figure reproduced from [168].

the problem. By amending the "off-time" period of the DIT and timing it with the incoming internally and translationally cold beam of molecules, one could allow the oriented molecules to be admitted to the trapping region without interference from the RF trapping fields – thus enabling the investigation of the effect of orientation on ion-molecule reaction systems.

Chapter 6

Charge exchange of cold Xe^+ with ammonia neutrals

In this chapter, the charge exchange reaction between sympathetically-cooled Xe^+ ions and ND_3/NH_3 molecules is examined in a linear Paul trap. For the first set of experiments, as described here, the neutral gas was introduced at room temperature via a leak valve, rather than via one of the sources described in chapter 3. Studying the reaction with thermal neutral reactants represents an essential preliminary step, paving the way for future experiments using cold molecule sources in combination with the Paul trap; in order to ascertain the temperature dependence of the reaction processes, and to establish the details of what occurs at the lowest temperatures, it is fundamental to first investigate what happens under room temperature conditions. Charge exchange reactions are monitored by recording images of the LIF pattern of the Coulomb crystal as a function of time. The numbers of co-trapped reactant (Xe^+) and product ions (ND_3^+ or NH_3^+) are established via LIF imaging analysis (with the aid of Coulomb crystal molecular dynamics simulations) and TOF-MS (using the DCT TOF-MS approach presented in chapter 4). In this way, we can establish an experimental protocol for examining ion-neutral reactions with unprecedented control

over the reactants and exceptional detection sensitivity of the ionic products.

6.1 The reaction of xenon ions with ammonia

6.1.1 Choice of the system

The study of the charge exchange reaction between ammonia and Xe^+ serves as a preliminary study to asses the performance of the combined apparatus. In addition to the charge exchange process, a number of other reaction pathways (involving hydrogen abstraction or subsequent dissociation of the ammonia ion) are possible for the Xe^+/NH_3^+ system. However, only the charge transfer pathway is exothermic (with the other pathways having endoergicities > 1 eV) [144]. Previous thermochemical studies have established that at thermal energies and below, only the simple charge transfer process occurs [183], namely:

$$Xe^+(^2P_{3/2}) + NH_3(^1A_1) \rightarrow Xe(^1S_0) + NH_3^+(^2A_1) \tag{6.1}$$

There are various reasons for the choice of the Xe^+ + ammonia reaction system. Firstly, owing to their permanent dipole moment, ammonia molecules can be decelerated (or, alternatively, guided) via the Stark decelerator available in the current setup. Additionally, the REMPI spectrum of ammonia (as mentioned before) has been well studied in the past. Hence, ammonia constitutes an excellent neutral reactant for our proof-of-concept study.

Regarding the choice of the reactant ionic species, xenon ions present the advantage of being conveniently produced *in situ* through a REMPI scheme utilising a pulsed dye laser available in the laboratory. In this initial proof-of-concept study, atomic ions are preferable over molecular ions since the presence of internal energy levels would complicate the data analysis and interpretation of the results. It should be noted

that, when working with calcium Coulomb crystals, Xe^+ is at the mass limit of singly charged species that can be sympathetically cooled, owing to its mass being more than three times the mass of calcium ions. As mentioned in Chapter 2, for efficient sympathetic cooling, the optimal relative mass-to-charge ratios range of the co-trapped species with respect to the laser cooled species is $\sim 0.4 - 2.5$. While the relative mass-to-charge ratio of Xe^+ is slightly outside the ideal range, Xe^+ is preferable over lighter noble gas ions since it does not undergo charge transfer reactions with species such as O_2 or H_2O that may be present at low partial pressures in the ion trap.

During the charge exchange reaction, calcium ions in the Coulomb crystal act as inert spectators (and as a "heat sink" through the sympathetic cooling process); this aspect is a key point for choosing this particular reaction. If the chosen (decelerated) neutral species (ammonia in this case) reacted with the Ca^+ ions, then (considering the three calcium ion energy levels addressed with the cooling lasers) a deconvolution of the relative contribution from ground and excited states of Ca^+ would be necessary. While this can in principle be done by adopting the optical Bloch equations for a three-level system (see [88]), it significantly complicates the analysis and interpretation of the data. Moreover, the choice of a system where the reactant ion (Xe^+) is heavier than the laser-cooled species (Ca^+) and the product ion (NH_3^+ or ND_3^+) is lighter means that the process can be studied by both imaging and TOF-MS methods, allowing us to follow the reaction from start to finish (via imaging of the LIF pattern) and then to independently verify the relative numbers and mass-to-charge ratios of all ions within the crystal at the point of ejection by TOF-MS.

The charge exchange reaction between Xe^+ and NH_3 has been investigated at room temperature in the past, and these previous results serve as a benchmark for our experimental data. Using a selected-ion flow tube (SIFT) apparatus, Alge and co-workers examined the reaction of NH_3 with Xe^+ in the ground $^2P_{3/2}$ and first excited $^2P_{1/2}$ states [184]. At 300 K, they obtained rate constants of 8.3×10^{-10} cm^3 s^{-1} and

1.8×10^{-10} cm^3 s^{-1}, for $Xe^+(^2P_{3/2})$ and $Xe^+(^2P_{1/2})$ (respectively). Average-dipole orientation (ADO) theory [185] predicts a reaction rate constant of 1.66×10^{-9} cm^3 s^{-1} for $Xe^+(^2P_{3/2})$ with NH_3 at 300 K, a factor of two higher than that reported experimentally [184].

6.1.2 Observations with NH_3 and ND_3

To my knowledge, there have been no comparable studies performed using deuterated ammonia. And yet, investigating the differences in reactivity of the two neutral reactants (using sympathetically-cooled Xe^+ and room temperature effusive sources) could provide some very interesting insights into the relative reactivity of NH_3 and ND_3, in addition to allowing us to make a direct comparison with existing predictions and measurements conducted on NH_3.

Since there is no bond breaking or conformation change during the charge exchange reaction, no substantial kinetic isotope effect is expected [7]. While detailed potential energy surface calculations are not yet available, existing calculations indicate that the process is barrierless (*i.e.* there is no activation barrier, although there may be submerged barriers along the reaction coordinate [186]). The long-range intermolecular forces play a key role in the barrierless processes. Specifically, the long-range interaction potential $V(R)$ governing ion-neutral reactions can be expressed as [187, 188]:

$$V(R) = -\frac{q\mu_D \cos\beta}{R^2} - \frac{q\mu_Q(3\cos^2\gamma - 1)}{2R^3} - \frac{\alpha q^2}{2R^4} + ... \tag{6.2}$$

where $\vec{R}$ is the separation of the centres of mass of the two reactants, q is the charge of the ion, $\vec{\mu}_D$ is the permanent electric dipole moment of the neutral reactant, β is the angle between $\vec{\mu}_D$ and $\vec{R}$, $\vec{\mu}_Q$ is the electric quadrupole moment of the neutral reactant, γ is the angle between $\vec{\mu}_Q$ and $\vec{R}$, and α is the polarisability of the neutral reactant. Previous studies on the dielectric properties of NH_3 and ND_3 demonstrated differences

in the electric dipole moment and polarisability between the two isotopologues [189, 190]. Therefore, one might expect the rate coefficients for $Xe^+ + NH_3 \rightarrow Xe + NH_3^+$ and for $Xe^+ + ND_3 \rightarrow Xe + ND_3^+$ to be different, arising from the distinct μ_D and α terms in the long-range interaction potential.

This chapter describes the experiments undertaken to ascertain any differences between the two rate coefficients within calcium ion Coulomb crystals, using room temperature ammonia molecules and sympathetically cooled xenon ions, before conducting experiments using internally and/or translationally cold ammonia molecules. We need to understand how the two systems react at room temperature before going to very low temperatures and controlling the properties of the reaction process (such as the internal state distribution of ammonia and the collision energy). In this way, we will gain insight into the role that each experimental variable plays on the reaction process.

6.2 Experimental methodology

The charge exchange reaction between xenon ions and ammonia neutrals is examined using the linear Paul trap combined with the Stark decelerator and described in detail in section 2.3.1. The trap is operated under UHV conditions ($P \approx 7 \times 10^{-10}$ mbar) and the reaction is monitored by observing the changes of the LIF pattern of the Coulomb crystal via a CCD camera and a 10x objective lens (see section 2.3).

Instead of using the Stark decelerator to admit ammonia molecules into the chamber, measurements are first conducted using an effusive (room temperature) source of ammonia. It should be noted that, before switching from ammonia to deuterated ammonia, the chamber is baked for a couple of days at ≈ 100 °C to remove any impurities from the ion trap chamber.

Data collection protocol

For each experimental scan, a stable Ca^+ Coulomb crystal is formed. As previously explained in Chapter 2, Ca^+ Coulomb crystals are formed by the non-resonant ionisation (at 355 nm) of an effusive, skimmed calcium atom beam at the trap centre. A main laser cooling beam, addressing the 4s $^2S_{1/2} \rightarrow$ 4p $^2P_{1/2}$ transition at 397 nm, and a 866 nm repump beam, returning population from the dark 3d $^2D_{3/2}$ state to the main cycle, serve to laser-cool Ca^+ ions. Bi-directional cooling is achieved by reflecting the cooling lasers back along the trap axis.

Once a stable Ca^+ crystal has been formed, xenon gas is introduced to the reaction chamber through a high-precision leak valve[1] until a chamber pressure of $2 - 5 \times 10^{-9}$ mbar is measured on the pressure gauge. A 249.6 nm frequency-doubled pulsed dye laser beam (5 ns pulse length, 0.8 mJ/pulse) is then admitted into the chamber to ionise xenon at the trap centre via a $(2 + 1)$ REMPI scheme. The resulting Xe^+ ions are sympathetically cooled into the Coulomb crystal. The presence of xenon ions is inferred from the characteristic flattening and elongation of the fluorescing Ca^+ framework, as the heavier Xe^+ ions form a dark outer shell (see figures 2.6 and 6.1). The Ca^+/Xe^+ bi-component crystal reaches a stable temperature (judged by the sharpness of the spots in the images) within $10 - 60$ s under our experimental conditions.

Once the bi-component crystal is stabilised (after ≈ 60 s), room temperature neutral ammonia reactant molecules are admitted into the chamber via a second precision leak valve, with charge exchange reactions occurring at partial pressures of up to 1×10^{-9} mbar. Reaction rate coefficients are calculated using a combination of crystal image analysis and mass-sensitive determination of the ions present in the crystal, as a function of reaction time.

[1]Kurt J. Lesker, Manual SS All-Metal Leak Valve (CF flanged): LVM Series.

Observations

The ammonia molecules do not react with the Ca^+ in the Coulomb crystal. To confirm this, we prepared a Ca^+ Coulomb crystal, then introduced ammonia molecules using the precision leak valve and monitored changes in the crystal over time, also ejecting the crystals at different times as a quantitative measure of all ionic species present. The absence of any dark core (in the LIF pattern) and of any mass channel other than Ca^+ ions in the TOF trace confirms that no reaction occurs between neutral ammonia molecules and Coulomb-crystallised Ca^+ ions.

Xenon ions are formed through a $(2+1)$ REMPI process accessing the $5p^5 6p\ ^2P_{3/2}$ intermediate state. The adopted REMPI scheme yields 22% of the ions in the excited spin-orbit state $^2P_{1/2}$ and the remainder in the lower $^2P_{3/2}$ state [191]. The population in the higher energy state $^2P_{1/2}$ decays to the lower state $^2P_{3/2}$ via a magnetic-dipole mediated transition on a time-scale of $\approx$ 48 ms [192]. Considering the significantly longer time interval ($\approx$ 60 s) between formation of a Ca^+/Xe^+ bi-component crystal and admission of ammonia reactant neutral molecules, it is safe to assume that all the xenon ions have relaxed into the ground ionic state prior to reacting.

No background reactions occur between Xe or Xe^+ and Ca^+ (the charge transfer from Ca^+ to Xe is highly endoergic). Ion loss from the trap is negligible on the time-scale of the reaction (a few minutes), as confirmed from the absence of impurity ions in the TOF traces (see figure 4.5) and the constant number of calcium ions in the simulated crystal images that best match the experimental data.

Impurity ions lighter than calcium could also contribute to the formation of the inner core, which distorts the results. To this end, background reaction scans were conducted, and confirmed that the contribution of any impurity ions is negligible. The imaging study is complemented by DCT TOF-MS analysis, as detailed in chapter 4.

6.3 Analysis

The charge exchange reaction is studied via imaging analysis of the rate of growth of a Coulomb crystal dark core (corresponding to non-fluorescing ammonia ions) using the numerous LIF images collected during each scan.

6.3.1 Evaluating the reaction rate coefficient

The reaction between ammonia and xenon ions is a one-to-one process, meaning that each Xe^+ ion consumed by the reaction yields an ammonia product ion. Considering ND_3 (the same applies to the reaction involving NH_3), the rate coefficient can be expressed as :

$$\frac{\mathrm{d}[\mathrm{Xe}^+]}{\mathrm{d}t} = -k_2[\mathrm{Xe}^+][\mathrm{ND}_3], \tag{6.3}$$

where $[Xe^+]$ and $[ND_3]$ represent the number densities of each reactant species and k_2 is the bimolecular rate coefficient.

Assuming there is no loss of Xe^+ ions from the crystal (except by reaction with ND_3) leads to the expression:

$$[\mathrm{Xe}^+] = [\mathrm{Xe}^+]_0 - [\mathrm{ND}_3^+] \tag{6.4}$$

and combining equations 6.4 and 6.3 yields

$$\frac{\mathrm{d}[\mathrm{ND}_3^+]}{\mathrm{d}t} = k_2[\mathrm{ND}_3]([\mathrm{Xe}^+]_0 - [\mathrm{ND}_3^+]). \tag{6.5}$$

With the assumption of a constant flow of ND_3, equation 6.5 simplifies to

$$\frac{\mathrm{d}[\mathrm{ND}_3^+]}{\mathrm{d}t} = k_1([\mathrm{Xe}^+]_0 - [\mathrm{ND}_3^+]), \tag{6.6}$$

where k_1 is a pseudo first order rate coefficient

$$k_1 = k_2[\mathrm{ND_3}]. \tag{6.7}$$

By integrating equation 6.6 it can be seen that:

$$[\mathrm{ND_3^+}](t) = [\mathrm{Xe^+}]_0 \left(1 - e^{-k_1 t}\right), \tag{6.8}$$

From this, the pseudo first order rate coefficient can be evaluated and thus also the bimolecular rate coefficient (equation 6.7), if the number density of ND_3 and the initial number density of Xe^+ are known.

The pseudo first order rate coefficient can be calculated by plotting the number of ND_3^+ ions against the reaction time and fitting the dark core growth curve to an exponential curve according to equation 6.8, as illustrated in figure 6.6. Therefore, the number of ND_3^+ ions has to be determined for different reaction times.

6.3.2 LIF imaging analysis

Asymmetry

The data for the charge exchange reactions involving room temperature ammonia have been collected following the relocation of our laboratory to another building. The experimental images of these crystals exhibit a slight distortion from the ellipsoidal symmetry expected under normal operating conditions (see figure 6.1). Moreover, the TOF traces are not consistent and usually show no presence of light species despite the images on the camera clearly indicating the presence of a dark core in the fluorescence pattern (see figure 6.2). Surprisingly, there is also a significant pick-up noise on the TOF traces synchronized with the rising and falling edges of the ejection pulses (see figure 6.2).

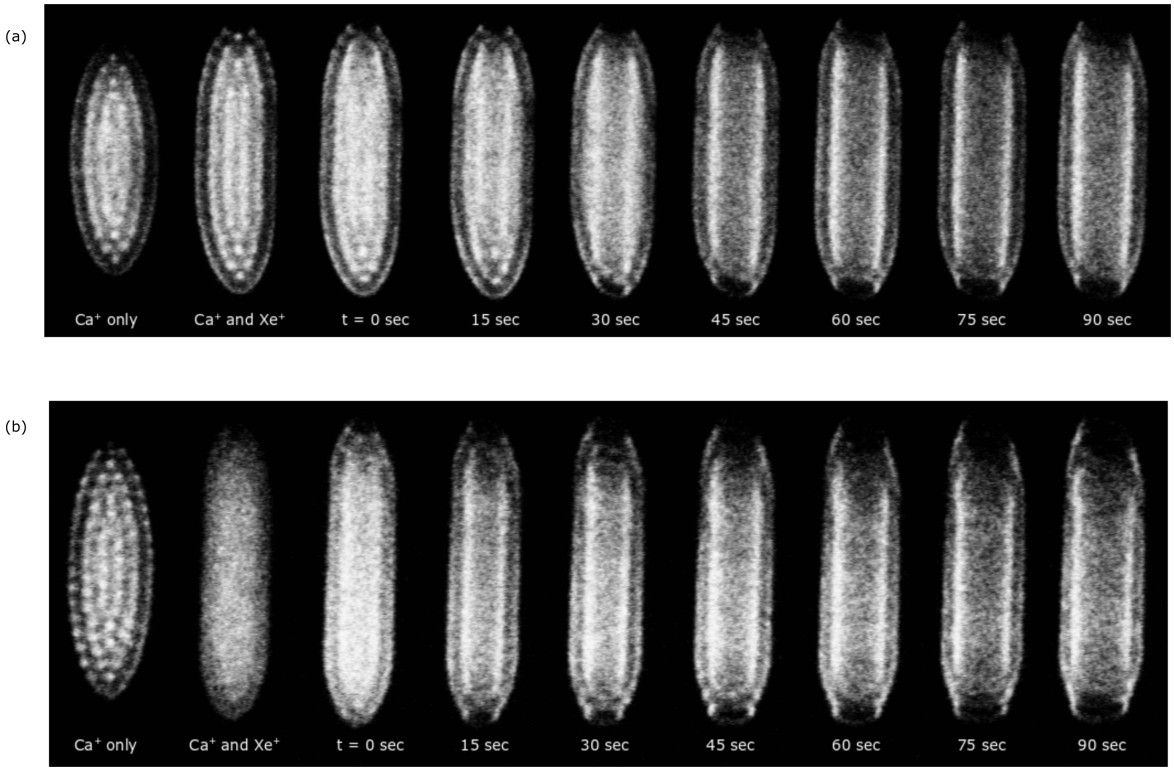

Figure 6.1: Progression of the charge exchange reaction with ammonia (panel (a) and (b) for ND_3 and NH_3, respectively) monitored through the LIF pattern of the Ca^+ ions within the Coulomb crystal. The images clearly show the distortion of the Coulomb crystal ellipsoidal symmetry due to the malfunctioning of the ion trap.

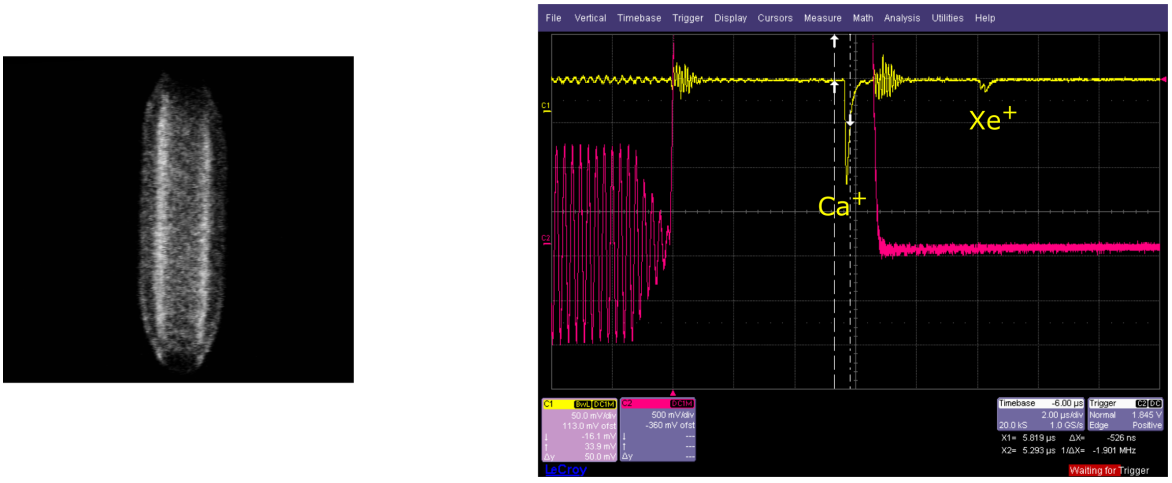

Figure 6.2: (a) LIF pattern of a multicomponent Coulomb crystal. (b) Oscilloscope signal of the MCP (in yellow), and of the ejection pulse (in magenta) TOF trace, recorded when ejecting the multicomponent crystal shown in panel (a). The scale of the scope had to be reduced down to 50 mV/division to be able to see the peaks on the trace. The presence of a detrimental pick-up noise on the trace is evident at the rising and falling edges of the ejection pulse.

Following extensive data collection, when inspecting the trap chamber for diagnostics, one of the ion trap rods was found to be misplaced, exhibiting a significant axial shift. At the time of writing, the issue with one of the rods being misplaced has been rectified, and preliminary data that has been subsequently collected confirms that the symmetry of the Coulomb crystals is as it should be (see figure 6.3). The TOF traces are again providing quantitative data about the identities of all species within the crystal at a selected reaction time. The misplaced ion trap rod explains both the lack of symmetry observed in the crystals and the poor detection efficiency of lighter species on the TOF-MS traces (see figure 6.2), as the fields would have been asymmetric. Lighter species are most affected by imperfect ejection fields, as these species are the most easily deflected.

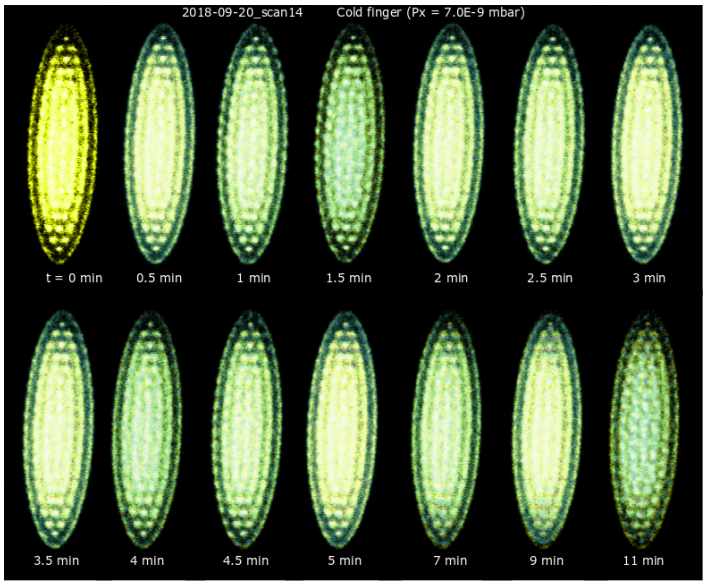

Figure 6.3: Sequence of LIF images recorded whilst monitoring the evolution of a Ca^+ ions Coulomb crystal as a function of time (with no reactant neutral gas present). The images show the typical ellipsoidal symmetry (and stability) of the Coulomb crystals has been achieved following the adjustment of the ion trap.

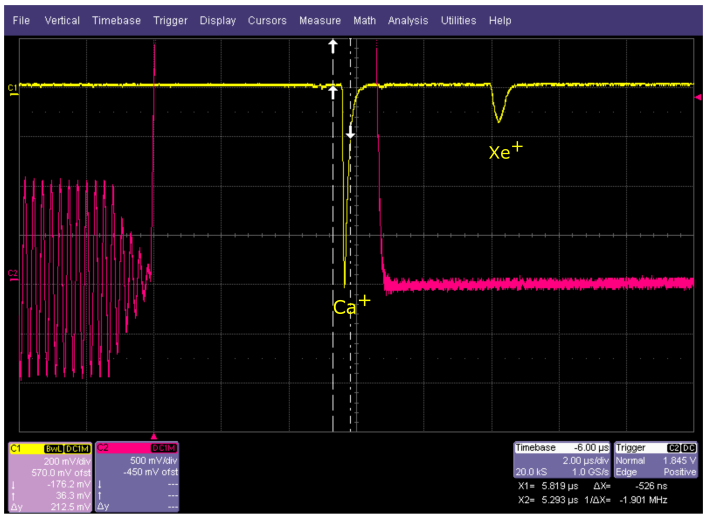

Figure 6.4: TOF signal of the MCP (in yellow) and the ejection pulse (in magenta) recorded on the oscilloscope when ejecting a Ca^+/Xe^+ bi-component crystal. Following the trap rod adjustment, the detection efficiency of the DCT TOF-MS has been recovered (the scale on the scope channel is an order of magnitude higher than when the trap was not correctly functioning). Moreover, the pick-up noise, previously superimposed on the MCP signal is no longer present.

Dark core volume analysis

An imaging manipulation `Python` script (see Appendix A) has been written to take into account the ellipsoidal symmetry of the experimental LIF images of the crystals in order to facilitate the use of the aforementioned collected data (and negating the need for the TOF-MS analysis, which was not able to be relied upon for this set of measurements).

A `MATLAB` code, called `CCRTA`, has been previously developed (by past members of the group [88]) in order to calculate the volume of the "dark" (non-fluorescing) core present in the images of Coulomb crystals incorporating species lighter than the laser-cooled ion (Ca^+, in our case). Using a graphical interface unit (GUI), it is possible to fit an ellipsoidal perimeter around the LIF pattern in a given experimental CCD image (see figure 6.5). The code outputs the volume and an estimated ion count based on a number density formula derived from the fluid model of a trapped plasma at zero temperature:

$$n_0 = \frac{4\epsilon_0 {V_{RF}}^2}{m{\Omega_{RF}}^2 r_0^4} \tag{6.9}$$

where ϵ_0 is the electric permittivity in vacuum, m is the mass of one single ion; r_0, V_{RF}, and Ω_{RF} are the ion trap parameters described in Chapter 2. Despite being derived from liquid-phase plasma model (at $T \to 0$), it has been previously demonstrated that densities calculated using this formula are in agreement with the number density of ions in large (≥ 100 ions) Coulomb crystals [193, 194]. Details of the reaction kinetics can be extracted from this imaging analysis owing to the presence of time stamps allocated to each CCD image.

The graph in figure 6.6 illustrates how we intend to proceed in evaluating the pseudo first order rate coefficient using the dark core analysis. By fitting the dark core growth rate (from analysing the LIF sequence of images reported above the graph) to

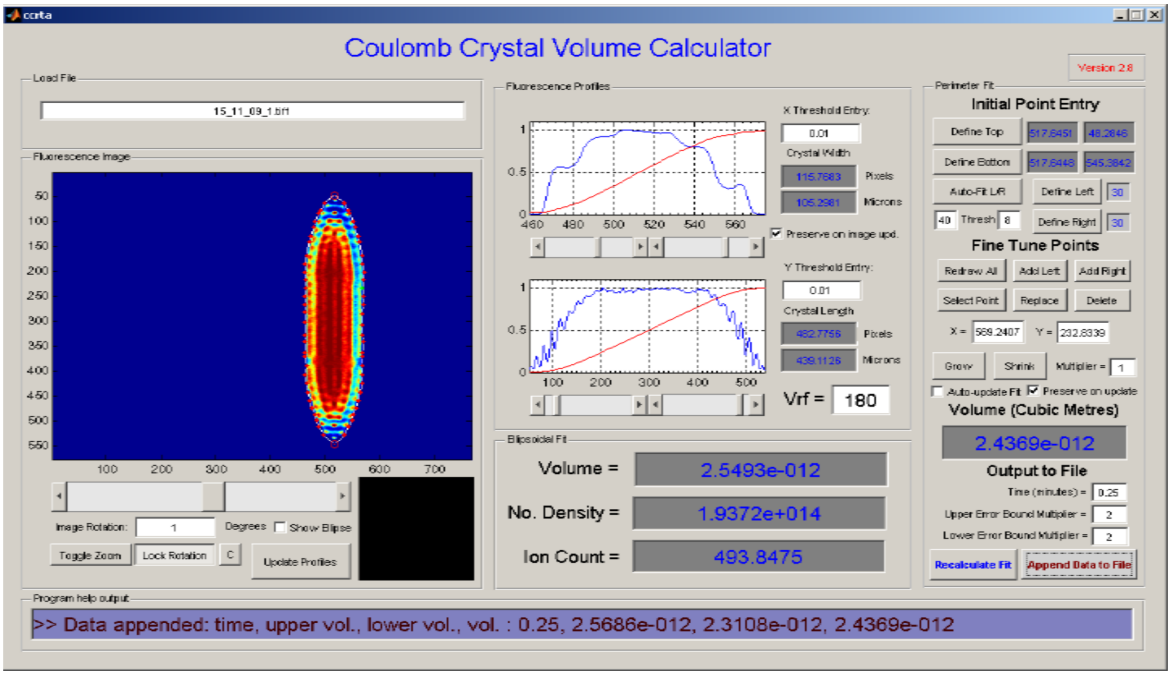

Figure 6.5: Screenshot image showing the GUI of the `CCRTA` program for the image analysis of the recorded Coulomb crystals.

the function in equation 6.8, we obtained a pseudo first order coefficient $k_1 = 1.52 \times 10^{-2}$ s^{-1} for the $Xe^+ + ND_3$ charge exchange reaction. At present, this approach is afflicted by various uncertainties in addition to the problems related to the asymmetry of the recorded crystals. For instance, we intend to use the residual gas analyser to ensure that the partial pressure of loaded ND_3 and NH_3 are the same. This is a key aspect, necessary to make sure the various experimental parameters are held constant – meaning that we can effectively directly compare the images and can clearly see the differences in reaction rate coefficient by eye. Moreover, now that the Paul trap (and DCT TOF-MS) malfunctioning has been rectified, we will soon be in a position to determine the bimolecular rate coefficient k_2 via the analysis of the TOF traces accompanying the sequence of LIF images for the new extensive session of experiments.

Given the large errors related to the evaluation of the height and width (and thereby the volume and number of ions) of the dark core when analysing the LIF images, we

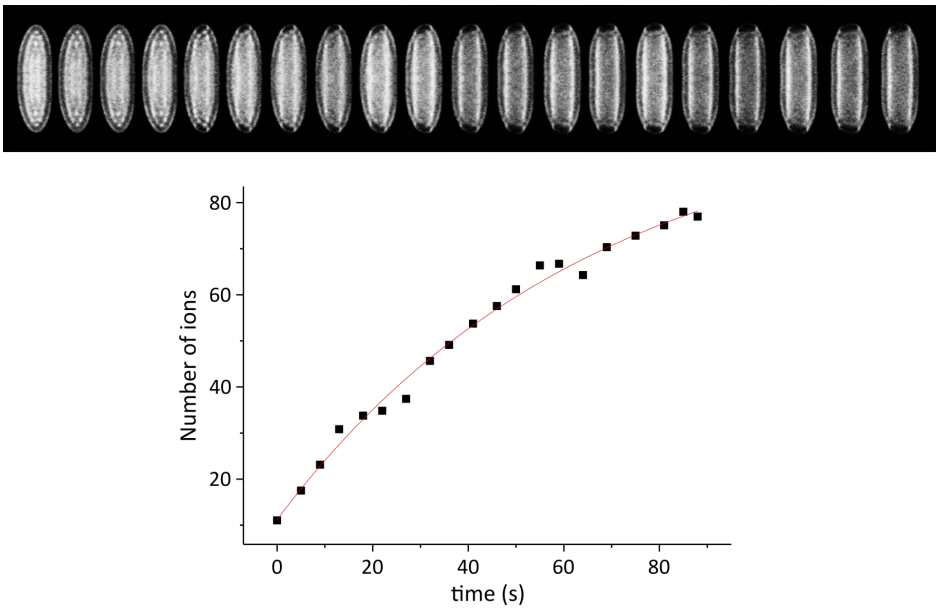

Figure 6.6: Example of preliminary analysis of a Coulomb crystal dark core growth rate. The reaction of sympathetically cooled Xe^+ ions with ammonia neutral molecules can be investigated through the evaluation of the number of ammonia ions (ND_3^+ in this case) in the crystal as a function of time. The data are fit to the experimental growth function according to equation 6.8.

are developing a more robust imaging analysis approach, building on initial work conducted by K. Park (a visiting student in our group). Unlike `CCRTA`, the new code does not rely on a user establishing the LIF ellipses perimeters via a GUI; instead, it uses geometrical and empirical considerations to find the edges of the LIF and to perform the fitting protocol on the experimental images. The code is in the process of being tested and optimised with the prospect of automating the dark core analysis, as it also has the ability to process a batch of images at a time.

6.4 Outlook

The collected data for both ammonia isotopologues reactant molecules at room temperature has been qualitatively analysed using the imaging analysis methodology outlined above. However, owing to the imperfection in the experimental set-up, we will have

large uncertainties in the resulting findings and cannot rely on the TOF-MS traces for quantitative measurements. The experiments are currently being repeated now that the cause of asymmetry has been identified and solved. With the trap electrodes correctly placed, the DCT TOF-MS detection method can be safely used to unambiguously ascertain the masses and relative abundances of the various ion products at a given time, allowing us to subsequently evaluate the reaction rate coefficient. The high sensitivity of the DCT TOF-MS methodology (developed as part of the work for this thesis) will enable one to investigate, for example, the relative reactivity of H and D in ion-molecule reactions – an area of high importance astrochemically, with the mechanism for deuterium fractionation yet to be confirmed.

Preliminary charge exchange reaction data has also been collected using the Stark decelerator as an electrostatic guide. In this configuration, static voltages $\pm V_{DC}$ (with $V_{DC} \leq 4$) are applied to the electrode pairs of the decelerator. No voltage switching takes place and therefore ammonia molecules are neither decelerated nor accelerated. While there is no overall change in kinetic energy (*i.e.* no deceleration takes place), the Stark potential energy experienced by ammonia molecules in LFS states leads to a transverse focusing force exerted on these molecules. Therefore, the decelerator in "guiding" mode can yield a high flux of molecules that can be varied in intensity by altering the static voltage [7, 144]. With the Stark decelerator used in guiding mode, a beam of internally cold (via supersonic expansion) ammonia is obtained with a high (but narrow) velocity distribution. When recording these measurements, the pulsed valve of the Stark decelerator apparatus is operated at 10 Hz. The shutter is opened such that the guided ammonia molecules (in LFS) can reach the ion trap chamber. A slightly higher ADO theory rate constant of 2.2×10^{-9} cm^3 s^{-1} is expected when operating under these experimental conditions [144]; the average collision energy between trapped, sympathetically-cooled Xe^+ ions – with a translational temperature on the order of $10 - 20$ K, as established by MD simulations – and the 385 m s^{-1}

Figure 6.7: Photograph of sections of the Stark decelerator illustrating the PEEK spacing elements introduced along the Stark decelerator beamline in order to prevent the long and heavy stainless steel structure from bending under the effect of the force of gravity and the mechanical stress due to the pump vibrations.

ammonia beam is approximately 13 meV (or 150 K).

Finally, once the measurements with room temperature effusive ammonia (and deuterated ammonia) molecules are completed, extensive data will be collected using the Stark decelerator to probe reactions at low collision energies and to test any single-state selectivity effect. Since the move of laboratories there have been electrical shorting problems related to the Stark decelerator, caused by some electrodes touching or being too close one another. In this regard, PEEK spacers (see figure 6.7) have been constructed and installed to improve the structural integrity so that the four rods of the decelerator (and consequently all the electrodes mounted on the rods) are maintained at the same distance along the entire length of the decelerator.

Hence, future experiments will be conducted at low collision energies, on the order of $10 - 100$ K, through the use of a Stark decelerated beam of ND_3 (or NH_3). While the density of decelerated ammonia will be up to an order of magnitude lower than in this work, examining the charge exchange between Xe^+ and ammonia as a function of collision energy will still be possible due to the high prescision and sensitivity offered by the DCT TOF-MS methodology. In this way, one could systematically test

the validity and accuracy of various capture theories over a range of collision energies and for a diverse range of ion-molecule reaction systems. For instance, the measurements obtained in these various configurations will represent a close comparison to the $N^+ + NH_3 \rightarrow N + NH_3^+$ charge exchange reaction studied with the CRESU technique and modelled by D. Clary through the capture theory known as "Adiabatic Capture Centrifugal Sudden Approximation" (ACCSA) [89].

Despite the aforementioned difficulties, the preliminary data illustrated in this chapter represent fundamental groundwork towards the study of the cold charge exchange reaction between xenon ions and ammonia molecules, with the interesting prospect of observing any differences in reactivity between the two isotopologues. The next chapter concludes this thesis and outlines possible avenues for future work.

Chapter 7

Conclusions

This thesis has described the significant experimental progress made towards the study of controlled reactive collisions between trapped ions and polar neutrals at low temperatures. The initial three chapters have discussed how cold ions and molecules can be formed, with particular focus on the use of Coulomb crystals and on the experimental apparatuses employed for the experiments conducted as part of the work presented here.

As detailed in chapter 4, a Paul trap time-of-flight mass spectrometer has been pioneered to ascertain the masses and abundances of the ions in a Coulomb crystal at a given time. As a result of the introduction of a time interval in which the ion trapping fields are quenched prior to the ejection pulse, high detection efficiency and good resolution are achieved with this new setup. The optimisation of the ejection voltages yields a mass resolution of 1 u for a wide range of masses of interest (up to 58 u), which is sufficient for most reactions of interest. The resolution could be improved if necessary through the addition of ion optic focusing elements or by extending the length of the flight tube. The technique is broadly applicable and favourable over already existing Coulomb crystal detection techniques for the quantitative characterisation of ion-molecule reactions. Owing to the ability to accurately interrogate the contents of

a crystal at a given time during a reaction, this method represents a powerful tool for calculating the rate constants of reactions occurring at low temperatures.

As outlined in the introduction, a key objective of our research is to achieve full control over the various reaction parameters to unravel hidden details of the kinetics and dynamics of the reactive processes. The ability to investigate reactions at low temperatures allows one to investigate features that can be masked at higher temperatures due to thermal averaging. With the ultimate goal of achieving control over all reaction parameters, the extent to which the orientation of buffer gas cooled molecules exiting the electrostatic guide can be controlled has been examined. By conducting linearly-polarised light REMPI measurements and spectral fitting with simulated REMPI spectra, the residual orientation of internally and translationally cold ammonia molecules at the point of spectroscopic probing has been calculated. As a result of state-tracking trajectory simulations, it has been possible to propose schemes to achieve full orientation of cold guided ammonia molecules. A linear Paul trap has then been installed in place of the planar electrodes utilised for the studies on the orientation of buffer gas cooled and velocity selected ammonia molecules. The apparatus is therefore complete for facilitating the study of cold reactive collisions within a Coulomb crystal. Owing to the unique features of the buffer gas cooled Stark guide apparatus, it will be possible to study the effect of rotational cooling on the reaction rates, thereby testing post-Langevin theories (such as those proposed decades ago by D. Clary [87]) which have not yet been verified due to the technical challenges of performing experiments at low temperatures.

The ongoing investigation into the charge exchange reaction between sympathetically cooled Xe^+ and room temperature ammonia has been discussed. Notably, improvements to the LIF imaging analysis protocol can facilitate a complementary approach to the DCT TOF-MS for calculating rate constants of the aforementioned reaction. With the important contribution of A. Tsikritea, extensive measurements are

being repeated now that the cause of Coulomb crystal asymmetry (and poor TOF-MS detection efficiency) has been solved by readjusting the Paul trap electrode rods. Not only will this analysis serve as a useful reference for comparison with the anticipated cold state-selected reaction achievable using the Stark decelerator; it will also provide valuable information regarding any interesting isotope effects on this charge exchange process.

In order to investigate a fully state-selected, tunable energy ion-molecule reaction, measurements must be conducted employing the apparatus comprising a Stark decelerator combined with a Paul trap. The recent issues with the Stark decelerator structural integrity have been addressed by introducing supporting elements made of PEEK. Hence, we will soon be in a position to perform experiments of the charge exchange reaction between sympathetically cooled xenon ions and cold (decelerated) ammonia neutrals and thus to compare the results with experiments conducted using room temperature effusive ammonia. In order to fully characterise this reaction, the ammonia molecules will be decelerated to different final velocities, in order to determine temperature-dependent rate constants. Notably, the low collisions energies achievable with the Paul trap combined with the Stark decelerator are well-suited to investigate reactions at conditions that are astrochemically relevant.

With the ultimate goal of achieving state-to-state control over a given reaction, a cryogenic ion trap is in the process of being constructed in our research group. By operating the ion trap at a temperature of 30 K (or lower), it will be possible to suppress the population redistribution of molecular ions interacting with the BBR field, thereby maintaining the desired state selectivity that is attained on initial formation by REMPI [127]. Owing to the enhanced control over the internal state of the reactants and the further cooling afforded by the devised apparatus, it will be possible to expand the scope of the chemistry that can be investigated in the cold regime.

Appendix A

LIF image manipulation code

This appendix illustrates in detail the function of the code that has been written to facilitate the analysis of the experimental images of the fluorescence pattern of Coulomb crystals collected in the laboratory. This part of the thesis is presented to explain to other group members how to initialise and use the code for processing the LIF images prior to imaging analysis.

An imaging manipulation `Python` script, called `enhance-LIF.py`, has been written to reconstruct the ellipsoidal symmetry of the experimental LIF images of the crystals recorded with the misaligned Paul trap electrodes. The code can operate in batch mode to process thousands of images in a few seconds.

Prior to recovering the expected ellipsoidal symmetry of a Coulomb crystal LIF pattern, the code corrects the camera+lens image distortion along the axis orthogonal to the trap. This distortion consists of a $\approx 25\%$ compression along the CCD camera horizontal axis which has been calculated using the software `ImageJ2` [132] and a graticule (ruler) with a calibrated step resolution of 10 μm. The Python code horizontally stretches each pixel of a given experimental image by a factor of 1.333. Moreover, to facilitate the comparison with the simulated LIF images obtained with the `ccmd` code, the code corrects the systematic tilt constantly present in all exper-

imental images of the crystals. The presence of a constant $+3^\circ$ deg (clockwise) tilt angle is due to the fact that the CCD camera mounting arm places the camera with a -3° deg (anti-clockwise) tilt with respect to the Paul trap axis.

A.1 Tutorial

The code runs utilising version 2.7 of the `Python` programming language [161]. By downloading the `Anaconda` distribution [195] one can ensure that all the required libraries are correctly installed in an automatic way. The only required manual download involves the installation (within the `Anaconda` framework) of the computer vision libraries `openCV` [196].

First, the user has to create a global folder containing all the various collected data (these can also be organised in various sub-folders). Then a copy of the `enhance-LIF.py` file must be added to the global folder.

To run the code, one has to open the shell prompt (or command line) and type: ipython $--$pylab. Then, it is necessary to go to the aforementioned global folder through typing the command: cd Path-to-the-global-folder. Finally, to execute the script, the user has to type: run `enhance-LIF.py`, and then follow the instructions on the terminal (see figure A.1).

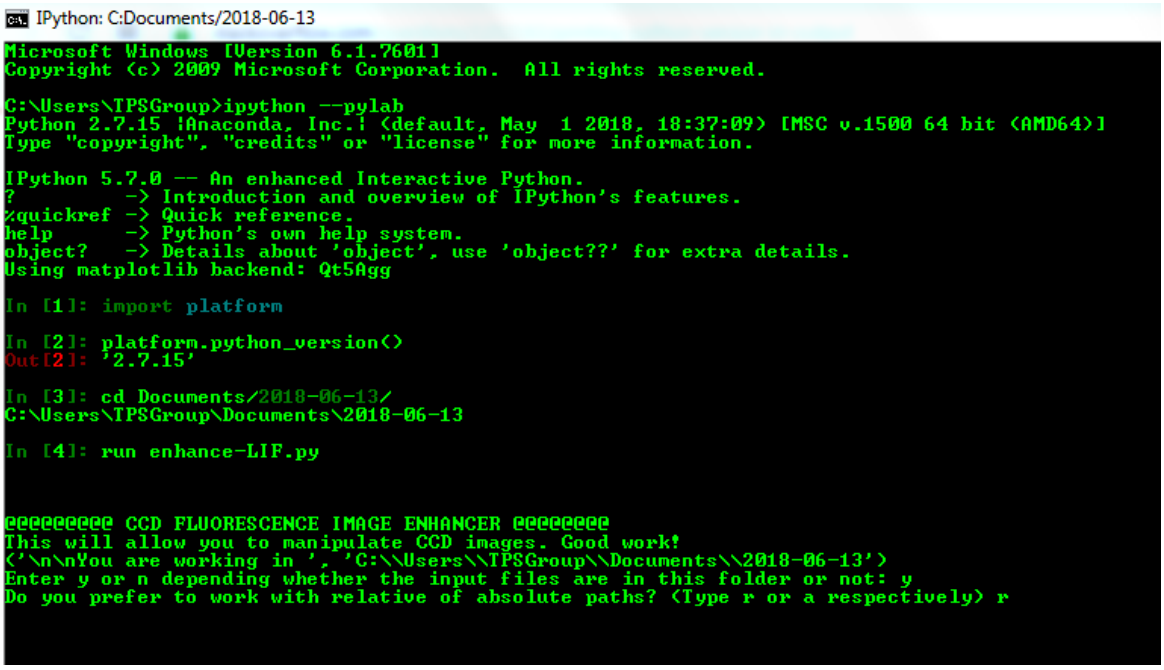

Figure A.1: Screen-shot image showing an example of the correct use of the command line to run the `enhance-LIF.py` code.

A.2 The `enhance-LIF.py` script

```
1
"""
2018-06 @ LorenzoPetralia
CCD LIF image editor for assisting Coulomb crystal laser-induced
    fluorescence pattern analysis.
Requires python (preferably) version 2, OpenCV version 3 and imutils
    libraries
The Anaconda environment is recommended to ensure the various imported
    packages are avialble).

"""
#############################################################
#                    IMPORTING LIBRARIES AND AUXILIARY PACKAGES
#############################################################
```

```
13 import numpy as np
   from matplotlib import pyplot as plt
   import os


17
   # import the necessary packages
   from imutils import contours
   from skimage import measure # if using scikit-image
21


   import imutils # set of convenience functions used to make applying image
       processing operations easier
   import cv2
25

   import platform
   import argparse # to use command lines arguments
   import os
29 import math



   ############################################################
33 #                      DEFINING MY FUNCTIONS
   ############################################################

   ##################### SAVE-UPDATE IMAGE ###############################
37 def saver(img, title, kind, place):
     cv2.imwrite(title+ "." +kind, img) #same folder
     #cv2.imwrite(place + title+ "_full." +kind, img) #same folder
     #print("image "+ title+ "." + kind + "  saved in:  " + place)
41
```

```
#################### RESIZE #################################
# resize the image maintaing aspect ratio and display it

def resizer(img, scale, x=True, y=True):
    """
    RESIZE image according to a certain scale factor (enlarge if scale is
     >1, reduce if scale <1)
    If you don't want to resize both axis, choose False for either x or y.
    """
    horiz= img.shape[1]    #image width - array columns
    vertic=img.shape[0]    #image hight - array rows
    channels=img.shape[2]
    ratio= horiz/vertic
    if x== True:
        new_horiz= int(horiz*scale) # in x pixels
        if y==True:
            new_vertic=int(math.floor(new_horiz/ratio))
        else:
            new_vertic=vertic
    elif x==False:
        new_horiz=horiz    # no horizontal rescaling
        new_vertic= int(vertic*scale) # in y pixels
    dims= (new_horiz, new_vertic)
    newsize_image= cv2.resize(img,dims, interpolation= cv2.INTER_AREA)
    return newsize_image


#################### ROTATE #################################
def rotate(img,angle,fix=True):
    if fix== True:
```

```
        # simple rotation maintaining same matrix size - could risk to crop
        the object though
        rotated_img= imutils.rotate(img, angle)          # positive angle
        for anticlockwise rotation
        print("simple rotation - image dimensions: ", rotated_img.shape)

    else:
        # careful rotation - no part of image is lost
        rotated_img=imutils.rotate_bound(imag, -angle)    # negative for
        anticlockwise rotation
        print("correct rotation - image dimensions: ", rotated_img.shape)

    return rotated_img


#################### GRAY SCALE ##################################
def monochrome(img):
    """
    In this way compress the RGB into one channel. Therefore from a (hight
      ,width, 3) matrix image to a (hight ,width)
    """
    grayimg= cv2.cvtColor(img, cv2.COLOR_BGR2GRAY)
    #cv2.imshow("image in grey scale", grayimg)
    return grayimg



def clean_erosion(img):  #OPTIONAL

    eroded = cv2.erode(img, None, iterations=1)
    #cv2.imshow("image cleaned erosion", eroded)
```

```
    return eroded


105


    ##################### ROIs - regions of interest ##################
109 #MARGINAL INTEGRATION FOR INTENSITY PROFILES AND THEREFORE MEASURING
        OBJECT EXTENT

    def ROIs(img,y_rate, x_rate):
        xprofile=np.sum(img, axis=0)
113     yprofile=np.sum(img, axis=1)
        # plt.figure("Fluorescece profiles")
        # plt.title("Fluorescece profiles")
        # plt.subplot(211)
117     # plt.plot(xprofile)
        # plt.xlabel("x pixels")
        # plt.ylabel("horizontal profile")
        # plt.subplot(212)
121     # plt.plot(yprofile)
        # plt.xlabel("y pixels")
        # plt.ylabel("vertical profile")

125     # #def differentialprofile()
        # xgrad=np.gradient(xprofile)
        # ygrad=np.gradient(yprofile)
        # plt.figure(2)
129     # plt.subplot(211)
        # plt.plot(xgrad)
        # plt.xlabel("x pixels")
        # plt.ylabel("horizontal grad")
```

```
133 # plt.subplot(212)
    # plt.plot(ygrad)
    # plt.xlabel("y pixels")
    # plt.ylabel("vertical grad")
137 # #plt.show()


    # vertical region of interest
141 ymax=np.amax(yprofile)
    ythreshold= ymax*(y_rate)
    ytrue= (yprofile>ythreshold)*1
    yroi= np.nonzero(ytrue)[0]
145 #print("Max cumulative y fluorescence is ", ymax)
    #print("these are the crystal ypixels \n\n",yroi)
    ystart=yroi[0]
    yend=yroi[-1]
149 cryst_hight= yend - ystart
    print("crystal hight: ", cryst_hight, " pixels")


153 # horizontal region of interest
    xmax=np.amax(xprofile)
    xthreshold= xmax*(x_rate)
    xtrue= (xprofile>xthreshold)*1
157 xroi= np.nonzero(xtrue)[0]
    #print("Max cumulative x fluorescence is ", xmax)
    #print("these are the crystal xpixels \n\n",xroi)
    xstart=xroi[0]
161 xend=xroi[-1]
    cryst_width= xend - xstart
    print("crystal width: ", cryst_width, " pixels")
```

```
165   return (ystart,yend, xstart,xend)




169

   ##################### CROPP ###################################
   #CROP to highlight object at its boundaries
173 #img = cv2.imread("lenna.png")
   def cropper(img,ystart,ystop, xstart,xstop):
     cropped= img[ystart:ystop, xstart:xstop]
     return cropped
177

   ################ STITCHING TWO IMAGES ##########################
181 # stitch image together to create enhanced crystal
   #crop lowest horizontal line of pixel for the stitches
   def stitching(img, step=1, centrosymmetric=False):
     # step =1 crop lowest horizontal 1 line of pixel for the stitches
185  # horizontal axis flip of the lower half
     flip_img = cv2.flip(img, 0)
     if centrosymmetric == True:
       flip_img=cv2.flip(flip_img, 1) # also flip along vertical axis for a
      global centrosymmetric flip
189

     upper= flip_img[:-step]
     lower= img
     stitched= np.vstack((upper,lower))
193  #cv2.imshow("stitched", stitched)
     return stitched
```

```
197
#################### Padding image ##############################

# PADDING to restore 480 x 640 pixel file size
201
def padder(img, final_hight,final_width):

  top, bottom, left, right = (0,0,0,0)
205  print("pre padding",img.shape)
  if final_width < img.shape[1]:
    hcut= int((img.shape[1] - final_width)/2)
    img= img[:,hcut:img.shape[1]-hcut]
209
  if final_hight < img.shape[0]:
    vcut= int((img.shape[0] - final_hight)/2)
    img= img[vcut:img.shape[0]-vcut,:]
213



  if final_hight > img.shape[0]:
217
    if (final_hight - img.shape[0])/2 % 2 ==0:
      top= (final_hight - img.shape[0])/2
      bottom=top
221   else:
      top=int((final_hight - img.shape[0])/2) +1
      bottom=top -1

225  else:
    print("no vertical padding",img.shape)
    top=0
```

```
    bottom=0

229


    if final_width > img.shape[1]:

233

      if (final_width - img.shape[1])/2 % 2 ==0:
        left= (final_width - img.shape[1])/2
        right=left
      else:
237     left=int((final_width - img.shape[1])/2) +1
        right=left -1


241   else:
      print("no horizontal padding",img.shape)
      left=0
      right=0

245

    print(top, bottom, left, right)

    pad_image=cv2.copyMakeBorder(img, top, bottom, left, right, cv2.
     BORDER_CONSTANT, 1)

249

    return pad_image


253


  ##############################################################
  #                    ENHANCING ALGORITHM BODY
257 ##############################################################
```

```
print("\n\n\n@@@@@@@@@@ CCD FLUORESCENCE IMAGE ENHANCER @@@@@@@@\nThis
    will allow you to manipulate CCD images. Good work!")

radice=os.getcwd()
print("\n\nYou are working in ", radice)


################  PARSING FILES ################################
# ============================================================
# Set the working path

working_environment= raw_input("Enter y or n depending whether the input
    files are in this folder or not: ")
if working_environment=="y":
    loadfiledir = str('./')
else:
    loadfiledir=raw_input("Enter the path as a string delimited by slahes
    : /.../ ")


absolute_loadfiledir =os.getcwd()   #to get the absolute current working
    path

output_collector=[]
relative_output_collector=[]
absolute_output_collector=[]
new_names=[]



#============================================================
#Choice between relative and absolute path names
```

```
path_name= raw_input("Do you prefer to work with relative of absolute
    paths? (Type r or a respectively) ")

if path_name == "a":
    for (path, dirs, files) in os.walk(absolute_loadfiledir):
        #print("Path=: \n", path, "\n\n")
        #print("Folders: ", dirs , "\n\n")
        #print([f for f in files if f.endswith("tiff")])     # if a.
    endswith('png') or a.endswith('jpg')
        output_collector.extend([f for f in files if f.endswith("tiff")]) #
    only the experimental images
        absolute_output_collector.extend([os.path.join(path,f) for f in
    files if f.endswith("tiff") ]) #complete path of the name of the file

    print("***** ",len(absolute_output_collector),"CCD files successfully
     localized! ***** ")

    print("\n\n")
    print("\n\n")
    print("\n\n")


    listfiles=absolute_output_collector


else:

    # if you want the relative paths for the files
    for (path, dirs, files) in os.walk(loadfiledir):
        print("Path=: \n", path, "\n\n")
        print("Folders: ", dirs , "\n\n")
```

```
        print([f for f in files if f.endswith("tiff")])
        output_collector.extend([f for f in files if f.endswith("tiff")]) #
    only the name of the files
        relative_output_collector.extend([os.path.join(path,f) for f in
    files if f.endswith("tiff") ]) #relative path of the name of the file
317

    print("***** ",len(relative_output_collector),"CCD files successfully
     localized! ***** ")

    print("\n\n")
321 print("\n\n")
    print("\n\n")


325 listfiles=relative_output_collector



329 ################################## PROCESS FILES ######################
  for filename in listfiles:
    if "secs" in filename:
      new_name= filename[:-10]
333 else:
      new_name= filename[:-5] #for the first image of a fluorescence series
    new_names.extend(new_name)

337 # load image
    img_new=cv2.imread(filename)


341 ###############################################
    # resize
```

```
    img_new= resizer(img_new, 853./640, y=False) # to compensate CCD
      horizontal distorsion

345

    ##############################################
    # rotate
    img_new= rotate(img_new, 3.)
349

    ##############################################
    # grayscale
353 img_new= monochrome(img_new)

    ##############################################
357 # ROIs - region of interest
    (ystart,yend, xstart,xend) = ROIs(img_new, 0.000000001, 0.000001)

361 ##############################################
    # crop
    enhanced=cropper(img_new, ystart,yend, xstart,xend)
    #img_new=cropper(enhanced, int(enhanced.shape[0]/2.),enhanced.shape
      [0],0,enhanced.shape[1]) #lower half
365 img_new=cropper(enhanced, int(enhanced.shape[0]/2.),enhanced.shape
      [0],0,enhanced.shape[1]) #lower half

    ##############################################
369 # stitching
    img_new=stitching(img_new, step=1)
```

```
373 ##############################################
    #    # refining

    #    img_new=rotate(img_new, -1)
377

    #    (ystart,yend, xstart,xend) = ROIs(img_new, 5/100, 10.5/100)
    #    enhanced=cropper(img_new, ystart,yend, xstart,xend)

381 #    ##horizontal stitching
    #    west= cropper(enhanced,0,enhanced.shape[0], 0, int(enhanced.shape
        [1]/2.))
    #    east=cv2.flip(west, 1)
    #    img_new= np.hstack((west,east[:,1:]))
385

    ################################################
      # padding
389   img_new=padder(img_new, 480, 640)




393

    ################################################
      # WRITE UPDATE IMAGE
      saver(img_new, new_name+"_modB","png", "./")
397   print("\n==========> Successfully enhanced: \t image:", new_name
        )



401
```

```
cv2.waitKey(100) #display image indef until any key is pressed
cv2.destroyAllWindows() # close every picture window by pressing any key


##############################################################
################  TO BE IMPLEMENTED  #########################
##############################################################
#BLURRING
# #specify the width and height of kernel which should be positive and
    ODD number e.g. 11, 11
# #Gaussian blurring is highly effective in removing gaussian noise from
    the image.
# #blurred = cv2.GaussianBlur(gray, (11, 11), 0)
# blurred = cv2.GaussianBlur(gray, (1, 1), 0)
# cv2.imshow("blurred pic", blurred)


# #image_small= cv2.resize(image, (1200, 800))
# #cv2.imshow("naive", image_small)
# #blurred_small= cv2.resize(blurred, (1200, 800))
# #cv2.imshow("blurred", blurred_small)



##############################################################
# # THRESHIOLD algorithm
# #To reveal the brightest regions in the blurred image we need to apply
    thresholding:
# # takes any pixel value p >= 200 and sets it to 255 (white). Pixel
    values < 200 are set to 0 (black).
```

```
## for 8-bit gray scale encoding there are 256 values - from 0 to 255 -
    where 0 is pure black and 255 is pure white

# thresh = cv2.threshold(blurred, 100, 255, cv2.THRESH_BINARY)[1]

# cv2.imshow("threshold filter", thresh)



## erosion and dilation routines to clean noise in this image (i.e.,
   small blobs):
## perform a series of erosions and dilations to remove - erosion will
   reduce the area of each bright spot removing peripheral parts
## any small blobs of noise from the thresholded image
# thresh = cv2.erode(thresh, None, iterations=1)
# cv2.imshow("threshold cleaned erosion", thresh)

## #thresh = cv2.dilate(thresh, None, iterations=4)
## #cv2.imshow("threshold cleaned erosion & dilation", thresh)



#################################################################
## Masking
#################################################################
## Segmentation - finding Edges
#################################################################
## Machine learning and convolutional neural network template matching
```

References

[1] P. W. P. W. Atkins, J. De Paula, and J. Keeler, *Atkins' Physical chemistry*, Oxford University Press, Oxford, 10 edition, 2014.

[2] M. T. Bell and T. P. Softley, *Molecular Physics*, **107**, 99, 2009.

[3] R. Sahai and L.-Å. Nyman, *The Astrophysical Journal*, **487**, L155, 1997.

[4] D. W. Chandler, *The Journal of Chemical Physics*, **132**, 13918, 2010.

[5] M. Gupta and D. Herschbach, *Journal of Physical Chemistry A*, **103**, 10670, 1999.

[6] M. Gupta and D. Herschbach, *Journal of Physical Chemistry A*, **105**, 2001.

[7] L. D. Harper, *D. Phil. Thesis, University of Oxford*, 2013.

[8] K. S. Twyman, *D. Phil Thesis, University of Oxford*, 2013.

[9] B. R. Rowe, G. Dupeyrat, J. B. Marquette, and P. Gaucherel, *Citation: The Journal of Chemical Physics*, **80**, 164305, 1984.

[10] I. W. M. Smith, *Low Temperatures and Cold Molecules. Imperial College Press, London*, 2008.

[11] I. R. Sims, J.-L. Queffelec, A. Defrance, C. Rebrion-Rowe, D. Travers, P. Bocherel, B. R. Rowe, and I. W. M. Smith, *Citation: The Journal of Chemical Physics*, **100**, 214203, 1994.

[12] H. L. Bethlem, F. M. H. Crompvoets, R. T. Jongma, S. Y. T. Van De Meerakker, and G. Meijer, *Physical Review A*, **65**, 2002.

[13] K. Wohlfart, F. Filsinger, F. Grätz, J. Küpper, and G. Meijer, *Physical Review A*, **78**, 2008.

[14] X. Wang, M. Kirste, G. Meijer, and S. Y. T. Van De Meerakker, *Z. Phys. Chem*, **227**, 1595, 2013.

[15] M. Schnell, G. Meijer, M. Schnell, and G. Meijer, *Angewandte Chemie International Edition*, **48**, 6010, 2009.

[16] E. Vliegen, S. D. Hogan, H. Schmutz, and F. Merkt, *Physical Review A*, **76**, 023405, 2007.

[17] S. D. Hogan, P. Allmendinger, H. Saßmannshausen, H. Schmutz, and F. Merkt, *Physical Review Letters*, **108**, 063008, 2012.

[18] N. Vanhaecke, U. Meier, M. Andrist, B. H. Meier, and F. Merkt, *Physical Review A*, **75**, 031402, 2007.

[19] E. Narevicius, A. Libson, C. G. Parthey, I. Chavez, J. Narevicius, U. Even, and M. G. Raizen, *Physical Review Letters*, **100**, 093003, 2008.

[20] K. Dulitz, J. Toscano, A. Tauschinsky, and T. P. Softley, *Journal of Physics B: Atomic, Molecular and Optical Physics*, **49**, 075203, 2016.

[21] T. Momose, Y. Liu, S. Zhou, P. Djuricanin, and D. Carty, *Physical Chemistry Chemical Physics*, **15**, 1772, 2013.

[22] A. Wiederkehr, H. Schmutz, M. Motsch, and F. Merkt, *Molecular Physics*, **110**, 1807, 2012.

[23] J. Toscano, A. Tauschinsky, K. Dulitz, C. J. Rennick, B. R. Heazlewood, and T. P. Softley, *New Journal of Physics*, **19**, 083016, 2017.

[24] K. Dulitz, *D. Phil. Thesis, University of Oxford*, 2014.

[25] P. F. Barker and M. N. Shneider, *Physical Review A*, **66**, 065402, 2002.

[26] P. B. Corkum, C. Ellert, M. Mehendale, P. Dietrich, S. Hankin, S. Aseyev, D. Rayner, and D. Villeneuve, *Faraday Discussions*, **113**, 47, 1999.

[27] T. Junglen, T. Rieger, S. A. Rangwala, P. W. H. Pinkse, and G. Rempe, *The European Physical Journal D*, **31**, 365, 2004.

[28] S. Willitsch, M. Bell, A. Gingell, S. Procter, and T. Softley, *Physical Review Letters*, **100**, 043203, 2008.

[29] M. Motsch, L. D. van Buuren, C. Sommer, M. Zeppenfeld, G. Rempe, and P. W. H. Pinkse, *Physical Review A*, **79**, 013405, 2009.

[30] L. D. van Buuren, C. Sommer, M. Motsch, S. Pohle, M. Schenk, J. Bayerl, P. W. H. Pinkse, and G. Rempe, *Physical Review Letters*, **102**, 033001, 2009.

[31] S. Chervenkov, X. Wu, J. Bayerl, A. Rohlfes, T. Gantner, M. Zeppenfeld, and G. Rempe, *Physical Review Letters*, **112**, 013001, 2014.

[32] A. B. Henson, S. Gersten, Y. Shagam, J. Narevicius, and E. Narevicius, *Science*, **338**, 234, 2012.

[33] J. Jankunas, B. Bertsche, K. Jachymski, M. Hapka, and A. Osterwalder, *The Journal of Chemical Physics*, **140**, 244302, 2014.

[34] A. Osterwalder, *EPJ Techniques and Instrumentation*, **2**, 10, 2015.

[35] K. Dulitz and T. P. Softley, *The European Physical Journal D*, **70**, 19, 2016.

[36] J. Toscano, C. J. Rennick, T. P. Softley, and B. R. Heazlewood, *Journal of Chemical Physics (under review)*, 2018.

[37] D. Gerlich, Ion-Neutral Collisions in a 22-Pole Trap at Very Low Energies, Technical report, 1995.

[38] F. Stienkemeier and K. K. Lehmann, *Journal of Physics B: Atomic, Molecular and Optical Physics*, **39**, 127, 2006.

[39] J. Küpper and J. M. Merritt, *International Reviews in Physical Chemistry*, **26**, 249, 2007.

[40] J. Higgins, C. Callegari, J. Reho, F. Stienkemeier, W. E. Ernst, M. Gutowski, and G. Scoles, *J. Phys. Chem. A*, **102**, 4952, 1998.

[41] D. Leibfried, R. Blatt, C. Monroe, and D. Wineland, *Reviews of Modern Physics*, **75**, 2003.

[42] E. S. Shuman, J. F. Barry, and D. DeMille, *Nature*, **467**, 820, 2010.

[43] J. D. Miller, R. A. Cline, and D. J. Heinzen, *Physical Review A*, **47**, R4567, 1993.

[44] E. L. Raab, M. Prentiss, A. Cable, S. Chu, and D. E. Pritchard, *Physical Review Letters*, **59**, 2631, 1987.

[45] M. H. Anderson, J. R. Ensher, M. R. Matthews, C. E. Wieman, and E. A. Cornell, *Science*, **269**, 198, 1995.

[46] K. E. Strecker and D. W. Chandler, *Physical Review A*, **78**, 063406, 2008.

[47] J. J. Kay, S. Y. T. van de Meerakker, K. E. Strecker, and D. W. Chandler, *Faraday Discussions*, **142**, 143, 2009.

[48] J. J. Kay, J. Kłos, M. H. Alexander, K. E. Strecker, and D. W. Chandler, *Physical Review A*, **82**, 032709, 2010.

[49] J. Jankunas and A. Osterwalder, *Annual Review of Physical Chemistry*, **66**, 241, 2015.

[50] Chefdeville, Kalugina, van de Meerakker, Naulin, Lique, and Costes, *Science*, **341**, 1094, 2013.

[51] A. B. Henson, S. Gersten, Y. Shagam, J. Narevicius, and E. Narevicius, *Science (New York, N.Y.)*, **338**, 234, 2012.

[52] A. Trottier, D. Carty, and E. Wrede, *Molecular Physics*, **109**, 725, 2011.

[53] W. G. Doherty, M. T. Bell, T. P. Softley, A. Rowland, E. Wrede, and D. Carty, *Physical chemistry chemical physics*, **13**, 8441, 2011.

[54] F. Masnou-Seeuws and P. Pillet, *Advances In Atomic, Molecular, and Optical Physics*, **47**, 53, 2001.

[55] K.-K. Ni, S. Ospelkaus, M. H. G. de Miranda, A. Pe'er, B. Neyenhuis, J. J. Zirbel, S. Kotochigova, P. S. Julienne, D. S. Jin, and J. Ye, *Science (New York, N.Y.)*, **322**, 231, 2008.

[56] N. Deb, L. L. Pollum, A. D. Smith, M. Keller, C. J. Rennick, B. R. Heazlewood, and T. P. Softley, *Physical Review A - Atomic, Molecular, and Optical Physics*, **91**, 1, 2015.

[57] M. Schwarz, O. O. Versolato, A. Windberger, F. R. Brunner, T. Ballance, S. N. Eberle, J. Ullrich, P. O. Schmidt, A. K. Hansen, A. D. Gingell, M. Drewsen, and J. R. C. López-Urrutia, *Review of Scientific Instruments*, **83**, 083115, 2012.

[58] J. Chiaverini, B. R. Blakestad, J. W. Britton, J. D. Jost, C. Langer, D. G. Leibfried, R. Ozeri, and D. J. Wineland, *Quantum Information and Computation*, **5**, 2005.

[59] A. Mokhberi and S. Willitsch, *Physical Review A*, **90**, 023402, 2014.

[60] F. H. J. Hall, M. Aymar, N. Bouloufa-Maafa, O. Dulieu, and S. Willitsch, *Physical review letters*, **107**, 243202, 2011.

[61] R. Wester, *Journal of Physics B: Atomic, Molecular and Optical Physics*, **42**, 154001, 2009.

[62] J. Mikosch, U. Frühling, S. Trippel, R. Otto, P. Hlavenka, D. Schwalm, M. Weidemüller, and R. Wester, *Physical Review A*, **78**, 023402, 2008.

[63] E. Endres, G. Egger, S. Lee, O. Lakhmanskaya, M. Simpson, and R. Wester, *Journal of Molecular Spectroscopy*, **332**, 134, 2017.

[64] R. C. Thompson, *Contemporary Physics*, **56**, 63, 2015.

[65] R. Blumel, The dynamic Kingdon trap: A novel design for the storage and crystallization of laser-cooled ions, Technical report, 1995.

[66] Q. Hu, R. J. Noll, H. Li, A. Makarov, M. Hardman, and R. Graham Cooks, *Journal of Mass Spectrometry*, **40**, 430, 2005.

[67] A. Mody, M. Haggerty, J. M. Doyle, and E. J. Heller, *Physical Review B*, **64**, 085418, 2001.

[68] D. Clary, *Molecular Physics*, **54**, 605, 1985.

[69] D. C. Clary, *Journal of the Chemical Society, Faraday Transactions 2*, **83**, 139, 1987.

[70] J. Troe and V. G. Ushakov, *The Journal of Chemical Physics*, **128**, 204307, 2008.

[71] W. L. Hase, *Dynamics of ion-molecule complexes, Elsevier, Amsterdam, The Netherlands.*, Elsevier, Amsterdam, The Netherlands., 2016.

[72] T. Rosenband, D. B. Hume, P. O. Schmidt, C. W. Chou, A. Brusch, L. Lorini, W. H. Oskay, R. E. Drullinger, T. M. Fortier, J. E. Stalnaker, S. A. Diddams, W. C. Swann, N. R. Newbury, W. M. Itano, D. J. Wineland, and J. C. Bergquist, *Science (New York, N.Y.)*, **319**, 1808, 2008.

[73] A. D. Ludlow, M. M. Boyd, J. Ye, E. Peik, and P. Schmidt, *Reviews of Modern Physics*, **87**, 637, 2015.

[74] W. G. Rellergert, D. DeMille, R. R. Greco, M. P. Hehlen, J. R. Torgerson, and E. R. Hudson, *Physical Review Letters*, **104**, 200802, 2010.

[75] S. Gulde, M. Riebe, G. P. T. Lancaster, C. Becher, J. Eschner, H. Häffner, F. Schmidt-Kaler, I. L. Chuang, and R. Blatt, *Nature*, **421**, 48, 2003.

[76] R. Blatt and D. Wineland, *Nature*, **453**, 1008, 2008.

[77] D. P. L. A. Craik, N. M. Linke, M. A. Sepiol, T. P. Harty, J. F. Goodwin, C. J. Ballance, D. N. Stacey, A. M. Steane, D. M. Lucas, and D. T. C. Allcock, *Physical Review A*, **95**, 22337, 2017.

[78] R. C. Sterling, H. Rattanasonti, S. Weidt, K. Lake, P. Srinivasan, S. C. Webster, M. Kraft, and W. K. Hensinger, *Nature Communications*, **5**, 3637, 2014.

[79] R. P. Feynman, *International Journal of Theoretical Physics*, **21**, 467, 1982.

[80] J. I. Cirac and P. Zoller, *Nature Physics 2012 8:4*, 2012.

[81] I. Bloch, J. Dalibard, and S. Nascimbène, *Nature Physics*, **8**, 267, 2012.

[82] M. A. Baranov, M. Dalmonte, G. Pupillo, and P. Zoller, *Chemical Reviews*, **112**, 5012, 2012.

[83] I. Buluta and F. Nori, *Science (New York, N.Y.)*, **326**, 108, 2009.

[84] H. L. Bethlem and W. Ubachs, *Faraday Discussions*, **142**, 25, 2009.

[85] M. P. Langevin, *Annales de Chimie et de Physique, series*, **5**, 245, 1905.

[86] G. Gioumousis and D. P. Stevenson, *The Journal of Chemical Physics*, **29**, 294, 1958.

[87] D. C. Clary, *Annual Review of Physical Chemistry*, **41**, 61, 1990.

[88] A. D. Gingell, *D. Phil. Thesis, University of Oxford*, 2010.

[89] D. C. Clary, *Journal of the Chemical Society, Faraday Transactions 2*, **83**, 139, 1987.

[90] N. G. Adams, D. Smith, and D. C. Clary, *The Astrophysical Journal*, **296**, 31, 1985.

[91] J.-B. Marquette, B.-R. Rowe, G. Dupeyrat, G. Poissant, and . S. Rebrion, *Chem. Phys. Lett.*, **122**, 431, 1985.

[92] D. Smith, P. Spanel, and C. A. Mayhew, *International Journal of Mass Spectrometry and Ion Processes*, **117**, 457, 1992.

[93] D. Smith and P. Španel, *International Journal of Mass Spectrometry*, **377**, 467, 2015.

[94] D. W. Trainor, D. O. Ham, and F. Kaufman, *The Journal of Chemical Physics*, **58**, 4599, 1973.

[95] W. W. Duley and Williams D. A., *Interstellar chemistry*, London : Academic Press, 1984.

[96] J. Woodall, M. Agúndez, A. J. Markwick-Kemper, and T. J. Millar, *Astronomy & Astrophysics*, **466**, 1197, 2007.

[97] KIDA : KInetic Database for Astrochemistry.

[98] V. Wakelam, E. Herbst, and F. Selsis, *Astronomy & Astrophysics*, **451**, 551, 2006.

[99] V. Wakelam, I. W. M. Smith, E. Herbst, J. Troe, W. Geppert, H. Linnartz, K. Öberg, E. Roueff, M. Agúndez, P. Pernot, H. M. Cuppen, J. C. Loison, and D. Talbi, *Space Science Reviews*, **156**, 13, 2010.

[100] W. Paul, *Reviews of Modern Physics*, **62**, 531, 1990.

[101] W. Paul, *Angewandte Chemie International Edition in English*, **29**, 739, 1990.

[102] M. Drewsen, I. Jensen, J. Lindballe, N. Nissen, R. Martinussen, A. Mortensen, P. Staanum, and D. Voigt, *International Journal of Mass Spectrometry*, **229**, 83, 2003.

[103] A. Mokhberi and S. Willitsch, *Physical Review A*, **90**, 023402, 2014.

[104] A. Gardner, K. Sheridan, W. Groom, N. Seymour-Smith, and M. Keller, *Applied Physics B*, **117**, 755, 2014.

[105] L. Deslauriers, S. Olmschenk, D. Stick, W. K. Hensinger, J. Sterk, and C. Monroe, *Physical Review Letters*, **97**, 103007, 2006.

[106] H. Noshad and M. Honari-Latifpour, *International Journal of Mass Spectrometry*, **374**, 49, 2014.

[107] M. Steiner, H. M. Meyer, C. Deutsch, J. Reichel, and M. Köhl, *Physical Review Letters*, **110**, 043003, 2013.

[108] B. R. Heazlewood and T. P. Softley, *Annual Review of Physical Chemistry*, **66**, 475, 2015.

[109] J. D. Prestage, G. J. Dick, and L. Maleki, *Journal of Applied Physics*, **66**, 1013, 1989.

[110] M. Drewsen and A. Brøner, *Physical Review A*, **62**, 045401, 2000.

[111] H. Dehmelt, *Advances in Atomic and Molecular Physics*, **3**, 53, 1968.

[112] D. Gerlich, *Inhomogeneous rf fields: a versatile tool for the study of processes with slow ions*, John Wiley & Sons, Inc, 1992.

[113] D. J. Berkeland, J. D. Miller, J. C. Bergquist, W. M. Itano, and D. J. Wineland, *Journal of Applied Physics*, **83**, 5025, 1998.

[114] C. S. Adams and E. Riis, *Laser Cooling and Manipulation of Neutral Particles*, Cambridge University Press, the new op edition.

[115] D. Leibfried, R. Blatt, C. Monroe, and D. Wineland, *Reviews of Modern Physics*, **75**, 281, 2003.

[116] W. D. Phillips, *Reviews of Modern Physics*, **70**, 721, 1998.

[117] S. Chu, *Reviews of Modern Physics*, **70**, 685, 1998.

[118] J. Dalibard and C. Cohen-Tannoudji, *Journal of the Optical Society of America B*, **6**, 2023, 1989.

[119] H. J. Metcalf and P. Van der Straten, *Laser cooling and trapping*, Springer, 1999.

[120] J. H. V. Nguyen, C. R. Viteri, E. G. Hohenstein, C. D. Sherrill, K. R. Brown, and B. Odom, *New Journal of Physics*, **13**, 063023, 2011.

[121] G. Ritter, S.-M. Bae, and U. Eichmann, *Applied Physics B*, **66**, 609, 1998.

[122] P. Horak, A. Dantan, and M. Drewsen, *Physical Review A*, **86**, 43435, 2012.

[123] D. J. Larson, J. C. Bergquist, J. J. Bollinger, W. M. Itano, and D. J. Wineland, *Physical Review Letters*, **57**, 70, 1986.

[124] TakashiBaba and I. Waki, *Japanese Journal of Applied Physics*, **35**, L1134, 1996.

[125] P. Bowe, L. Hornekær, C. Brodersen, M. Drewsen, J. S. Hangst, and J. P. Schiffer, *Physical Review Letters*, **82**, 2071, 1999.

[126] K. Mølhave and M. Drewsen, *Physical Review A*, **62**, 011401, 2000.

[127] N. Deb, B. R. Heazlewood, M. T. Bell, and T. P. Softley, *Physical Chemistry Chemical Physics*, **15**, 14270, 2013.

[128] C. B. Zhang, D. Offenberg, B. Roth, M. A. Wilson, and S. Schiller, *Physical Review A*, **76**, 012719, 2007.

[129] J. Elworthy, *Part II (M. Chem.) Thesis, Universtiy of Oxford*, 2018.

[130] L. Verlet, *Physical Review*, **159**, 98, 1967.

[131] GIMP, GNU igmage Manipulation Program 2015, 2015.

[132] C. T. Rueden, J. Schindelin, M. C. Hiner, B. E. DeZonia, A. E. Walter, E. T. Arena, and K. W. Eliceiri, *BMC Bioinformatics*, **18**, 529, 2017.

[133] L. L. Pollum, *D. Phil. Thesis, University of Oxford*, 2015.

[134] F. Cascarini, *Part II (M. Chem.) Thesis, Universtiy of Oxford*, 2016.

[135] National Instruments, LabVIEW, NI, 2011.

[136] N. Deb, *D. Phil. Thesis, University of Oxford*, 2014.

[137] E. W. Steer, *D. Phil. Thesis, University of Oxford*, 2017.

[138] H. L. Bethlem, G. Berden, and G. Meijer, *Physical Review Letters*, **83**, 1558, 1999.

[139] M. T. Bell, *D. Phil. Thesis, University of Oxford*, 2008.

[140] H. L. Bethlem and G. Meijer, *International Reviews in Physical Chemistry*, **22**, 73, 2003.

[141] M. Kirste, B. G. Sartakov, M. Schnell, and G. Meijer, *Physical Review A*, **79**, 051401, 2009.

[142] MATLAB, R2013a, The MathWorks, Inc., Natick, Massachusetts, United States, 2013.

[143] C. E. Heiner, H. L. Bethlem, and G. Meijer, *Physical Chemistry Chemical Physics*, **8**, 2666, 2006.

[144] J. M. Oldham, *D. Phil. Thesis, University of Oxford*, 2014.

[145] C. M. Western, *Journal of Quantitative Spectroscopy and Radiative Transfer*, 2017.

[146] C. Sommer, L. D. van Buuren, M. Motsch, S. Pohle, J. Bayerl, P. W. H. Pinkse, and G. Rempe, *Faraday Discussions*, **142**, 203, 2009.

[147] C. Sommer, M. Motsch, S. Chervenkov, L. D. van Buuren, M. Zeppenfeld, P. W. H. Pinkse, and G. Rempe, *Physical Review A*, **82**, 013410, 2010.

[148] M. Motsch, C. Sommer, M. Zeppenfeld, L. D. van Buuren, P. W. H. Pinkse, and G. Rempe, *New Journal of Physics*, **11**, 055030, 2009.

[149] K. S. Twyman, M. T. Bell, B. R. Heazlewood, and T. P. Softley, *The Journal of chemical physics*, **141**, 024308, 2014.

[150] D. C. Lis, E. Roueff, M. Gerin, T. G. Phillips, L. H. Coudert, F. F. S. van der Tak, and P. Schilke, *The Astrophysical Journal*, **571**, L55, 2002.

[151] K. A. Meyer, L. L. Pollum, L. S. Petralia, A. Tauschinsky, C. J. Rennick, T. P. Softley, and B. R. Heazlewood, *Journal of Physical Chemistry A*, **119**, 12449, 2015.

[152] O. O. Versolato, M. Schwarz, A. K. Hansen, A. D. Gingell, A. Windberger, Ł. Kłosowski, J. Ullrich, F. Jensen, J. R. Crespo López-Urrutia, and M. Drewsen, *Physical Review Letters*, **111**, 053002, 2013.

[153] M. Drewsen, A. Mortensen, R. Martinussen, P. Staanum, and J. L. Sørensen, *Physical Review Letters*, **93**, 1, 2004.

[154] M. Welling, H. a. Schuessler, R. I. Thompson, and H. Walther, *International Journal of Mass Spectrometry and Ion Processes*, **172**, 95, 1998.

[155] K. Højbjerre, D. Offenberg, C. Z. Bisgaard, H. Stapelfeldt, P. F. Staanum, A. Mortensen, and M. Drewsen, *Physical Review A*, **77**, 030702, 2008.

[156] S. Willitsch, M. T. Bell, A. D. Gingell, and T. P. Softley, *Physical Chemistry Chemical Physics*, **10**, 7200, 2008.

[157] K. Sheridan and M. Keller, *New Journal of Physics*, **13**, 123002, 2011.

[158] W. C. Wiley and I. H. McLaren, *Review of Scientific Instruments*, **26**, 1150, 1955.

[159] M. M. Wolff and W. E. Stephens, *Review of Scientific Instruments*, **24**, 616, 1953.

[160] C. Schneider, S. J. Schowalter, K. Chen, S. T. Sullivan, and E. R. Hudson, *Physical Review Applied*, **2**, 034013, 2014.

[161] G. van Rossum, *Python tutorial, Technical Report CS-R9526, Centrum voor Wiskunde en Informatica (CWI), Amsterdam*, 1995.

[162] W. C. Swope, H. C. Andersen, P. H. Berens, and K. R. Wilson, *The Journal of Chemical Physics*, **76**, 637, 1982.

[163] D. A. Dahl, *International Journal of Mass Spectrometry*, **200**, 2000.

[164] M. Quintero-Pérez, P. Jansen, and H. L. Bethlem, *Physical Chemistry Chemical Physics*, **14**, 9630, 2012.

[165] D. Rösch, H. Gao, A. Kilaj, and S. Willitsch, *EPJ Techniques and Instrumentation*, **3**, 5, 2016.

[166] P. C. Schmid, J. Greenberg, M. I. Miller, K. Loeffler, and H. J. Lewandowski, *Review of Scientific Instruments*, **88**, 123107, 2017.

[167] B. A. Mamyrin, V. I. Karataev, D. V. Shmikk, and V. A. Zagulin, *Soviet Journal of Experimental and Theoretical Physics*, **37**, 1973.

[168] E. W. Steer, L. S. Petralia, C. M. Western, B. R. Heazlewood, and T. P. Softley, *Journal of Molecular Spectroscopy*, **332**, 94, 2017.

[169] D. Skouteris, D. E. Manolopoulos, W. Bian, H.-J. Werner, L.-H. Lai, and K. Liu, *Science (New York, N.Y.)*, **266**, 998, 1994.

[170] N. Balakrishnan, *The Journal of Chemical Physics*, **121**, 5563, 2004.

[171] A. J. Orr-Ewing and R. N. Zare, *Annual Review of Physical Chemistry*, **45**, 315, 1994.

[172] J. Booth, S. Bragg, and G. Hancock, *Chemical Physics Letters*, **113**, 509, 1985.

[173] P. R. Brooks, *Science*, **193**, 11, 1976.

[174] M. H. G. de Miranda, A. Chotia, B. Neyenhuis, D. Wang, G. Quéméner, S. Ospelkaus, J. L. Bohn, J. Ye, and D. S. Jin, *Nature Physics*, **7**, 502, 2011.

[175] J. Jankunas, K. S. Reisyan, T. P. Rakitzis, and A. Osterwalder, *Molecular Physics*, **114**, 245, 2016.

[176] K. Schreel and J. J. Ter Meulen, *J. Phys. Chem. A*, **101**, 1997.

[177] P. R. Brooks, E. M. Jones, and K. Smith, *The Journal of Chemical Physics*, **51**, 3073, 1969.

[178] P. W. Harland, W.-P. Hu, C. Vallance, and P. R. Brooks, *Physical Review A*, **60**, 1999.

[179] E. W. Steer, K. S. Twyman, B. R. Heazlewood, and T. P. Softley, *Molecular Physics*, **113**, 1465, 2015.

[180] D. Papousek, M. Bester, K. Yamada, G. Winnewisser, and A. Guarnieri, *Journal of Molecular Spectroscopy*, **106**, 29, 1984.

[181] J. Bentley, B. J. Cotterell, A. Langham, and R. J. Stickland, *Chemical Physics Letters*, **332**, 2000.

[182] T. E. Wall, S. K. Tokunaga, E. A. Hinds, and M. R. Tarbutt, *Physical Review A*, **81**, 33414, 2010.

[183] D. J. Levandier and Y.-H. Chiu, *The Journal of chemical physics*, **133**, 154304, 2010.

[184] N. G. Adams, D. Smith, and E. Alge, *Journal of Physics B: Atomic and Molecular Physics*, **13**, 3235, 1980.

[185] T. Su and M. T. Bowers, *International Journal of Mass Spectrometry and Ion Physics*, **12**, 347, 1973.

[186] J. Loreau, ULB, Bruxelles, Private communication, 2017.

[187] S. Willitsch, 307–340, 2017.

[188] D. Zhang and S. Willitsch, *Cold Ion Chemistry*, 2017.

[189] E. Halevi, E. Haran, and B. Ravid, *Chemical Physics Letters*, **1**, 475, 1967.

[190] C. Scher, B. Ravld, and E. A. Halevi, *J. Phys. Chem*, **86**, 654, 1982.

[191] S. J. Bajic, R. N. Compton, X. Tang, and P. Lambropoulos, *Physical Review A*, **44**, 1991.

[192] S. Jullien, J. Lemaire, S. Fenistein, M. Heninger, G. Mauclaire, and R. Marx, *Chemical Physics Letters*, **212**, 340, 1993.

[193] L. Hornekær, N. Kjærgaard, A. M. Thommesen, and M. Drewsen, *Physical Review Letters*, **86**, 1994, 2001.

[194] U. Fröhlich, B. Roth, and S. Schiller, *Physics of Plasmas*, **12**, 073506, 2005.

[195] ANACONDA, vers. 2-2.4.0, Anaconda Software Distribution. Computer software, 2016.

[196] OpenCV and Itseez, Open Source Computer Vision Library, 2015.